Nanoscale

REVIEW

Cite this: *Nanoscale*, 2024, **16**, 3838

Defects in lead halide perovskite light-emitting diodes under electric field: from behavior to passivation strategies

Na Jiang,[a,b] Guoquan Ma,[a,b] Dandan Song,[a,b] Bo Qiao,[a,b] Zhiqin Liang,[a,b] Zheng Xu,*[a,b] Swelm Wageh,[c] Ahmed Al-Ghamdi[c] and Suling Zhao*[a,b]

Lead halide perovskites (LHPs) are emerging semiconductor materials for light-emitting diodes (LEDs) owing to their unique structure and superior optoelectronic properties. However, defects that initiate degradation of LHPs through external stimuli and prompt internal ion migration at the interfaces remain a significant challenge. The electric field (EF), which is a fundamental driving force in LED operation, complicates the role of these defects in the physical and chemical properties of LHPs. A deeper understanding of EF-induced defect behavior is crucial for optimizing the LED performance. In this review, the origins and characterization of defects are explored, indicating the influence of EF-induced defect dynamics on LED performance and stability. A comprehensive overview of recent defect passivation approaches for LHP bulk films and nanocrystals (NCs) is also provided. Given the ubiquity of EF, a summary of the EF-induced defect behavior can enhance the performance of perovskite LEDs and related optoelectronic devices.

Received 22nd December 2023,
Accepted 29th January 2024

DOI: 10.1039/d3nr06547b

rsc.li/nanoscale

1. Introduction

Over the past decade, lead halide perovskites (LHPs) have garnered substantial attention owing to their remarkable optoelectronic properties, including exceptional color purity,[1] tunable optical bandgaps,[2] robust defect tolerance,[3,4] narrow emission linewidths,[1] wide color gamut,[2] high charge-carrier mobility,[5] and elevated photoluminescence quantum yield (PLQY).[6] Consequently, LHPs have found widespread applications in various optoelectronic devices, such as photovoltaics, light-emitting diodes (LEDs), nanolaser, and photodetectors.[3,7,8] In 2014, Tan *et al.* first realized near-infrared, red, and green electroluminescence (EL) devices based on perovskite at room temperature.[9] Subsequently, there has been a significant increase in the external quantum efficiency (EQE)

---

[a] *Key Laboratory of Luminescence and Optical Information, Beijing Jiaotong University, Ministry of Education, Beijing, 100044, China. E-mail: zhengxu@bjtu.edu.cn, slzhao@bjtu.edu.cn*
[b] *Institute of Optoelectronics Technology, Beijing Jiaotong University, Beijing, 100044, China*
[c] *Department of Physics, Faculty of Science, King Abdulaziz University, Jeddah 21589, Saudi Arabia*

Na Jiang

Na Jiang received her B.S. from Hebei University in 2020. Now, she is a Ph.D. candidate in Optical Engineering at Beijing Jiaotong University, under the supervision of Professor Zheng Xu. Her current research focuses on optoelectronic devices based on metal halide perovskites.

Zheng Xu

Zheng Xu works in the Beijing Jiaotong University as a physics professor since 2005. He got his Ph.D. in 2002 at the Graduate School of the Chinese Academy of Sciences with a major in condensed matter physics. In 1996, he joined the Institute of Optoelectronic Technology, Beijing Jiaotong University as a senior engineer. His research interests are optoelectronic materials and devices, flat panel display technology, solar cells, semiconductor lighting, and nanomaterials.

of perovskite light-emitting diodes (PeLEDs), with red, green, and blue PeLEDs reaching 26.3%,[10] 30.84%,[11] 18.65%,[12] respectively, within a relatively short time frame. Numerous studies have focused on the investigation of defects in perovskite materials, which have emerged as a recurring focal point for enhancing device performance and stability.

Similar to traditional colloidal quantum dot light-emitting diodes (QLEDs) and organic light-emitting diodes (OLEDs), the solution-based processability inherent in PeLEDs inevitably generates defects, which, in the context of PeLEDs, are pivotal factors influencing their commercial feasibility. Nanocrystals (NCs) and thin films from the perovskite family frequently feature intrinsic, grain boundary, and interface defects.[13] Shallow-level defects, typically originating from inherent point defects, serve as carrier traps to capture electrons and holes, thereby creating avenues for energy loss.[14] Even though LHPs are acknowledged for their high "defect tolerance", diverse defects can induce alterations in the energy band of the emitting layer (EML), resulting in energy band misalignment.[15] Moreover, deep-level defects commonly form centers for nonradiative recombination, disrupting charge transport and impacting carrier lifetime and PLQY.[16] Defects are the fundamental origin of ion migration. The phenomenon of ion migration, driven by point defects and grain boundary defects, leads to phase separation, shifts in EL peak position, and device instability.[17] In light of these considerations, we posit that a more profound understanding and controlled manipulation of defect behaviors hold the potential to significantly enhance the performance of PeLEDs, particularly in terms of EQE and stability.

In addition to defect physics, defect behavior under an inevitable electric field (EF) has exhibited another impact that requires serious consideration. Generally, defects can transform into "charged defects" under sustained EF, resulting in free carrier-like motion, particularly in halide vacancies associated with ion migration. Ion migration poses a real obstacle to the stability and ageing of perovskites. First-principles calculations with increasing EF have verified alterations in lattice structures, including lattice parameters, band gaps, and light absorption properties.[19] The influence of EF on the interaction between charged defects and photoexcited species leads to temperature-dependent changes in the PL yield and decay.[20] Furthermore, the migration of charged defects can undergo redox reactions, producing new defects under bias, subsequently leading to new nonradiative centers detrimental to the PeLEDs.[21] Nevertheless, the intricacies of defect behavior under active EF remain generally undefined, indicating an urgent need for comprehensive exploration.

Suling Zhao

Suling Zhao works in the Beijing Jiaotong University as a physics professor since 2011. She got her Ph.D. in 2003 at Northern Jiaotong University with a major of luminescence, then she finished her postdoc works in Tohoku University of Japan and Paris Sud University of France. In 2005, she joined the Institute of Optoelectronic Technology, Beijing Jiaotong University as an associate professor. Her research interests are luminescence nanomaterials and devices, electroluminescence devices, and solar cells.

In this review, we presented a comprehensive discussion of the origin, characterization, and behavior of defects under EF and their passivation in PeLEDs, as depicted in Fig. 1. We began by elucidating the significance of defects, delving into their nature, classification, and characterization within perovskites. Subsequently, we presented several current perspectives on the defect behavior under EF. Based on the damage posed by field-induced defect behavior, we outlined the latest strategies for defect passivation and regulation to enhance the stability and efficiency of PeLEDs. We concluded by discussing current theories on defect behavior and highlighting avenues for future research.

2. Significance of defects

The defect state density in lead-based perovskites has been reported to range from 10^{10} to 10^{18} cm^{-3}.[22] The presence of these defects compromise device performance, impeding the commercial potential of perovskite devices.

2.1 Fundamental characteristics of LHPs

Crystalline LHPs conform to the ABX_3 chemical stoichiometry: 'A' signifies a monovalent cation such as $CH_3NH_3^+$ (MA^+), $CH(NH_2)_2^+$ (FA^+), or Cs^+; 'B' denotes a divalent metal cation, typically Pb^{2+} or Sn^{2+}; and 'X' represents a halide anion, usually Cl^-, Br^-, or I^-. The octahedral $[BX_6]^{4-}$ consists of six halide anions coordinating with the B-site cation, and the extended framework of the corner-sharing $[BX_6]^{4-}$ octahedrons encloses a cuboctahedral void filled by the larger A cation, as shown in Fig. 2a.[23] Three standard crystal structures, α (cubic), β (tetragonal), and γ (orthorhombic), are associated with the extent of the $[BX_6]^{4-}$ octahedron tilt, as illustrated in Fig. 2b. The A-site cation forms ionic bonds with $[BX_6]^{4-}$ octahedra, bestowing LHPs with distinctive electron-ionic properties and a softer lattice than other traditional semiconductors. The Goldschmidt tolerance factor (t) and octahedral factor (μ) were used to assess the stability of the LHP lattice.

$$t = \frac{R_A + R_B}{\sqrt{2}(R_B + R_X)} \tag{1}$$

$$\mu = \frac{R_B}{R_X} \tag{2}$$

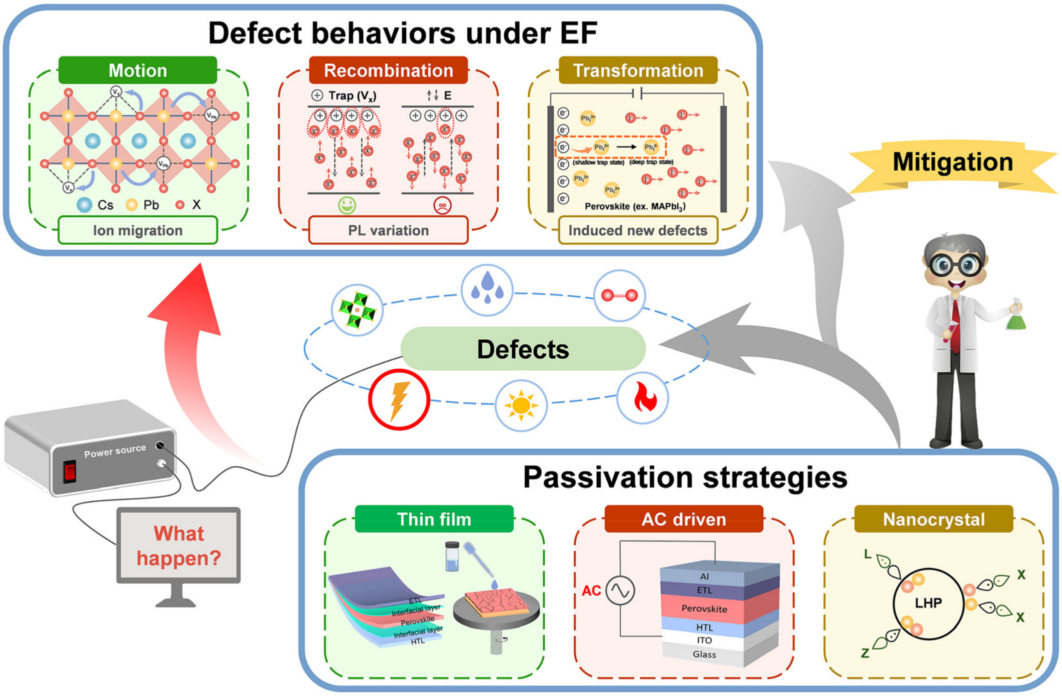

Fig. 1 Schematic summary of EF-induced defect behaviors and passivation strategies in PeLEDs.

where R_A, R_B, and R_X denote the ionic radii of the A-, B-, and C-sites, respectively. The cubic phase is typically indicated by range of $0.9 \le t \le 1$, whereas the orthorhombic phase aligns with $0.71 \le t \le 0.9$.[24] In addition, the formation of a stable $[BX_6]^{4-}$ octahedron is probable when the value of μ lies between 0.442 and 0.895.[25] However, when compositions include heavier halides, the Goldschmidt tolerance factor cannot accurately predict the structural stability. Therefore, Scheffler *et al.* introduced a new tolerance factor, denoted as τ, defined as:[26]

$$\tau = \frac{R_X}{R_B} - n_A\left(n_A - \frac{R_A/R_B}{\ln(R_A/R_B)}\right) \tag{3}$$

where n_A represents the oxidation state of A and R_i represents the i ionic radii. When $\tau < 4.18$, perovskite lattices can form with an accuracy rate of 92%.[26]

2.2 Origin of defects

An impressive cost-efficiency ratio is one of the most significant advantages of LHPs. However, utilizing a low-cost solution-based method invariably renders the control of the nucleation and growth challenging, leading to the inherent formation of defects. Eqn (4) describes the formation energy $\Delta H(\alpha, q)$ for defect α in its charge state q.

$$\begin{aligned}\Delta H(\alpha, q) &= E(\alpha, q) - E(\text{host}) \\ &+ \sum_i n_i(E_i + \Delta\mu_i) + q[E_{\text{VBM}}(\text{host}) + E_F]\end{aligned} \tag{4}$$

In this equation, the energy difference between the two systems is defined by the total energy $E(\alpha, q)$ of a supercell with a defect at the charge state q and the inherent energy $E(\text{host})$ of an identical supercell devoid of the defect. The n_i and μ_i represent the number of atoms and atomic chemical potential, respectively, with q signifying the electron charge. E_i denotes the atomic energy of species i, and E_F represents the Fermi energy level. It should be noted that eqn (4) is applicable to thin-film materials, whereas defect formation in NCs adheres to the subsequent framework,

$$\Delta H_f^{NC}(\alpha + \alpha') = E[NC(\alpha + \alpha')] - E(NC) \pm E(s) \tag{5}$$

where α and α' denote the defect pair with opposite charges, and the last term in the equation represents the energy of the defective bulk NC and charge-neutral molecular species, respectively. The defect formation energy of thin films lacks universality because the chemical potential of NCs prepared in solution correlates with molecular ions rather than precipitates.[27] Defects often occur in pairs and evolve into ionic pairs in solution. ΔH is variable, subject to the influence of the growth environment, as illustrated in Fig. 2c.[28] $MAPbI_3$ constitutes a minor proportion at thermodynamic equilibrium and is substantially influenced by the alterations, as presented in Fig. 2d.

However, the origin of these defects is intricate. Overall, defect origins can be classified into inherent and external stimulation.

2.2.1 Inherent. Regarding passivation defects, intrinsic defects are predominant in perovskite materials. These intrinsic defects, which are closely related to the ABX_3 composition and unregulated crystallization growth, are both inherent and intricate. The selection of specific A-, B-, and X-site ions profoundly influences the perovskite structure. Different lattice

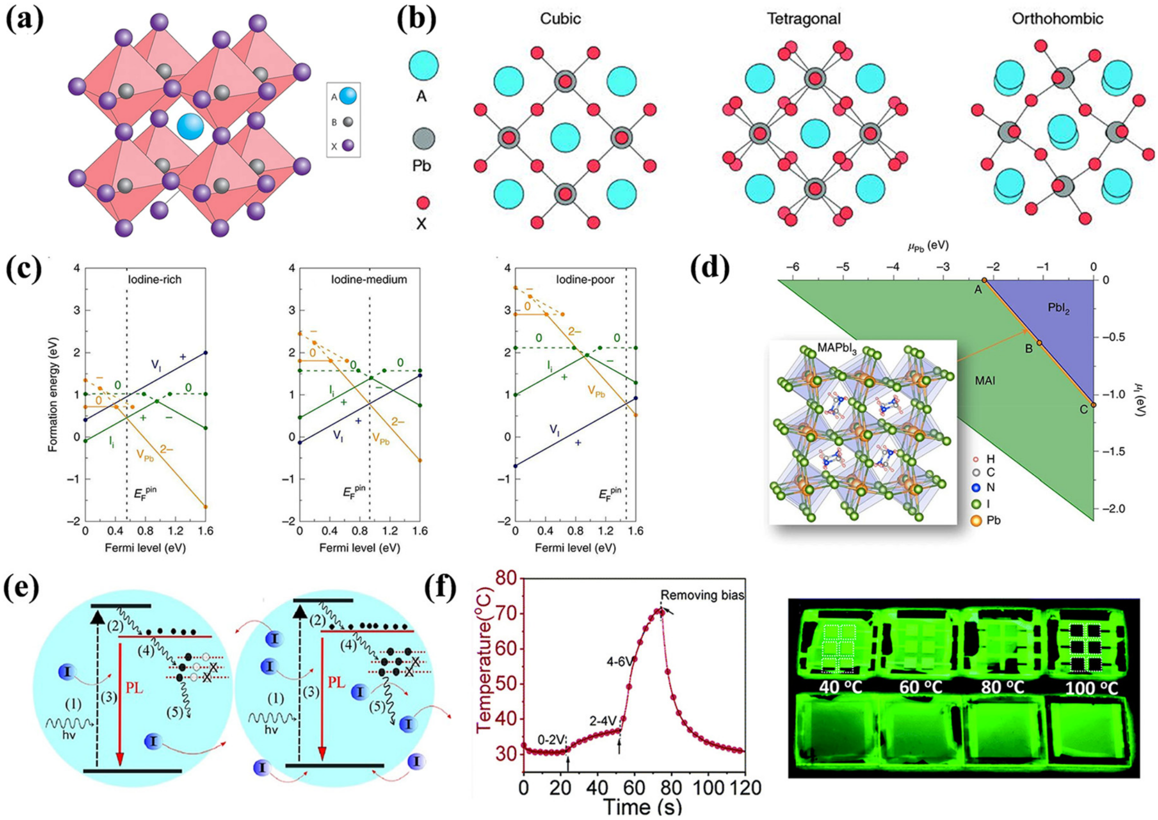

Fig. 2 (a) Schematic diagram of perovskite crystal structure. Reproduced with permission from ref. 23. Copyright 2014 Springer Nature. (b) Crystal structures of different phases of $APbX_3$. Reproduced with permission from ref. 27. Copyright 2021 AIP Publishing. (c) Formation energies of native defects under three representative growth conditions. (d) Thermodynamic equilibrium range of the perovskite $MAPbI_3$ growth conditions. (c and d) Reproduced with permission from ref. 28. Copyright 2021 Springer Nature. (e) Schematic dynamic processes at low excitation (left) and high excitation (right), involving defect trapping and detrapping, which determine the PL increment, and ion activation, migration, and accumulation, which determine the PL quenching. Reproduced with permission from ref. 32. Copyright 2016 Wiley-VCH. (f) Extracted device surface temperature against time curve (left) and photographs of a completed PeLED device (top) and a perovskite film covered by TPBi and LiF (bottom) subjected to annealing at different temperatures under 365 nm UV lamp illumination. Reproduced with permission from ref. 37. Copyright 2013 Royal Society of Chemistry.

compositions yield varying facets, and consequently, distinct defect types. For example, $CsPbX_3$ tends to form Cs and X vacancies. The challenging control process presents slight differences between the NCs and films. For NCs, imprecise management of nucleation and growth during preparation inevitably produces defects, significantly contributing to the poor performance of PeLEDs. Often, NCs surfaces are surrounded by ligands. Their dynamic association with the surface can lead to supplementary surface defects, impeding the NC storage and performance. However, polycrystalline films are typically produced using solution spin-coating and rapid thermal evaporation methods, which add complexity to the crystallization and growth stages. Hence, increasing research has focused on integrating additives during crystallization to enhance the perovskite crystallinity and mitigate film crack and void.

2.2.2 External stimulation.

Numerous studies have demonstrated the adverse effects of external environmental factors on the optoelectronic device performance, particularly the pernicious role on defects. Perovskite exhibit instability in the presence of humidity and oxygen, leading to notorious instability and decomposition issues. Adverse environmental conditions can induce and interact with defects. For instance, $MAPbI_3$, water-soluble, exhibits a pronounced vulnerability to moisture. Under humid conditions, water molecules infiltrate the lattice, establishing weak hydrogen bonds with MA^+, which in turn triggers crystal bond dissociation.[29] Similarly, exposure to oxygen leads to the adsorption of O_2 on the (100) surface of $MAPbI_3$ *via* van der Waals forces, generating positive surface charges and elevating the work function.[30] In both scenarios, incorporating an insulating layer within the device structure or encapsulating the device with a UV cured resin can improve the hydroxide stability. However, current research suggests that moderate levels of water and oxygen may not only be non-detrimental but may even enhance device performance. You *et al.* observed a significant reduction in defects when thermal annealing of the precursor occurred in a humid environment.[31]

Beyond the ambient air environment, external stimulation, such as sustained illumination, EF, and thermal field can intensify interactions with defects. Overall, the influence of field-induced defects in PeLEDs is complex and depends on defect density, material attributes, and environmental circumstances. Illumination has been identified as a factor that modifies the optoelectronic characteristics of perovskites and their devices. The PL of perovskite presents improvement, quenching, or remain constant under continuous illumination, depending on the density of intrinsic defect states in films produced by different methodologies, as illustrated in Fig. 2e.[32] An increase in PL implies defect de-trapping to a certain degree through curing under illumination, whereas a constant PL indicates ongoing saturation. Illumination exposure can lead to the emergence of photo-induced defects, which trap charge carriers, reducing device efficiency.[33] Additionally, light can induce ion migration, resulting in charge redistribution in the EML, a phenomenon that partially reverses in darkness.[34] Quilettes *et al.* concluded that the PL enhancement in dimmer grains considerably surpassed that in bright grains, due to iodide redistribution. In actual experiments, light and oxygen frequently co-influence devices. This is evident when $MAPbI_3$ degrades upon simultaneous exposure to light and oxygen through the formation of superoxide species.[35]

Joule heating is a crucial aspect in the operation of electroluminescent devices. However, a deeper understanding of its impact on PeLEDs stability remains elusive. Joule heating is associated with thermally activated ion migration and can inflict irreversible damage to the organic transport layer or interfaces.[36,37] Under a bias voltage of 6 V, the device can attain temperatures approaching 70 °C, as shown in Fig. 2f. In comparison, inorganic perovskites exhibit superior thermal stability compared to their organic–inorganic hybrid counterparts. Moreover, various temperatures cause phase transitions in perovskites. For $CsPbCl_3$, the transition temperatures from monoclinic to orthorhombic to tetragonal are 37 °C, 42 °C, and 47 °C,[38] respectively. Similar behaviors are observed in $CsPbBr_3$ and $CsPbI_3$.[39,40]

EF is more than a primary driving force of device operation, requiring a higher level of attention. Although current research on the influence of EFs on perovskite optoelectronic devices has predominantly focused on photovoltaics, LEDs remain understudied. Similar to the influence of illumination on perovskite materials, EFs also trigger ion migration and phase separation, leading to an increase in defects and degradation of the crystal structure.[41] The ionic properties of the octahedral "sub-lattice" within the perovskite framework facilitate the mobility of both positive and negative charged ions or vacancies under EF,[42] particularly V_X defects,[43] which behave akin to free carriers under sustained EF. In addition, EF can introduce new defects and alter the energy band structure. Studying the effect of EF on defect behavior remains limited, and will be the focal point of the ensuring chapter.

2.3 Classification of defects

As mentioned previously, defects can be caused by numerous sources and occur in a diverse range of types. Understanding these specific defect types facilitates identification of their origins and underlying formation mechanisms, enabling effective characterization and regulation. Based on distinct classification standards, these defects can be categorized as follows.

2.3.1 Dimensionality. Consistent with the different dimensionalities of the defects, they can be classified into zero-, one-, two-, and three-dimensional defects. Zero-dimensional defects typically refer to point defects, including vacancies (V_A, V_B, and V_X), interstitials (A_i, B_i, and X_i), and substitutions (A_B, A_X, B_X, X_A, and X_B), as illustrated in Fig. 3a.[44] Unlike zero-dimensional point defects, which are localized disruptions in the crystal lattice, higher-dimensional defects extend over larger regions. One-dimensional defects are linear in nature, such as dislocations or stacking faults, and do not encompass point-like characteristics. Two-dimensional defects correspond to planar disruptions like grain boundaries, as represented in Fig. 3b.[45] Three-dimensional bulk defects, such as pinholes, cracks, precipitates, and second-phase domains, have a pronounced tendency to cause irreversible damage to device performance.

2.3.2 Defect pairs. Generally, the interactions between different point defects can be referred to as defect pairs. Typically, defect pairs yield two primary classifications: Frenkel defects and Schottky defects (Fig. 3c).[45] A Frenkel defect arises when a cation, such as Pb^{2+} or Cs^+, leaves its standard lattice site to occupy an interstitial site, ensuring no net charge imbalance in the crystal. However, Schottky defects occur when a pair of oppositely charged ions is absent from their normal lattice sites, which affects the electrical conductivity of the perovskite. The fundamental distinction between them is that a Frenkel defect is derived from a single-ion type, whereas a Schottky defect originates from two unique charged vacancies.

2.3.3 Position within the bandgap. Defects are commonly categorized into shallow- and deep-level defects, based on the resistance level of the forbidden band. Defect states proximal to the valence band maximum (VBM) or conduction band minimum (CBM) are termed shallow-level defects, primarily functioning as carrier traps. Conversely, defect states within the bandgap are designated as deep-level defects, which can establish nonradiative recombination centers, thereby compromising the device efficiency. In general, interstitials and substitutions in LHP materials predominantly contribute to deep-level defects, while shallow-level defects are often associated with vacancies, notably V_X and V_A, and barely diminish transition efficiency.[46] However, it should be noted that this is not an ironclad rule, as certain vacancies (*e.g.*, V_{FA} in $FAPbI_3$) can act as deep charge traps,[47] suggesting that the specific nature and impact of defects can vary considerably depending on the specific LHP composition and structure. Surface defect passivation can efficiently mitigate shallow-level defects. As shown in Fig. 3d, vacancy-associated states in LHPs exhibit characteristics linked to the orbital interactions of X and Pb. Specifically, the interplay between Pb 6s and X 3/4/5p orbitals at the VBM gives rise to a bonding and an antibonding state, which is pivotal in determining the characteristics of the

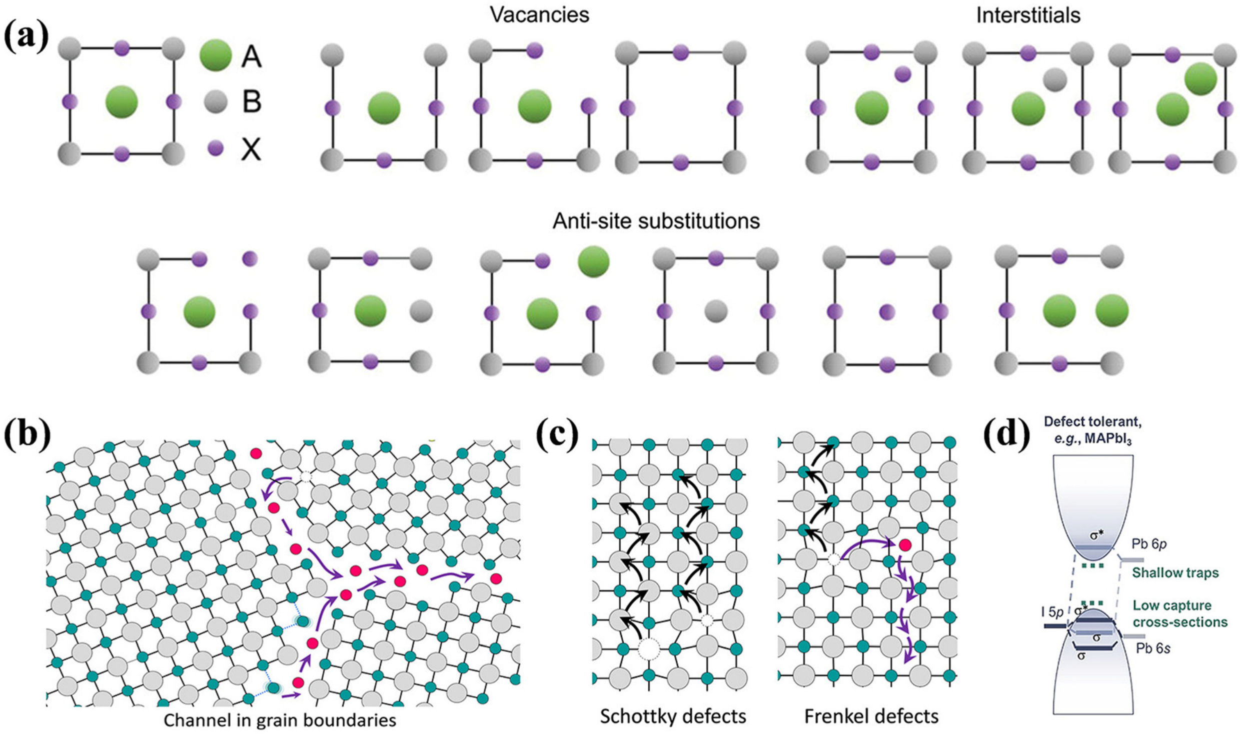

Fig. 3 (a) Scheme of vacancies, interstitials and anti-site substitutions in the perovskite lattice. Reproduced with permission from ref. 44. Copyright 2022 Wiley-VCH. (b) Open spaces and dislocations at grain boundaries. (c) Illustration of Schottky defects (left) and Frenkel defects (right). (b and c) Reproduced with permission from ref. 45. Copyright 2016 American Chemical Society. (d) Electronic structure of defect-tolerant materials (*e.g.* MAPbI$_3$), which primarily form shallow traps with low capture cross-sections. Reproduced with permission from ref. 13. Copyright 2021 Wiley-VCH.

valence band.[13] In the conduction band, the Pb 6p orbital hybridizes with the X 3/4/5p orbital, forming a bonding state at the VBM and an antibonding state at the CBM. This bonding feature emphasizes the shallow nature of these defect states. Calculations indicate that Cl-based produces present deep-level defects, whereas Br- or I-based structures predominantly exhibit shallow-level defects.[13,48]

2.4 Advanced characterizations of EF-induced defect behaviors

It is highly practical to reveal the behavior of defects in metal halide PeLEDs, as it is closely correlation with the device performance and optoelectronic properties. To date, there have been few characterization techniques employed to directly identify defect states. In addition, most defect behavior assessments are typically inferred from variations in the device performance, either enhancement or degradation. As previously mentioned, defects range from low- to high-dimensional types, arising from internal or environmental factors. Device performance parameters shift as the defect density is reduced through passivation or ligand-engineering strategies. This section summarizes the pivotal methods for characterizing defect behaviors, including microscopic, spectroscopic, and electrical measurements, and elucidates how these methods assess defect status alterations caused by minimized non-radiative losses. The manner in which these characterizations with defects deserves further study.

2.4.1 Microscopic measurements. Compared to other techniques, microscopy measurements can be relatively intuitive insights into understanding and deducing the movement and distribution of defects, thus laying the foundation for defect comprehension. Common measurement methodologies include: (i) optical microscopes can usually directly observe macroscopic defects of larger sizes, such as cracks, holes, and the like;[49] (ii) confocal fluorescence microscopy has notable contrast variations between effectively passivated and unpassivated defect zones, which in turn respond to changes in defects;[50] and (iii) conductive atomic force microscopy (c-AFM), which indirectly reflects defect status *via* localized conductivity shifts due to diverse electronic states.[51] For instance, currents at grain boundary frequently exceed those at grain surfaces, aligning with the existing understanding. Techniques affording enhanced precision include Kelvin probe force microscopy (KPFM) and scanning tunneling microscopy (STM).

Kelvin probe force microscopy (KPFM). KPFM, a derivative of AFM, is a non-contact technique for measuring the surface potential. It leverages the potential difference between the probe and the sample surface to obtain the surface potential distribution,[52] which is an indirect method to characterize the presence and nature of defects. By initially mapping the surface topography with AFM and maintaining a fixed probe

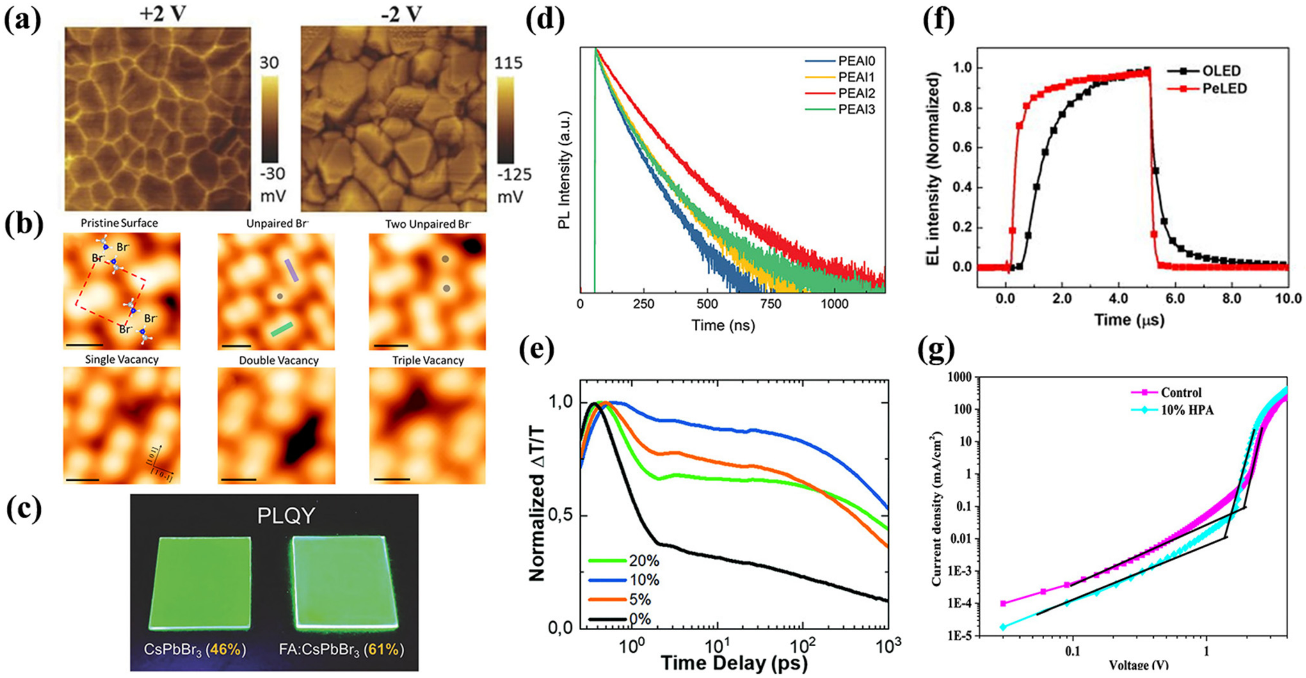

Fig. 4 (a) CPD mapping images in the dark after applying positive bias (left) and negative bias (right). Reproduced with permission from ref. 54. Copyright 2016 Wiley-VCH. (b) Intrinsic defects on the surface of $MAPbBr_3$ monitored by STM. Reproduced with permission from ref. 57. Copyright 2019 American Chemical Society. (c) Highly luminescent, smooth, and compact NC films, featuring a photograph of high bright $CsPbBr_3$ and FA-doped $CsPbBr_3$ NC films. Reproduced with permission from ref. 59. Copyright 2018 Wiley-VCH. (d) TrPL decay curves of $FAPbI_3$ NCs treated with various PEAI concentrations. Reproduced with permission from ref. 62. Copyright 2022 Wiley-VCH. (e) Comparison of initial carrier recombination of $CsPb_{1-x}Mg_xBr_3$ perovskite films with different $MgBr_2$ concentrations deposited directly on quartz. Reproduced with permission from ref. 65. Copyright 2016 Royal Society of Chemistry. (f) TrEL of OLED and PeLED at the 5 V. Reproduced with permission from ref. 72. Copyright 2019 AIP Publishing. (g) Current density–voltage characteristics of hole-dominated devices with a control perovskite or 10% HPA layer. Reproduced with permission from ref. 75. Copyright 2022 American Chemical Society.

height, the potential difference, V_{CPD}, between the probe and the sample surface can be determined.[53] KPFM measures the electrostatic forces of samples using an externally applied alternating voltage (V_{AC}) and bias (V_{DC}), generating a surface potential map. In Fig. 4a, increased V_{CPD} at grain boundaries emerged under positive voltage from defect-induced ion accumulation, while efficient ion extraction under negative voltage reduced V_{CPD}.[54] However, it should be noted that variations in surface potential may not only originate from hole or electron traps affecting the local charge distribution but also be influenced by the chemical composition of the material, surface roughness, other electronic effects, environmental conditions, and so on. It is often necessary to combine other characterizations to analyze defect states accurately.

Scanning tunneling microscopy (STM). This high-resolution technique enables visualization of surface structures at the atomic scale, capturing both the electronic and morphological attributes of LHPs.[55] When integrated with density functional theory (DFT), it elucidates surface and sub-surface structures, accentuating the interface properties. For a tunneling current to be obtained, probe-to-surface distance should be less than 1 nm.[56] As Stecker *et al.* revealed that in $MAPbBr_3$, single unpaired Br^- was caused by pair orientation mismatches and, with the assistance of vacancies, further associate with Br neighbors to form two unpaired Br^-.[57] Moreover, single, double, and triple vacancies could be clearly appeared as dark depression at atomic scale in STM images (Fig. 4b). In STM testing, the preparation and cleanliness of the sample surface significantly impact the measurement results, and care should be taken to identify artifacts caused by changes in local charge distribution due to inhomogeneous sample surfaces or contamination. When comparing test results side-by-side, attention should be paid to probing information, scanning parameters, *etc*.

2.4.2 Spectroscopic measurements

Photoluminescence quantum yield (PLQY). Generally, the PLQY is a key parameter affected by carrier recombination kinetics in LHPs, which can be described as the quotient of the radiative recombination rates to the rates of overall recombination in eqn (6):[5]

$$\mathrm{PLQY} = \frac{\sum R_\mathrm{r}}{\sum R_\mathrm{r} + \sum R_\mathrm{nr}} \tag{6}$$

$$\mathrm{PLQY} = \frac{Bn^2}{An + Bn^2 + Cn^3} \tag{7}$$

$$\mathrm{PLQY} = \frac{k_\mathrm{ex} n}{(k_\mathrm{ex} + k_\mathrm{trap})n + k_\mathrm{Aug} n^2} \tag{8}$$

where R_r and R_{nr} represent radiative and nonradiative recombination, respectively. The eqn (7) often appears in 3D LHPs with lower exciton energy (E_b), where An indicates trap-assisted nonradiative monomolecular recombination, Bn^2 refers to the bimolecular radiative recombination of free charge carriers, and Cn^3 corresponds to three-body Auger recombination. Changes in carrier density at different fluence levels have a significant effect on PLQY. Meanwhile, the formation of stable excitons is realistic due to the presence of quantum confinement in low-dimensional LHPs. Therefore, in low-dimensional LHPs, radiative recombination is mainly driven by monomolecular excitonic recombination, as shown in eqn (8).[6] Among them, k_{ex} represents the first-order radiative monomolecular recombination rate, k_{trap} stands for the first-order nonradiative monomolecular recombination rate, k_{Aug} is the second-order nonradiative recombination rate, and n is the charge-carrier density. The Auger process has a pronounced reliance on the carrier density. At low excitation densities, where the contribution of the Auger process becomes negligible, the PLQY adheres to the ratio $k_{ex}/(k_{ex} + k_{trap})$, a value that maintains independence from the density of excitation. However, Auger recombination begins to manifest its significance at the high density of carriers, which in turn affects PLQY. With a high molar absorption coefficient, NCs feature excitation overlap regions that facilitate significant excitation light absorption for light conversion.[58] On this basis, perovskite nanocrystals (PNCs) often exhibit high PLQY, creating the requirements of emerging displays. The PLQY of perovskite polycrystalline films or NCs can be applied as a metric for recombination losses influenced by various elements, notably bulk and multilayer film interface defects. Absorption and fluorescence reabsorption of the sample may lead to measurement errors in PLQY. The uniformity and thickness of the perovskite films, as well as the dispersion of the NCs, have a significant effect on the PLQY results. Moreover, perovskite materials may undergo phase transition under light exposure and temperature changes, leading to inaccurate test results. As depicted in Fig. 4c, Zeng *et al.* effectively optimized $CsPbBr_3$ NCs, achieving an impressive PLQY > 90% using a room-temperature triple-ligand surface engineering approach.[59] Moreover, a partial substitution of the A-site with FA^+ increased the PLQY of PNCs films from 46% to 61%, signifying fewer nonradiative recombination centers attributable to defects. The merit of defect reduction leading to enhanced PLQY was confirmed by green PeLEDs leveraging $CsPbBr_3$ NCs with a high EQE of 11.6%.

Time-resolved photoluminescence (TrPL). TrPL is a transient decay assessment method used to analyze charge carrier recombination dynamics, indirectly indicating the extent of defect formation in NCs or films. Typically, the TrPL decay is modeled using the rate equation:[5,60]

$$-\frac{d_n}{d_t} = k_1 n + k_2 n^2 + k_3 n^3 \qquad (9)$$

$$-\frac{d_n}{d_t} = k_{trap} n + k_{ex} n + k_{Aug} n^2 \qquad (10)$$

where k_i (i = 1, 2, 3, trap, ex, Aug) corresponds to the rate constants and n represents the concentration of carriers. To some extent, PL decay curves can respond to nonradiative recombination processes. Particularly, in 3D LHPs with a low E_b, rate equation can be explained by eqn (9), where k_1, k_2, and k_3 correspond to the rate constants for monomolecular, bimolecular, and Auger recombination, respectively. However, for 2D, quasi-2D, and NCs, the charge carrier recombination dynamics process can be described by eqn (10). In the case of NCs, two competing processes are involved in monomolecular recombination: exciton radiative recombination ($k_{ex}n$) and nonradiative recombination assisted by traps ($k_{trap}n$).[60] In the TRPL test, which has a fluence dependence, excitation density determines the charge-carrier density in the LHPs. Whether or not the Auger recombination can be neglected depends on the carrier density. Upon the low excitation density, the decay of PNCs is predominantly mediated by defect-assisted recombination, exhibiting a rapid decay rate. As excitation density increases, defect occupancy is initiated, followed successively by exciton radiative recombination and Auger recombination processes.[61] Wong *et al.* employed a post-treatment involving encapsulation of $FAPbI_3$ NCs with 2-phenylethylammonium iodide (PEAI).[62] The resultant TrPL curves indicated a reduction in surface vacancies for PEAI-passivated NCs (Fig. 4d). An extended PL lifetime, coupled with a PLQY of up to 61.6%, was achieved through the enhancement of film crystallization quality and carrier transport performance. TrPL-based analyses provide insights into exciton formation and the behavior of free carriers, but they lack the capability to distinguish between excitons and free carriers. To a certain degree, TrPL can be an indicator of the defect density throughout the device, which has a profound correlation with EQE, containing defects in the bulk or at interfaces. However, detector response time and resolution limitations are key challenges in TrPL, which are crucial for accurately capturing rapid dynamic processes in perovskites. However, photodegradation of perovskites may occur under prolonged light or high-intensity excitation, potentially affecting TrPL measurements. The photophysical properties of perovskites may change with temperature, making temperature control and recording important in TrPL measurements.

Transient absorption spectroscopy (TA). TA spectroscopy, also known as ultrafast transient absorption or pump–probe technology, has been employed to investigate the carrier transport dynamics in bulk perovskite materials or films. This provides insights into charge extraction from device interfaces and energy transfer from excited states. The nomenclature "pump–probe" arises from the dual-pulse measurement technique involving distinct pump and probe pulses. The regenerative amplifier generates a pulse beam that is subsequently bifurcated. The majority of the beam serves as the pump pulse, while a lesser fraction is converted into weak broadband white light, designated as the probe pulse.[61] Both the high-energy pump beam and broadband white light probe beam sequentially irradiate the sample. This transition shifts the sample from the ground state to an excited state upon pump-light excitation. Therefore, TA spectroscopic measurements commonly comprise signals from excited state absorption (ESA), ground-state bleaching (GSB), and stimulated emission (SE).[63] The TA curve captures both the detection and reference light signals, with or without the pump pulse, and includes ΔA and ΔT signals. The ΔA signal, which is calculated as the difference in absorption spectrum between the excited and ground states, can manifest as either a positive or negative value. This signal serves to probe the temporal evolution of photoexcited states,[63]

$$\Delta A = -\log \frac{\left[I(\lambda)_{pro} - I(\lambda)_{\mathrm{ref}}\right]_{\mathrm{pump}}}{\left[I(\lambda)_{pro} - I(\lambda)_{\mathrm{ref}}\right]_{\mathrm{unpump}}} \tag{11}$$

where I means the light intensity, $I(\lambda)_{\mathrm{pro}} - I(\lambda)_{\mathrm{ref}}$ signifies the difference between the probe pulse intensity and the reference pulse intensity, and the numerator and denominator refer to the sample under the irradiated pump pulse or not. Moreover, the ΔT signal is defined as the ratio of transmission to incident light, and is commonly expressed as the normalized $\Delta T/T$. This metric can manifest as either a positive or negative value, indicative of photoinduced transmission or absorption, respectively.[64]

TA spectroscopy is a powerful tool for monitoring carrier relaxation by capturing variation data in light absorption or reflection in time and space, which is enabled by the interplay between pump and the probe light pulses. This method has revolutionized the study of microscopic defect dynamics in various optoelectronic devices, including photovoltaics, LEDs, and optoelectronic detectors. Nevertheless, choosing different excitation intensities and wavelength conditions produces varying results regarding the intensity and dynamics of the TA signal. Sample treatment (*e.g.*, preparation method, film thickness) and testing environment (*e.g.*, temperature, atmospheric conditions) before TA tests also affect results. Researchers should exclude nonlinear effects and sample degradation as much as possible before interpreting TA signals. Sun *et al.* demonstrated a reduction in defect density in $CsPbBr_3$ perovskite by partially substituting Mg^{2+} for Pb^{2+}, as confirmed through TA spectroscopy and TrPL.[65] As shown in Fig. 4e, the incorporation of Mg^{2+} led to a slower relaxation rate of the initial peak upon photoexcitation, typically occurring on the picosecond (ps) scale. This reduced relaxation rate is indicative of decreased nonradiative recombination channels and suggests improved perovskite morphology along with a significant reduction in defect density, as corroborated by TrPL data.

Thermal admittance spectroscopy (TAS). Charged defects have a notable influence on electronic performance and capacitance properties. TAS predominantly focuses on monitoring capacitance fluctuations associated with defect density to glean insights into both deep-level and shallow-level defects.[63] Applying an alternating EF, defect information can be obtained by scrutinizing alterations in capacitance. However, TAS is constrained in its ability to map the spatial distribution of defects. Under illumination, specific electronic defect states capture photogenerated electrons. Modulating the frequency of the alternating current instigates the release of these photogenerated electrons, thereby generating admittance signals.[66] Conducting TAS at varying temperatures enables the elucidation of defect density and energy distribution in semiconductor materials, with distinct defects corresponding to specific capacitance metrics.[67] Through TAS analysis, the defect capture state density (tDOS) can be quantified. Common challenges with TAS include the precision of temperature control and the selection of frequency response, where different frequencies may reveal distinct defect types and charge transfer mechanisms. Measurement artifacts that may be caused by ambient electromagnetic interference, poor sample contact, or instrumental noise should be excluded when analyzing the data and focusing on temperature dependence. When necessary, compare and contrast the results with other test methods (*e.g.*, DLTS). Huang *et al.* compared the passivation effects of PCBM and choline chloride (ChCl) on LHPs and determined that ChCl exhibited a lower aggregate tDOS.[68] Devices treated with ChCl displayed a shallow-level trap state density approximately threefold lower than that observed in PCBM-treated devices (0.35–0.40 eV), signifying the effective passivation of defects at grain boundaries by ChCl.

2.4.3 Electrical measurements

Deep-level transient spectroscopy (DLTS). DLTS offers heightened sensitivity, simplified operation, and an extended detection range for identifying deep-level defects.[63] DLTS employs time-domain capacitance measurements for the comprehensive characterization of defects, yielding vital data on their energy levels, concentrations, and charge states. Initially, charge carriers are introduced into the sample *via* illumination or voltage pulses and captured at deep-level defect sites, thereby inducing transient charge states. These charge states undergo time-dependent charging or discharging processes, which rely on the charge state of the deep-level defects kinetics monitored through real-time capacitance measurements of the sample. The DLTS can quantify the ionization energy of deep-level defects, thus analyzing their energetic depth. Furthermore, the rate and magnitude of the charging and discharging events serve to estimate the deep-level defects concentrations, facilitating an understanding of the defect distribution within the material. The sensitivity of the instrument may limit the identification of electron traps and deep defects. Care should be taken when analyzing DLTS data to identify and differentiate between electron traps and deep defects. Comparative DLTS studies on films prepared *via* one-step and two-step methods revealed that the one-step method yielded a higher density of defects.[69]

Transient EL (TrEL). The TrEL technique leverages the luminescent properties of materials under EF excitation to investigate and characterize defects. In a typical TrEL experiment, short-pulse EF excites the sample, leading to the generation or injection of charge carriers. These carriers traverse the material and interact with defects, subsequently resulting in radiative recombination and emitting visible light.[70] Time-resolved spectral analyses elucidate key parameters, such as onset time, luminescence intensity, and lifetime, offering insights into defect properties, including charge carrier capture and release rates, defect concentration, and energy level structure. Quantification of charge carriers is attainable through temporal integration of EL during the slow decay phase, allowing for an approximate calculation of defect density (n_t), using a specific mathematical equation:[71]

$$n_t = -\frac{V_{bi}}{q\omega_0}\frac{dC}{d\omega}\frac{\omega}{k_B T} \tag{12}$$

where V_{bi} means the built-in EF, ω represents the angular frequency, q serves as the elementary charge, ω_0 produces the depletion width, k_B performs the Boltzmann constant, and T shows the temperature. Fig. 4f illustrates that the decay rate of TrEL was substantially higher than that of OLED upon voltage termination, thereby indicating a reduced trap density in MQW perovskite as compared to OLED.[72]

Space-charge-limited-current (SCLC). The SCLC method is frequently employed to evaluate key parameters such as conductivity, carrier concentration, mobility, and defect density.[73] Charged defects can capture free charges, decrease the number of free carriers, and induce alterations in the electrical properties when the defects become saturated. Because the space-charge effect limits the current, the *I–V* curve, commonly partitioned into three distinct regions, including ohmic, trap-filled limit, and Child region, serving as a basis for determining defect density.[74] In the low-voltage ohmic region, the curve is linear, which is attributable to defect sites being filled with the injected charge. Upon saturation of these defects, the injected charge carriers can move in the material unhindered, resulting in a rapid increase current and transition to a low-resistance state. The voltage at this point, is denoted as the trap-filled limit voltage (V_{TFL}), which facilitates the calculation of the defect density *via* a specific equation:

$$N_t = \frac{2\varepsilon_0\varepsilon_r V_{TFL}}{eL^2} \tag{13}$$

where L, ε_r, ε_0, and e represent the thickness of the MHP film, the dielectric constant of the material, permittivity of vacuum, and electronic charge, respectively. However, the quality of the sample interface and electrode contact are critical to SCLC testing. The caveat explained is to consider the effect of contact resistance and sample homogeneity on SCLC measurements. Inconsistencies in perovskite film thickness may lead to difficulties in interpretation. Analysis of the SCLC curve presented in Fig. 4g determined that the defect density in the quasi-2D film with hypophosphorous acid (HPA) was 1.55×10^{17} cm^{-3}, which was less than the 2.19×10^{17} cm^{-3} observed in the pristine film.[75] This demonstrated that the inclusion of HPA served as an effective passivating agent for defects.

2.4.4 Additional measurements

Time-of-flight secondary-ion mass spectrometry (TOF-SIMS). TOF-SIMS is a sophisticated surface analytical mass spectrometry technique offering detailed insights into the composition and distribution of elements and molecules on the perovskite film surface, grain boundaries, and interfaces in an entire device stack.[76] TOF-SIMS, delivering high-resolution depth profiling, imaging, and 3D tomography, is utilized in PeLEDs to produce evidence of ion migration behavior, indirectly characterizing the formation of defects. This is mainly due to the fact that defect regions may exhibit a different elemental composition or chemical state than surrounding material, thus indirectly reacting to the formation of the defect. Moreover, defects sometimes accumulate at the surface or interface of the perovskite, and by analyzing the inhomogeneous elemental distribution in these regions, the characteristics and distribution of the defects can be revealed. TOF-SIMS can track the distribution of specific ions (*e.g.*, Pb^{2+} and I^-) in PeLEDs, thus revealing ion migration paths often associated with internal defects. TOF-SIMS functions through the bombardment of the sample's surface with a high-energy primary-ion beam (≈30 keV), initiating a collision cascade and disrupting molecular bonds within the material, which results in surface material removal without inducing bulk sputtering.[76] The bulk sputtering is a second low-energy ion beam (≤1 keV), which enables depth profiling. A minor portion of the ejected material becomes charged, allowing for precise mass analysis of these charged secondary ions. In depth profiling, primary-ion beams lead to oversampling with higher energy, and removing damaged material is insufficient to remove the beam damage following each round of sputtering damage to the organic material underneath in PeLEDs, which keeps accumulating, producing beam damage artifacts. Lee *et al.* utilized TOF-SIMS to track the penetration depth of small molecules on perovskite films after post-treatment, determining that ethylenediamine (EDA) can more effectively passivate surface defects and reduce nonradiative recombinations.[77]

In situ characterization. In order to accommodate the dynamic micro-level processes associated with LHPs, techniques for *in situ* characterization of ion migration and defect formation are rapidly advancing. *In situ* transmission electron microscopy (TEM) enables the real-time monitoring of microstructural alterations in perovskite materials and devices, particularly under specialized conditions like thermal fields and EFs, offering more relatively direct visual confirmation crucial for comprehending the mechanisms of ion migration and defect formation. Utilizing high-angle annular dark-field (HAADF) imaging of the *in situ* TEM, the devices showed shrinkage at the EML/hole transport layer (HTL) interface and appeared nanoparticles at structural defects present in the HTL itself as well as at the interface under continuous bias.[78] Enhanced contrast in these regions provides confirmation of ionic migration involving heavy metal elements. Hu *et al.* used *in situ* UV-vis absorption spectroscopy combined with SEM to visualize defect formation indirectly. Their findings indicated that introducing nitrogen at the onset of crystallization enhances the film quality and device performance, in contrast to its application during the intermediate stage, which was observed to induce defects and cracks.[79] While *in situ* characterization offers valuable insights, it concurrently presents specific challenges, such as the inherent instability of LHPs.

Moreover, the electron beam in *in situ* TEM can induce unintended precipitation of lead within LHPs, potentially skewing the results. A synergistic approach is often adopted to alleviate these issues, integrating additional testing methodologies to provide a more comprehensive and accurate understanding of the phenomena under study.

3. Electric field-induced defect behaviors

It is widely acknowledged that defects in perovskite materials, which are crucial for optoelectronic stability, are susceptible to various forms of external stimulation, including water, oxygen, light field, EF, and thermal field. The manner in which these environmental factors induce defect states remains controversial, and existing conclusions are inconsistent. The study of the effects of humidity and oxygen on perovskite-based devices has yielded insights into both the advantageous and disadvantageous effects. Among these external factors, the EF related to device operation is a persistent issue that warrants critical attention. Dating back to the foundational research of Varignon *et al.*, the role of EF in shaping the properties of intrinsic perovskite materials has been explored, despite EF being an essential driving force in EL devices. Notably, this work identified that EF can modulate Jahn–Teller distortions in specific perovskite materials such as $SrTiO_3$, $BaMnO_3$, $YMnO_3$, and $BiFeO_3$.[80] Typically, the defect formation sites are firstly affected by the EF. However, the behavior of defects induced by external EFs has a complex debate on intrinsic materials and devices, which hinders the advancement of EL devices. Many studies have focused on reducing the adverse effects of defects, although there is a marked absence of comprehensive investigations into the intrinsic behavior of defects under EF conditions. Therefore, it is imperative to conduct focused research to elucidate the influence of EF on defect dynamics within operational perovskite materials and devices.

3.1 Ion migration

Recently, EF-induced ion migration has garnered significant attention in the realm of perovskite materials and LEDs due to their association with both device performance and stability.[81] Within an external EF context, ion migration often either a manifestation of defects[43] or mediated by them,[82] plays a double-edged sword role in halide perovskite-based electronic devices. Although mobile ions contribute to spectral impurities and compromise the stability of PeLEDs, they also have potential to partially heal defects, thereby enhancing the device performance. This section offers a nuanced perspective of the complexities of ion migration in EL devices.

3.1.1 Relationship between ion migration and defects. The phenomenon of ion migration in LHPs has its origins in perovskite solar cells (PSCs), accounting for anomalies in low-frequency dielectric constant and hysteretic behavior.[83] Mobile ions can generally be categorized into two types: ionic defects inherent in the material and excess ions derived from the precursors. As outlined in Section 2.3, ionic defects often take the form of point defects that emerge during crystallization owing to inherent softness of the material, even without external stimulation. However, ion migration is predominantly facilitated by these point defects, which enhance the rate of ion movement through mechanisms such as ion hopping.[82] Due to the complexity and variability in measurement and calculation methodologies, a definite, fixed value for the ionic defect activation energy (E_a) is generally elusive. The value of E_a can be used to describe the trend and rate of ion migration. In addition, E_a is not consistently correlated with factors such as composition, grain size, strain, and solution environment.[44] The E_a of the mobile ions obtained by measurement and calculation methods is briefly summarized in Table 1. Notably, the E_a values for A- and X-sites are lower than those for B-sites, corresponding to shallow- and deep-level defects, respectively. The relatively low E_a serves as a driving force for the directional migration of ionic defects, particularly under the influence of an external EF.

In contrast to PSCs that utilize standard stoichiometry, PeLEDs often employ excess halide salts to maintain their lattice integrity. Therefore, similar to the doping strategy, a precursor with excess salt serves surplus ions resulting in more defects. Moreover, regarding the thinner EML and stronger EF than PSCs, the oscillation of various ions in response to a reversing EF is a non-negligible factor, as illustrated in Fig. 5a.[84] Upon voltage application, mobile ions initially fill

Table 1 Summarized E_a in LHP materials and devices

Material type	Mobile species	Methods	E_a [eV]	Ref.
$MAPbI_3$	V_{MA}	DLTS	0.37	86
	MA_i		0.37	
	I_i		0.19	
$MAPbI_3$	I^-	Transient ion-drift measurements	0.29 ± 0.06	87
	MA^+		0.39–0.9	
$MAPbI_3$	—	Temperature dependence of the conductivity	0.43	83
$(FA/MA/Cs)Pb(I/Br)_3$	—	TAS	0.282	88
$MAPbI_3$	I^-	Temperature dependence of PL	0.14 ± 0.03	89
$CsPb_{1-x}Cd_xBr_3$	—	Temperature dependence of PL	0.225	90
$MAPbI_3$	MA^+	Temperature dependence of the impedance	0.58	91
$MAPbI_3$	V_i	DFT	0.08	92
	V_{MA}		0.46	
	V_{Pb}		0.8	
	I_i		0.08	
$MAPbBr_3$	V_{Br}	DFT	0.09	92
	V_{MA}		0.56	
$MAPbI_3$	V_I	DFT	0.58	93
	V_{Pb}		2.31	
	V_{MA}		0.84	
$MAPbI_3$	V_I	DFT	0.32	94
	V_{MA}		0.57	
$FAPbI_3$	V_I	DFT	0.55	94
	V_{MA}		0.61	
$MAPbI_3$	V_I	MD	0.1	95
	I_i		0.24	
$CsPbI_3$	V_I	DFT	0.36 (0.29)	96
	V_{Cs}		0.59 (1.16)	
	V_{Pb}		0.81 (0.99)	

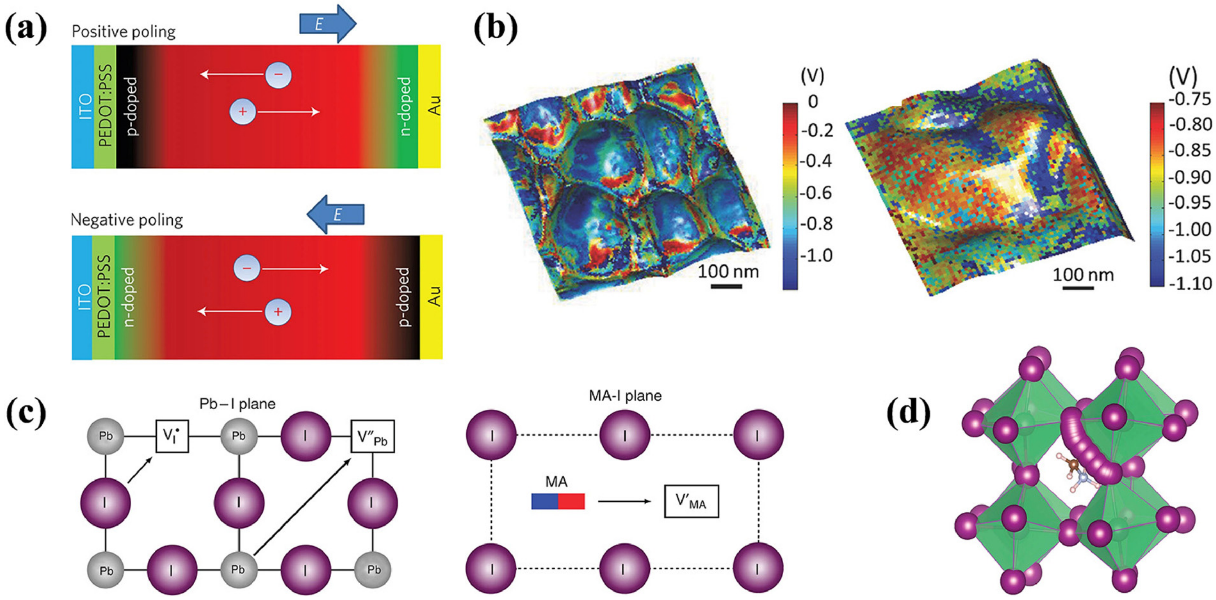

Fig. 5 (a) Schematics of ion drift in perovskite during positive and negative poling, respectively. Reproduced with permission from ref. 84. Copyright 2014 Springer Nature. (b) Potential difference (surface charge) superimposed on topographic image of the $CH_3NH_3PbI_3$-only perovskite film (left) and thermally annealed perovskite/PCBM film (right), acquired using the BE-KPFM technique. Reproduced with permission from ref. 99. Copyright 2017 Wiley-VCH. (c) I^- migration along an octahedron edge and Pb^{2+} migration along the diagonal direction ⟨110⟩ (left), while MA^+ migration into a neighboring vacant A-site cage (right). (d) Theoretical calculation results of migration paths indicating a slightly curved path and local relaxation/tilting of the octahedra. (c and d) Reproduced with permission from ref. 93. Copyright 2015 Springer Nature.

the trap, temporarily enhancing the EQE and PL intensities of the device. Under conditions of sustained high current density, irreversible ion migration and accumulation lead to more defects and Joule heat generation, subsequently exacerbating ion migration and causing a decline in the device efficiency. According to the operating principle of PeLEDs, electrodes on both sides continuously inject electrons and holes into the electron transport layer (ETL) and HTL, respectively, under an external field. This electron–hole activity, in conjunction with vacancies in the EML, limits opportunities for beneficial interactions between mobile ions and defects, thereby exacerbating ion migration.[85]

3.1.2 Ion migration paths under electric fields. The paths of ion migration depend on various factors, including material properties, EF strength, and ion mobility rates. Furthermore, diverse defective environments result in distinct migration behaviors of different ions, leading to numerous migration trends. Based on previous reports, ion migration pathways can be broadly classified into two categories: those occurring within the bulk material and those relevant to the device architecture.

Grain boundary (GB). To passivate defects, excess halide salts are incorporated during the fabrication of the perovskite layer,[97] a substantial fraction of which fails to integrate into the lattice, instead residing at GB or surface sites.[98] These provide channels for more ion mobility. Yun *et al.* demonstrated that ion migration at GBs occurs at a faster rate than that within grain interiors (GIs), as assessed by KPFM.[54] This accelerated migration is attribute to the rapid ion mobility at GBs. Various factors, such as GB composition and structure, temperature, and applied EF, can exhibit influence on the GB which serves as ion migration "highways". Yang *et al.* employed innovative, open-loop, band-excitation, (contact) Kelvin probe force microscopy (BE-KPFM and BE-cKPFM) techniques to compare ion migration across GBs with different compositions (Fig. 5b).[99] They confirmed that the introduction of [6,6]-phenyl-C_{61}-butyric acid methyl ester (PCBM) reduced ion migration, whereas the presence of additional mobile Cl^- ions at GBs enhanced it. The GB are the result of crystallization process in which the perovskite material grows in multiple domains; the boundaries between these domains retain partial chemical bonds, thereby requiring a lower E_a for migration than the bulk material.

Interface. Upon the application of an EF across the device, a force is exerted on the ions, instigating their movement not only within the EML but also throughout the perovskite materials. This leads to pronounced ion migration at the device interfaces. Additionally, the halide ions exhibit a strong affinity for electrode materials,[100] exacerbating ion migration at the interface, as corroborated by the detection of halide ions in the transport layer. Concurrently, the electrode introduce metal ions into the device under the influence of the EF, resulting in the formation of Pb^0 through a redox reaction.[101] In this context, mobile ions undergo redistribution within the EML, establishing an internal EF (E_{ion}). When multilayer films are incorporated into device designs *via* straightforward solution-based processes, these interfaces serve as additional pathways for ion migration owing to the introduction of new defects.

Bulk defect. The migration pathways of ions can vary. Taking the ion transport mechanism in the $MAPbI_3$ perovskite structure as an illustrative example, theoretical calculations suggested that mobile ions generally preferred direct linear jumps between adjacent sites, as depicted in Fig. 5c.[93] Specifically, I^- migrated of along octahedral cages, Pb^{2+} traversed the diagonals of cubic unit cells in the ⟨110⟩ direction, and MA^+ relocated to adjacent empty A-site cages. However, a detailed investigation of the migration pathways for I^- vacancies revealed a slight deviation from a strictly linear route, featuring a curved trajectory with a saddle point offset from the neighboring Pb^{2+}, as presented in Fig. 5d. Ion migration within bulk materials is further complicated by lattice dislocations, in addition to the typical elemental defects.[102] The presence of these dislocations distorted the crystal lattice, effectively reducing the energy barriers that would otherwise hinder ion migration. This allowed ions to traverse the lattice more expeditiously along paths, dislocation mechanism commonly referred to as "dislocation-mediated ion migration".

Surface defect. Due to their reduced dimensions, PNCs exhibit a high specific surface-to-bulk ratio, rendering the surface critical in ion migration. The underlying mechanisms for surface ion migration can be more intricate than those in the bulk and are influenced by multiple factors, such as material composition, NCs size and shape, and environmental conditions. Surface defects include a broader range of features than bulk defects, such as vacancies, interstitials, anti-site defects, surface states, surface reconstructions, and charges arising from dangling bonds. Leppert *et al.* revealed through DFT studies that Br vacancy migration barrier in cubic $CsPbBr_3$ bulk was approximately twice that of surface migration, attributing this difference to more room for variations in surface bond lengths.[103] Similar studies have been reported in other studies, indicating that the activation energy of migration for surface V_{Br} is nearly 0.3 eV lower than in bulk material.[104] However, Meggiolaro *et al.* noted that I_i is largely unaffected by surface conditions.[105] Surface defects serve as additional sites for ion migration for several reasons: (i) the surface is inherently more prone to defects; (ii) the disparity between surface and bulk properties drives ion migration along the surface; and (iii) the surface charge can either attract or repel ions, thereby influencing ion migration behavior.

3.1.3 Electric-field induced ion migration effects on device performance

Luminance overshoot. Experimental observations of "luminance overshoot", depicted in Fig. 6a, suggest an initial boost in luminance prior to a decline, when the effect of EF on device performance are studied.[82] This is supported by the work of Zhao *et al.*, who demonstrated that EF significantly improves the efficiency of $MAPbI_3$ LEDs through repeated electrical scans, as shown in Fig. 6b.[106] This is attributed to mobile ions initially filling local defects, thereby decreasing nonradiative recombination. However, luminance overshoot can be misleading as it might be misconstrued as an indication of permanent performance gains, which is not the case. Long-term repeated electrical scans can render perovskite lattice sites mobile, subsequently increasing defects such as vacancies and adversely affecting EQE. Therefore, Kim *et al.* designed a 3D/2D hybrid perovskite structure that substantially mitigated luminance overshoot while enhancing both stability and efficiency, as presented in Fig. 6c.[17]

Inefficiency. Despite a transient increase in efficiency under electric stress, an excessive EF ultimately leads to decrease in efficiency and stability. The main contributors to this inefficiency are exciton quenching, charge accumulation, and material degradation. First, ion migration within the perovskite layer of PeLEDs serves as a trap site for excitons, initiating nonradiative recombination, and thereby quenching excitons ineffectively. Second, ion migration often triggers charge redistribution within the device, leading to energy band bending, as depicted in Fig. 6d.[107] In addition, ion accumulation can generate an interfacial dipole, altering charge injection and extraction efficiency and consequently reducing device performance. This changes the transport ability of the ETL and HTL, exacerbating the imbalanced carrier injection at high current densities. Further discussion of the material degradation is presented in the subsequent section. In summary, ion migration exerts a significant impact on the efficiency and stability of PeLEDs, necessitating meticulous control and monitoring to optimize performance.

Spectral impurity. Spectral impurities frequently occur in mixed halogen PeLEDs such as $ABBr_xCl_{3-x}$ and ABI_xBr_{3-x}, resulting in deviations from stable pure-blue (460–470 nm)[108] and stable pure-red (630–640 nm) emissions,[109] respectively. Notably, field-driven phenomena contribute to the formation of phase-separated halide-rich domains, thereby inducing spectral impurities. Vashishtha *et al.* presented compelling evidence that varying the Br/I ratio in mixed halide $CsPbBr_{3-x}I_x$ occurs red-shifting and splitting of the EL peaks due to field-driven halide separation.[110] This is highly dependent on NC composition and applied voltage. Under 7 V operation, purified Br and higher I/Br ratio domains were observed, corresponding to green and red peaks as shown in Fig. 6e and f. The instability can often be attributed to the difference in ionic radii: including Cl^-, Br^-, and I^- ions (R_{Cl} = 0.181 nm, R_{Br} = 0.196 nm, and R_I = 0.220 nm),[23] which can introduce defects or lattice distortions that promote ion migration through weak atomic bending. Newly formed Br- or I-domains alter the original energy bandgap, inevitably resulting in peak shifts and spectral broadening. Nevertheless, Li *et al.* demonstrated that although the EL peak experienced a red shift after several minutes of initial electrical operation, this peak offset can be fully reversed if the devices were allowed to rest for an adequate duration.[111] Other research in other dimensional perovskite materials corroborated these findings.[110,112] Due to the limitation of a single test cycle, it remains uncertain how the reversibility of spectral changes impacts the long-term stability

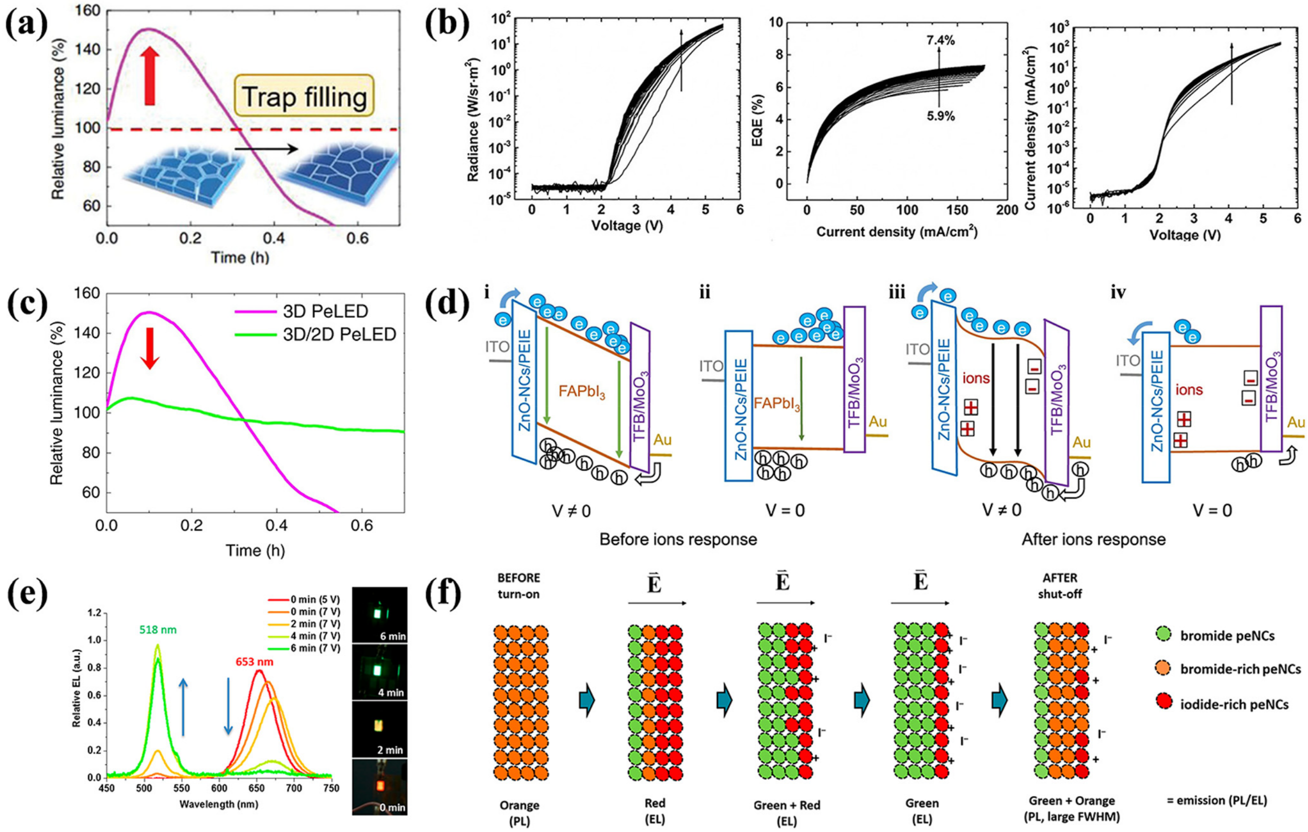

Fig. 6 (a) Impact of the EF-induced ion migration on PeLEDs leading to in luminance overshoot. Reproduced with permission from ref. 82. Copyright 2022 Wiley-VCH. (b) *R*–*V*, EQE–*J*, and *J*–*V* curves of an as-produced PeLED for subsequent voltage scans. Reproduced with permission from ref. 106. Copyright 2017 Wiley-VCH. (c) Relative luminance of 3D/2D hybrid and 3D PeLEDs over time, demonstrating a significant reduction in luminance overshoot for the 3D/2D hybrid PeLEDs. Reproduced with permission from ref. 17. Copyright 2020 Springer Nature. (d) Schematic representation of the band diagram before (left) and after ions responded (right), following the application of a positive forward voltage pulse. Reproduced with permission from ref. 107. Copyright 2021 Springer Nature. (e) EL spectrum from the LED device operating at the turn-on voltage (5 V), at 7 V, and at 2 min intervals until the spectrum had fully shifted, alongside photos of the same LED (right). (f) Schematic diagram of ion separation in (e). (e and f) Reproduced with permission from ref. 110. Copyright 2017 American Chemical Society.

of PeLEDs. In conclusion, mixed LHPs hold promise for future applications in pure red and pure blue light emissions for a wide color gamut. Further detailed investigations into ion migration-induced phase separation and its impact on the spectral purity are warranted.

Degradation. Long-term stability remains a critical challenge impeding the commercialization of PeLEDs.[113,114] Nowadays, the rapid and irreversible degradation of non-encapsulated PeLEDs in ambient conditions during continuous operation is a significant contributor to device instability. Ion migration is the primary cause of degradation. The detrimental effects of ion migration can be categorized into three key degradation areas: perovskite layer, interface, and electrode corrosion. Ion migration induces vacancies and accumulation of halide interstitials at the interface, resulting in a distorted crystal lattice. Deng *et al.* reported a negative feedback loop between perovskite decomposition and ion migration, wherein decomposition accelerated ion accumulation, subsequently decelerating bulk degradation caused by EF.[81] As shown in Fig. 7a, both irreversible and reversible PL responses are observed under varying EF conditions. Moreover, Miao *et al.* further argued that at high operating voltages, surface degradation mediated by ion migration was more pronounced than bulk degradation.[113] As shown in Fig. 7b, at a low driving voltage (2.1 V), both EL and PL exhibited similar decay trends, indicating that the primary degradation mechanism occurred in the perovskite layer.[114] Conversely, although PL remained relatively stable, EL experienced a rapid decline, suggesting that principal degradation occurred at the device interfaces between the EML and the transport layer. These findings are corroborated by additional studies, as indicated in Fig. 7c.[113] Ion migration in specific contexts may exhibit complete or partial reversibility yet evoke complicated electrochemical reactions at interfaces with metal electrodes, significantly impacting PeLEDs' functionality, performance, and durability. Three possible electrochemical reactions in principle: (i) redox reactions localized at the interface, (ii) migration of metal ions from electrodes into the perovskite film, and (iii) corrosion of metal electrodes caused by halide

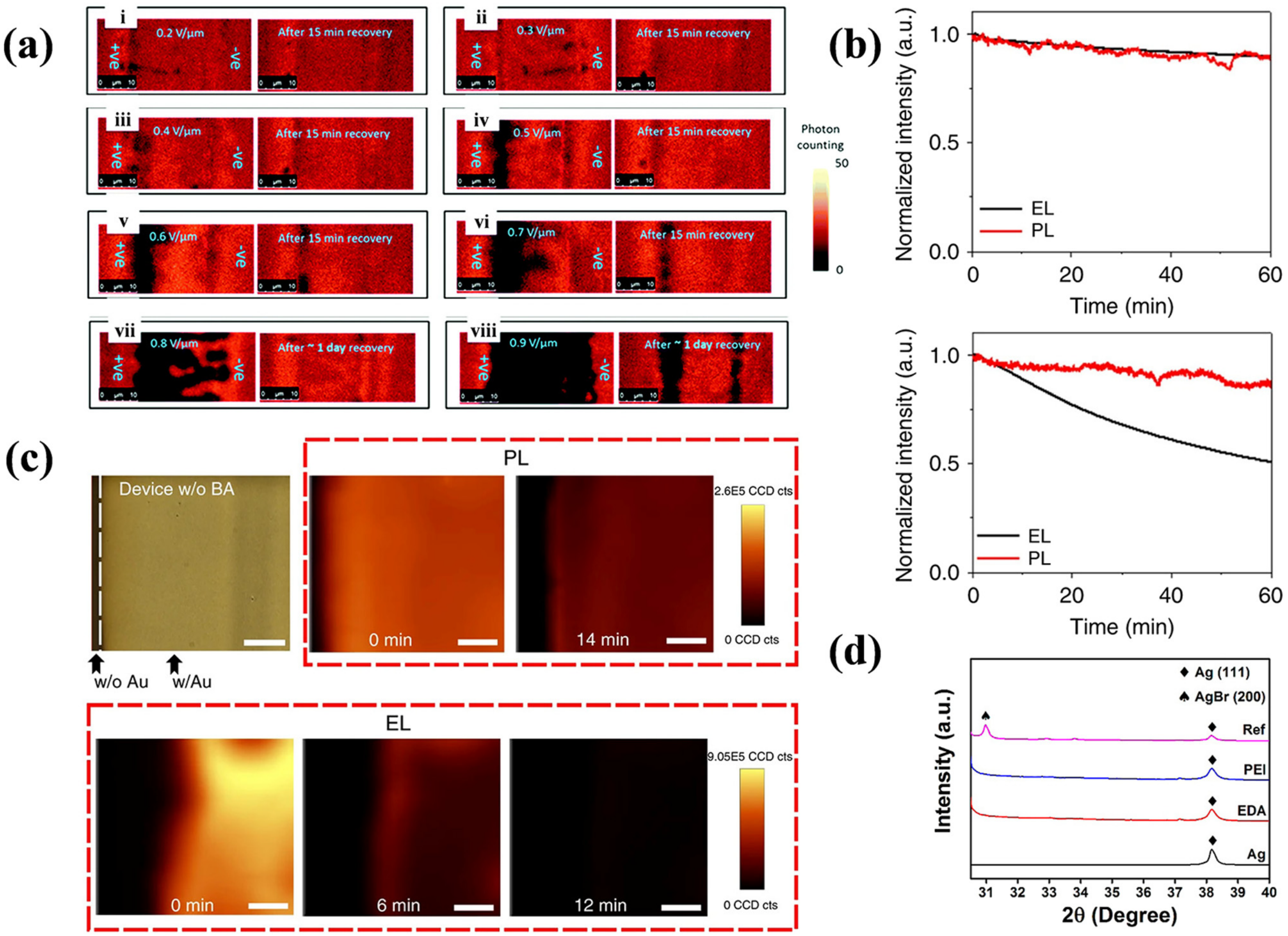

Fig. 7 (a) PL images of the same sample biased as the EF was progressively increased at different electric field levels. Between each biasing, the sample was allowed to recover different minutes. Reproduced with permission from ref. 81. Copyright 2013 Royal Society of Chemistry. (b) Simultaneously measured PL and EL intensities of a working 1.0 DDS film-based LED at a low driving voltage of 2.1 V (top) and high driving voltage of 2.8 V (bottom), respectively. Reproduced with permission from ref. 114. Copyright 2020 Springer Nature. (c) Microscopy image and corresponding PL and EL intensity maps of a device without BA treatment (scale bar, 70 μm), illustrating that degradation initiates from the edge of the Au electrode and the EL degrades faster than the PL. Reproduced with permission from ref. 113. Copyright 2019 Springer Nature. (d) XRD patterns of Ag on $MAPbBr_3$ materials with and without APMs after 30 days. Reproduced with permission from ref. 77. Copyright 2017 American Chemical Society.

complexes. Commonly used metal electrodes, such as Ag, Au, and Al, undergo different electrochemical reactions at the interface due to defect types, with metal ions of higher charge states typically facing greater kinetic barriers. Au is typically recognized for its robust resistance to corrosion and oxidation; nevertheless, the 5d energy level can interact with V_{Pb} to create deep trap states, facilitating the formation of numerous non-radiative complexes.[115] In $MAPbI_3$ PeLEDs, despite a transport layer existing for physical separation, Al^0 in the Al electrode rapidly reduced Pb^{2+} to Pb^0 and converted $CH_3NH_3PbI_3$ to $(CH_3NH_3)_4PbI_6{\cdot}2H_2O$, which is then converted to CH_3NH_3I.[101] Intriguingly, degradation between the Al electrode and the EML proceeded spontaneously, independent of oxygen and light exposure. However, moisture notably enhanced ion diffusion, perpetuating a continuous reaction between the metal and the perovskite, underlining a complex degradation mechanism. Due to the transparency of metal oxide electrodes, like ITO is widely used as the anode, but acidic PEDOT:PSS etches the ITO surface and causes defects, leading to the migration of In and Sn into the EML, generating quenching centers, and causing degradation of the PeLEDs. Light exposure triggers redox reactions between $MAPbI_3$ and Au interface, emitting volatile substances such as I_2 and MAI and leading to polyiodide compounds.[116] These compounds, in turn, can oxidize the gold electrode, forming gold halide complexes, thereby modifying the properties of the interface. Hence, applying contact engineering in perovskite materials is crucial to reduce unwanted interfacial reactions and achieve dependable contact characteristics. To mitigate this, Lee *et al.* employed amine-based passivating materials (APMs) to suppress the corrosion of metal electrodes by inhibiting ion migration from the perovskite layer to the electrode, thus enhancing both efficiency and stability of PeLEDs.[77] Fig. 7d reveals that the XRD pattern of Ag on $MAPbI_3$ without APMs

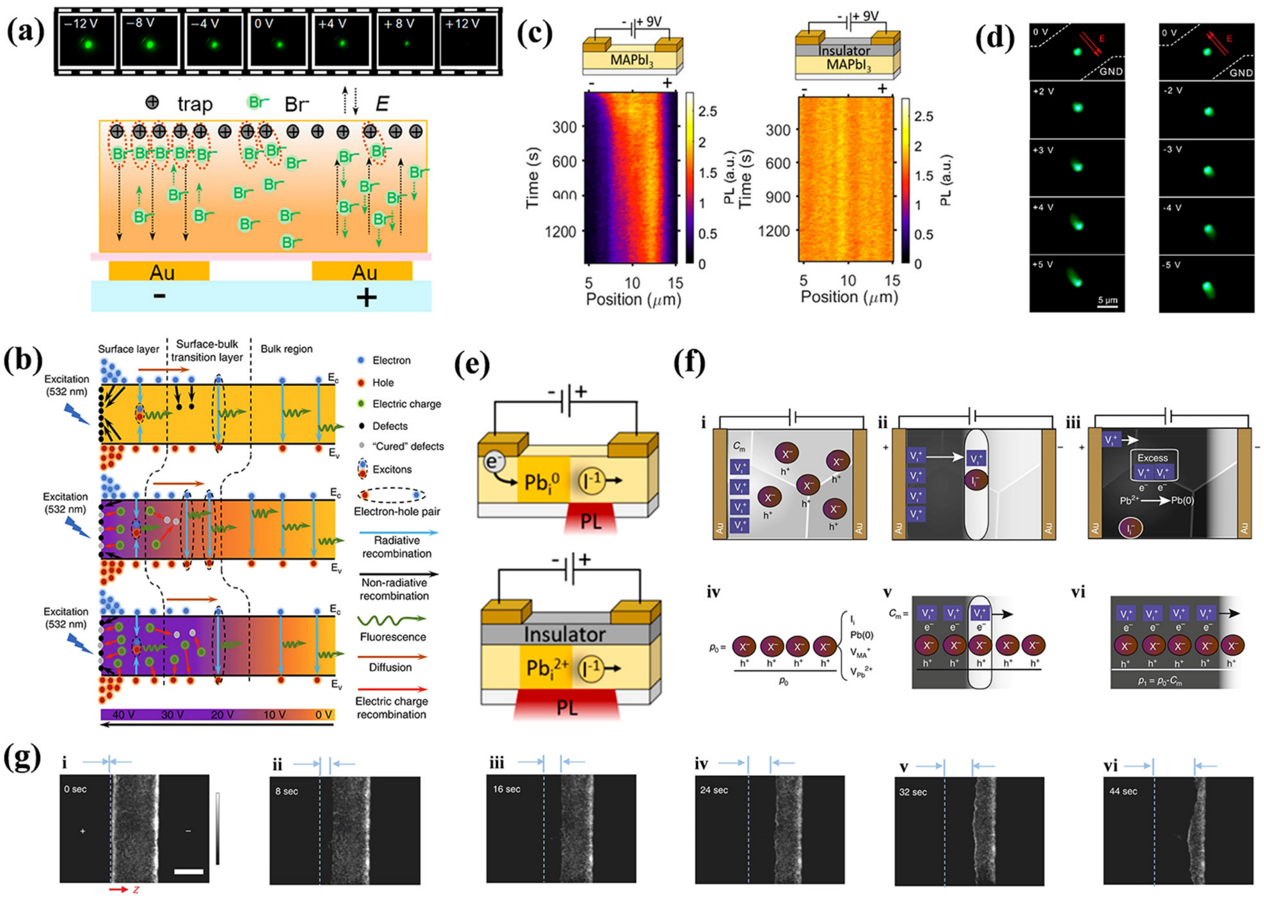

Fig. 8 (a) PL images of the MIS structure with voltages varying from −12 V to +12 V (top); schematic illustration of the electric-field-induced interaction between Br vacancies and excessive Br^- (bottom). Reproduced with permission from ref. 3. Copyright 2021 American Chemical Society. (b) Schematic diagram of the three-step carrier transfer model for MPB SCBK with 532 nm excitation under no bias, appropriate bias, and excessive bias. Reproduced with permission from ref. 122. Copyright 2020 Springer Nature. (c) PL scan of a single line within the electrode gap for $MAPbI_3$/Au (left) and $MAPbI_3$/PMMA/SiO_2/Au (right) during a bias of +9 V applied to the right electrode. Reproduced with permission from ref. 21. Copyright 2018 American Chemical Society. (d) Real-color PL images of a typical $CsPbBr_3$ nanoplate device with different positive (left panel) and negative (right panel) bias voltages applied at the upper electrode. Reproduced with permission from ref. 124. Copyright 2018 American Chemical Society. (e) Schematic illustration of the redox processes of Pb_i^{2+} in different $MAPbI_3$ device structures. Reproduced with permission from ref. 21. Copyright 2018 American Chemical Society. (f) Interpretation of the dominant ionic effects. Diagrams proposing processes occurring during the application of an electrical field in the lateral electrode configuration. (g) Time-dependent PL images of a perovskite film $CH_3NH_3PbI_{3-x}Cl_x$ under an external EF (~2×10^4 V m^{-1}). The "+" and "−" signs indicate the polarity of the electrodes. (f and g) Reproduced with permission from ref. 118. Copyright 2018 Springer Nature.

demonstrates an evident signal of AgBr, implying severe electrode corrosion due to ion migration.

3.2 PL variation

Current research has predominantly employed lateral EFs to modulate the PL of the perovskite layer for defect behavior analysis. Gao groups pointed out that an EF can induce either passivation or activation of V_{Br} depending on the direction of the laterally applied field. As depicted in Fig. 8a, V_{Br} commonly locates at the surface of $CsPbBr_3$ microplates as a positive center for capturing photogenerated electron.[3] In a negatively biased EF, these vacancies are passivated by excess Br^- ions from raw material, resulting in increased PL brightness with escalating negative bias. In contrast, the V_{Br} and Br^- ions move in opposite directions, causing a reduction in the PL intensity. Awasthi *et al.* reported lateral field-induced PL variations due to changes in the number of free carriers.[117] They observed that the trapping probability of electrons by defects varied for different field orientations. A positive field declines the number of free carriers and trapped electrons, reducing the nonradiative recombination and increasing the lifetime. In contrast, a negative EF exhibited the opposite effect. This reflects the anisotropic impact of EF on the PL of the $MAPbI_3$ perovskites. However, most related studies have not concentrated on the defect behaviors and their interactions with carriers that lead to PL alterations. Moreover, as displayed in Fig. 7a, Deng *et al.* used PL in a lateral EF setting to study the degradation of perovskite materials, an experiment similar to the one described above. They discovered that ion migration and defect-mediated accumulation lead to reversible PL changes. This findings is consistent with earlier work indicating that MA- and I-related defects migrate in a lateral EF, causing PL quenching, as shown by PL imaging microscopy.[118] The mobility of MA- and I-associated defects prompts a shift in the effective concentration of electron–hole pairs, resulting in numerous sites for nonradiative quenching. This subject has been rigorously investigated in the context of PSCs.[119–121]

In the context of an applied EF, in addition to the response of charged defects, there is an additional case of carrier injection, which complicates the interaction process between the defects and carriers. Xing *et al.* delineated a universal three-step carrier transfer model, as illustrated in Fig. 8b.[122] Owing to the commonly used preparation methods, numerous defects are generated both on the surface and within the bulk of the film. The three steps predominantly occur at the surface, surface–bulk transition layer, and bulk region of the material. In the absence of an EF, the photogenerated electrons and holes initially interact with the surface defects upon laser excitation. Subsequently, the remaining electrons and holes drift into the surface–bulk transition layer, where some are captured by the bulk defects. Upon diffusion into the bulk region, these carriers transition into free carriers, leading to a long-lifetime radiative recombination. The introduction of an appropriate EF increases the complexity by inducing both photogenerated and electrically injected carriers. Under the influence of EF, bulk defects gravitate toward the surface, while these surface defects capture some of the injected carriers, resulting in passivation. Furthermore, bulk defects can be healed by drifting photogenerated or injected carriers, thereby neutralizing the treated defects and increasing radiative recombination at the surface and surface–bulk layers. Moreover, excessive voltage introduces additional charge carriers that can mitigate pre-existing defects and generate new ones by capturing holes, thereby reducing the probability of radiative recombination. Hence, numerous studies have corroborated the potential for voltage regulation engineering to passivate surface defects and mitigate carrier-related issues.[3,123]

It is vital to understand the impact of the behaviors between injected carriers and defect on recombination mechanisms. Birkhold *et al.* studied PL quenching in $MAPbI_3$ using lateral devices equipped with both charge-injecting and insulator-coated blocking contacts.[21] They witnessed PL quenching exclusively at injecting contacts when bias was introduced, whereas the $MAPbI_3$ film displayed no defect-assisted charged ion migration without charge injection, as illuminated in Fig. 8c. Hu *et al.* showed that charged carrier transport is a vital process in defining the performance of $CsPbBr_3$ nanoplates under an EF. Fig. 8d shows that when a lateral positive bias is applied, the emission spot adopts an elongated shape directed towards the top electrode, counter to the applied EF.[124] The degree of elongation is directly proportional to the applied bias magnitude. Notably, under a negative bias, the emission spot extends towards the opposite electrode, always in a direction opposite to the applied EF. This elongation of the PL tail is attributable to the drift of photogenerated minority carriers under the applied bias. Importantly, the PL images exhibits less pronounced elongation at low temperatures, further substantiating the nuanced role of injected carriers in the presence of an EF.

Investigating the effects of vertical EF on defect behaviors is complicated because of the absence of more intuitive characteristics. Leijtens *et al.* fabricated $MAPbI_{3-x}Cl_x$ capacitors using non-injecting Al_2O_3 contacts to examine the dynamics of defect-induced excited states at room temperature (RT) and 190 K, employing both PL and TrPL analyses to eliminate the effect of injected carriers.[20] The field-induced PL was attenuated at RT, with distinct trends observed for the single- and double-molecular decays of PL. This attenuation arose from photoexcited carriers and charged defects drifting in opposite directions under EF, reducing the probability of radiative recombination while accumulating charged defects at the non-injecting interface. Conversely, at 190 K, the enhancement in the field-induced PL persisted even after the field was deactivated. This enhancement was attributed to the EF-induced alignment of organic cations at low temperatures, which limits the vibrational freedom and local shielding of the lattice between the organic and inorganic ions. This leads to stronger electron–hole interactions, accompanied by slower rates of charge drift, charged ion migration, and carrier capture at these low temperatures. Hence, the rate of radiative recombination surpassed that of nonradiative recombination. Under the influence of EF, PL quenching occurred in conjunction with carrier separation and drift, leading to a reduction in the nonradiative relaxation rate. This observation indicates that mobile defects under EF also have a significant impact on the rate of nonradiative recombination.

To realize efficient and stable PeLEDs, a comprehensive understanding of the defect behavior and carrier interactions in halide perovskite materials under operational conditions is imperative. Such an analysis will provide valuable scientific insights and theoretical frameworks essential for enhancing the fundamental properties of these materials, thereby addressing the challenges previously outlined.

3.3 Induced new defects

When EF is applied to a device, defects are the first to respond to. However, the motion of one defect under the influence of EF can induce the formation of additional new defects, thereby altering the energy band structure. This process can result in vacancy–interstitial pairs, which complicates the differentiation between intrinsic and field-induced defects. Although the transformation of semiconductor electrical morphology induced by ions remains an area for further investigation, the mechanisms governing the generation of new defects in PeLEDs under EF is also a subject of active research. Theoretical and experimental studies have been conducted to propose various models to elucidate these phenomena.

The proposed mechanism suggests that EF can promote the migration of various defect types, such as point defects, vacancies, and interstitials, leading to the formation of new defects, as discussed in Section 3.1. This defect migration can subsequently generate charge carriers and their recombination, leading to light emission. In standard device configurations, these defects often interact with the injected carriers. Birkhold *et al.* reported that injected electrons can interact with existing defects to form new nonradiative defect centers, specifically Pb_i^0, through the electrochemical reduction of Pb_i^{2+}.[21] A diagram of the redox process is shown in Fig. 8e. DFT calculations indicate that Pb_i^{2+} resides above the CBM with a defect energy level of 0.08 eV, whereas Pb_i^0 forms a deep trap state at 0.47 eV below the CBM, corroborating observed PL bursts in Fig. 8c. However, such phenomena are absent in devices without electron injection. Bisquert *et al.* extended this understanding by exploring the role of interstitial Pb(0),[118] and employed p-type doped $MAPbI_3$ with defect types including I_i, V_{MA}, V_{Pb}, and lattice Pb(0) for their investigation. Among the inherent defects studied, only I_i can form deep energy levels while being neutralized by V_I, thus mitigating the quenching centers. Furthermore, excess V_I can trigger redox reactions that convert the interstitial Pb^{2+} to Pb(0), as illustrated in Fig. 8f. Both I_i and Pb(0) serve as nonradiative recombination centers that quench the PL images, as shown in Fig. 8g. Huang *et al.* also reported that ferroelectric polarization in perovskite polycrystalline films could induce grain polarization and ion migration, creating new defects when the polarization strength surpasses 1.0 V μm^{-1}.[84] Using Br/Cl mixed-halide NCs as a research object, Liao *et al.* investigated the defect behavior in PeLEDs with varying numbers of layers of NCs under EF.[125] They pointed out that multilayered NC devices, which undergo drift of Cl^- between adjoining NCs under the action of the EF, induce a new defect region with Cl-deficient, which leads to spectral instability and degradation of the device. In contrast, devices with single-layered NCs can efficiently curb the process. However, the excess holes injected, coupled with the electrochemical reaction react with Cl^-, lead to the generation of irreversible chlorine vacancy regions. Such defects constitute deep traps and nonradiative recombination centers.

An alternative mechanism imply that EF can induce the formation of new defects through electrostriction or piezoelectric effects. In this scenario, EF causes strain within the perovskite material, resulting in new defect formation and the consequent modulation of the electronic structure of the material. Supporting this notion, Wieghold *et al.* utilized SMA-STM to study the bandgap of $Cs_{0.05}(FA_{0.83}MA_{0.17})_{0.95}Pb(I_{0.83}Br_{0.17})_3$.[18] Their findings revealed a marginal reduction in the bandgap with increasing EF strength, with an even greater reduction observed under illumination. This behavior can be attributed to charged defects, which alter the crystal structure and in turn influence electron–phonon coupling, subsequently affecting the carrier recombination dynamics. DFT calculations further corroborate these observations, confirming changes in lattice constants, bandgap, and optical absorption characteristics with enhanced EFs.

Overall, the behavior of defects in PeLEDs under EF presents a complex and not yet fully understood landscape at the microscopic level. Currently, the majority of research in this area is focused on ion migration, with considerable efforts directed towards the development of passivation techniques to mitigate this phenomenon. Despite these efforts, advancements in microscale analysis of defect behavior have been relatively slow. Many studies have employed changes in the PL in the presence of a lateral EF to investigate the interactions between defects and both photogenerated and injected carriers. The application of an external EF in PeLEDs can lead to the segregation and translation of photogenerated carriers, affect the inherent defect migration, and generate new defects that alter the density of states, ultimately affecting both radiative and nonradiative recombination mechanisms. However, the situation under vertical field conditions remains relatively unexplored. Hence, a comprehensive understanding of carrier recombination dynamics, defect migration, and charge capture under EF modulation is pivotal for improving the performance of PeLEDs and accelerating their path to commercialization.

4. Management of defects

To overcome the hindrance caused by defects that adversely affect device performance under EF conditions, researchers worldwide are exploring a range of passivation strategies. Various similar but not identical procedures, such as ligand engineering, additive incorporation into precursor solutions, and inclusion of interfacial layers within devices, have been used to develop perovskite defect passivation. Considering high surface-area-to-volume ratio NCs, ligands can control nucleus growth and size regulation during synthesis, while post-treatment with ligands can fine-tune the surface chemistry of NCs, both allowing for comprehensive defect passivation from the inside out at the same time. Yet, incorporating a controlled ratio of additives into precursor solutions not only promotes the growth of high-quality crystalline films with fewer defects, but also elevates the PLQY and overall device efficiency. Importantly, device engineering remains crucial to unlock the full potential of near-perfect LHPs in achieving high-performance PeLEDs. The strategic insertion of compatible interfacial layers can further passivate defects in perovskite films and minimize the grain boundary issues. Therefore, this chapter provides a comprehensive overview of the latest advancements in each of these key areas.

4.1 Defects passivation strategies in LHP NCs

4.1.1 Surface chemistry in LHP NCs. Since the pioneering discovery of nanoscale $MAPbBr_3$ particles by Schmidt *et al.*, the surface chemistry of LHP NCs has been a subject of rigorous study.[126] Surface chemistry is fundamental to understanding how to control the nucleation, growth, stability, and conductivity of NCs. As illustrated in eqn (14), which outlines the hot injection (HI) synthesis of $CsPbX_3$, the indispensable role of ligands in the preparation process becomes evident. The common use of ligands such as long-chain oleic acid (OA) and oleylamine (OLA) is particularly noteworthy. These ligands serve as stabilizing agents and provide essential passivation features *via* their amine-acid pairs during the synthesis of LHP NCs. The molecular formula reveals that the amino and carboxylic functional groups from long-chain, 18-carbon OLA and OA are instrumental in effectively controlling the morphology and providing protection against oxygen and moisture attacks. Among these, the interaction between OA and OLA with NCs' surface sites has garnered some debate. During NC synthesis, OA donates a proton to OLA, resulting in the formation of an ammonium cation (R-NH_3^+). This occurs when OA and OLA are present at a 1 : 1 molar ratio in a nonpolar solvent, as shown in eqn (15). The amino group of OLA can engage in coordinate bonding with unsaturated Pb^{2+} ions on the surface, utilizing its lone pair of electrons while in an unprotonated state.[126] In contrast, computational studies suggest that R-NH_3^+ could occupy up to 50% of A-site cations on the surface in theory.[127] Moreover, a portion of R-NH_3^+ passivates V_{Br} *via* hydrogen bonding, irrespective of the surface termination.[128] The formation of ammonium carboxylate salts, as outlined in eqn (15), increases the dissolution of $PbBr_2$, subsequently enhancing the production of Br^- ions according to eqn (16). It is widely accepted that OLA forms robust bonds with NC surfaces. However, there is a debate regarding the role of OA in the surface bonding. Angshuman Nag *et al.* employed nuclear Overhauser effect spectroscopy (NOESY) to investigate whether OA exists as free ligands in the final colloidal dispersion, thus not binding to the NC surface.[128] In post-purification solution, the addition of excess OLA enables OA to form alkylammonium oleate through ion pairs with amines, facilitating its enhanced surface adsorption,[129] as illustrated in eqn (17). Brutchey *et al.* utilized ^1H NMR and diffusion-ordered spectroscopy (DOSY) to suggest that both OA and OLA interact with the surface of NCs.[130] In addition, their work contradicts the findings of De Roo *et al.*, asserting that OA binds securely to the NC surface even without excess amines. Additional studies indicate that the R-COO^- can coordinate with unsaturated Pb^{2+} and A-site cations through electron donation.[56,126] Concurrently, long-chain OA may passivate surface X^- to coordinate with Pb^{2+}, thereby stabilizing the octahedral structure.[131] In summary, it is generally acknowledged that due to the ionic nature of perovskite NCs, the formation of labile bonds between OLA/OA ligands and NC surfaces is inevitable.

$$2\text{Cs-oleate} + 3PbX_2 = 2CsPbX_3\ \text{NCs} + Pb(\text{oleate})_2 \tag{14}$$

$$RNH_2 + RCOOH \rightleftharpoons NH_3^+ ... COO^- \tag{15}$$

$$\begin{aligned} &2PbBr_2 + NH_3^+ \ldots COO^- + xRNH_2 \\ &\rightarrow PbBr_3^- \cdot NH_3^+ + PbBr^- \cdot COO^- + xRNH_2 \end{aligned} \tag{16}$$

$$NH_3^+ ... COO^- + RNH_2 \rightleftharpoons (NH_3^+ ... RNH_2)COO^- \tag{17}$$

The intricacy of surface chemistry of perovskite NCs is partly attributable to the interactions between various surface terminations and capping ligands. Bodnarchuk *et al.* proposed a likely model for the NC surface structure and discussed strategies for healing trap states on these surfaces, a key determinant of colloidal stability.[132] Fig. 9a delineates three potential

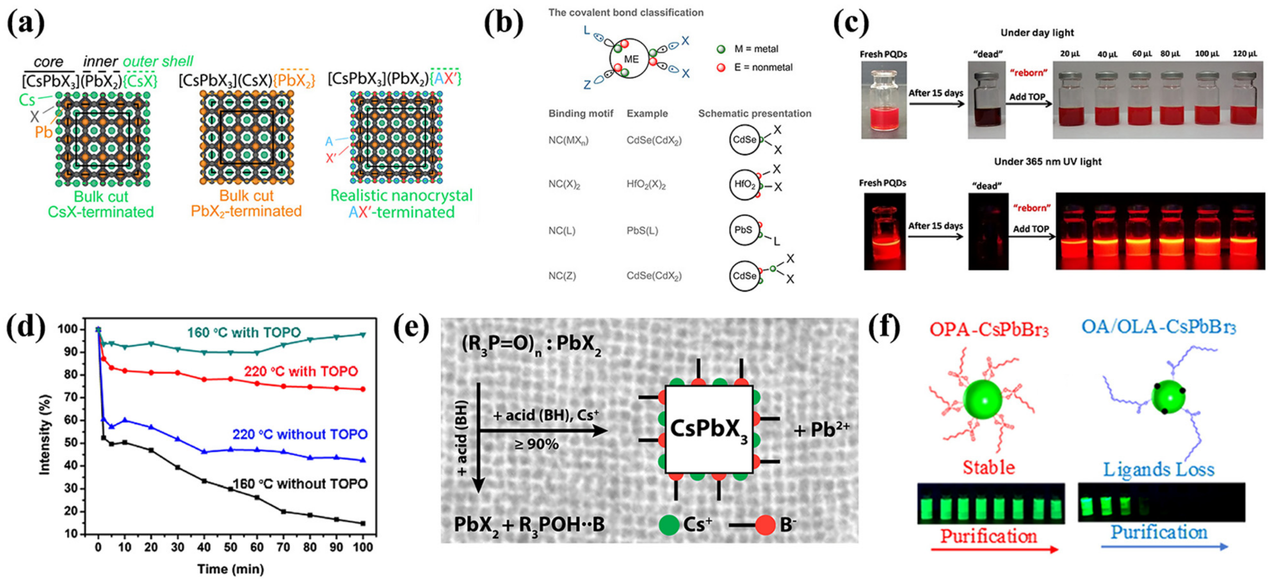

Fig. 9 (a) The NC is arbitrarily divided into core, inner, and outer shell in three different ways. Reproduced with permission from ref. 132. Copyright 2019 American Chemical Society. (b) Schematic representation of the most important ligand classes within the covalent bond classification scheme. Reproduced with permission from ref. 129. Copyright 2016 American Chemical Society. (c) Photos of fresh/aged PNCs and aged PNCs with different amounts of TOP under daylight (top) and UV light (bottom). Reproduced with permission from ref. 135. Copyright 2018 American Chemical Society. (d) Intensity of PL emission as a function of $CsPbBr_3$ NCs against ethanol treatment time. Reproduced with permission from ref. 143. Copyright 2017 American Chemical Society. (e) A schematic of how TOPO, $PbBr_2$, acid, and Cs^+ interact within the NCs synthetic system. Reproduced with permission from ref. 145. Copyright 2018 American Chemical Society. (f) Synthesis of $CsPbBr_3$ NCs with OPA (left) and OA/OLA (right), schematic representation of the NC surface chemistry (top), and physical representation of the change in luminescence (365 nm excitation) after multiple purifications (bottom). Reproduced with permission from ref. 150. Copyright 2018 American Chemical Society.

surface terminations: $[CsPbX_3](PbX_2)\{CsX\}$, $[CsPbX_3](CsX)\{PbX_2\}$, and $[CsPbX_3](PbX_2)\{AX'\}$. Here, [ ] donates the core, ( ) represents the inner shell, and { } represents the outer shell, where A represents alkylammonium and Cs^+, and X′ respond to halides and/or oleates. Among these, the $\{PbX_2\}$-terminated model is highly improbable because of the necessity for a 2.5 times greater ligand packing density, resulting in steric hindrance and disruption of the octahedral coordination tendency of Pb^{2+}. The most experimentally congruent model was $[CsPbX_3](PbX_2)\{AX'\}$. Therefore, to achieve high-performance electrical and photophysical semiconductor properties directly influenced by the surface characteristics, it is essential to reconstruct the damaged (PbX_2) surface and fortify the $\{AX'\}$ outer layer to maintain the stability of the $[PbX_6]^{4-}$ octahedra.

In summary, a thorough understanding of electro-optical performance of defect states and the surface chemistry of NCs is vital for achieving high-quality and stable LHP NCs. Existing challenges persist in the equilibrium between surface passivation and charge transport when traditional OA and OLA ligands are used. Recently, there has been an increase in research on novel ligands that not only bind more securely to the NC surface, but also exhibit outstanding transmission characteristics. Therefore, the subsequent section focuses on enhancing LHP NC passivation through ligand optimization. Further details can be found in Table 2.

4.1.2 Surface passivation *via* ligand control. Ligand engineering has emerged as an effective approach for achieving both high environmental stability and EQE in PeLEDs to address the dynamic binding of long-chain OA/OLA to NC surfaces and the negative carrier transport. Kovalenko and co-workers have proposed a covalent bonding classification method for ligands, designating them as L-, X-, and Z-type ligands, as illustrated in Fig. 9b.[129] L-type ligands, typically referred to as Lewis bases, donate lone electron pairs to empty orbitals on the NC surface.[133,134] In contrast, Z-type ligands usually Lewis acids, possess electron-acceptor groups. X-type ligands own metal–ligand bond, with each electron coming from the ligand and the nanocrystalline surface, and generally include ammonium salts, radicals, or zwitterionic molecules.[126] In acid–base electron theory, the classification of a substance as either acidic or basic should be based on its behavior in specific reactions, rather than a general assessment of its acidic or basic nature. The same substance can act as an acid or a base in different reaction environments.

L-type ligands

Phosphine and phosphine acid. Phosphorus-containing materials interacting with the PNC particles during NC synthesis subsequently affect the colloidal stability of PNCs, with the effects varying based on the functional groups and carbon chain lengths attached to the phosphorus atom. Trioctylphosphine (TOP) has been successfully used to regenerate non-luminous aged $CsPbBr_{1.2}I_{1.8}$ NCs without detectable structural changes, as depicted in Fig. 9c,[135] and to enhance the optical performance of fresh $CsPbI_3$ NCs. Contrary to the prevalent view that TOP does not directly interact with the surface after treatment confirmed by X-ray Photoelectron Spectroscopy (XPS) and Fourier transform infrared spectroscopy (FTIR).[135,136] TOP facilitates the release of $R\text{-}COO^-$ groups from their coordination with Pb^{2+} owing to the Lewis base effect, which is a critical factor in mitigating the degradation of $\alpha\text{-}CsPbI_3$ by further promoting chemical equilibrium.[136] This mechanism results in effective surface passivation. However, Geyer *et al.* found that adding TOP to post-treatment $CsPbI_3$ NCs considerably enhanced the phase stability of the solution.[137] FTIR and XPS mapping data indicate that TOP acts as a capping ligand to protect NCs, albeit with a weak P peak, suggesting a limited quantity of P consistent with the fact that each TOP only has one P atom. This diverges from the conclusions of Zhang *et al.* Moreover, TOP serves as a coordinating alkylphosphine solvent to improve the reactivity of the PbI_2 precursor forming $TOP\cdot PbI_2$ compound, thus accelerating nucleation and growth to yield high-quality $CsPbI_3$ NCs.[138] TOP is frequently used as an alternative to alkylammonium to improve the optical properties of LHP NCs in amine-free conditions. Xu *et al.* incorporated both TOP and lead stearate ($Pb(St)_2$) in their synthesis approach to create an environment devoid of amines and acids.[139] The dual carboxyl groups of $Pb(St)_2$ were strategically utilized for robust surface passivation. One carboxylate facilitated the conversion of TOP to TOPO, whereas the other interacted with a Br^- dangling bond, resulting in a Pb-rich surface with carboxylate-based passivation. In addition to TOP, phosphine-containing compounds such as triphenylphosphine (TPP),[140,141] diphenylphosphine (DPP),[142] and tributylphosphine, have also been widely explored, each showing varying degrees of enhancement in the performance of NCs.

Subsequent research has revealed the efficacy of the P═O functional group in improving both the crystallinity of NCs and efficiency of PeLEDs. The first ligand featuring a P═O group applied to the perovskite NC system was trioctylphosphine oxide (TOPO), which was a branched capping ligand, conferring strong steric stability at high temperatures. Zhang *et al.* mixed TOPO and OA/OLA to synthesize TOPO-capped $CsPbX_3$ NCs using a hot-injection method.[143] In FTIR, the peak at 1155 cm^{-1} is attributed to C–P stretching, confirming that TOPO is anchored to the surface. TOPO increased the thermal stability threshold for obtaining monodisperse NCs to 260 °C and demonstrated exceptional resistance to degradation by protonic solvents, such as ethanol, as displayed in Fig. 9d. Kim *et al.* fabricated a PeLED structure (ITO/PEDOT:PSS/VB-FNPD/NCs/TPBi/LiF/Al) treated with a Zn-TOPO complex,[144] achieving high EQE (7.12%, 6.06%, and 0.56%) and CE (9.93 cd A^{-1}, 32.5 cd A^{-1}, and 0.88 cd A^{-1}) for red, green, and blue devices. TOPO possessing L-type ligand properties, readily forms complexes with Zn^{2+} from excess ZnX_2 raw material, offering Zn-TOPO the properties of a Lewis acid to passivate halide defects. ^{31}P NMR and XPS revealed that TOPO adheres to the surface of NCs only when coordinated with Zn^{2+}, generating a reduction in Pb–O lattice bonding. Interestingly, when TOPO fully replaced OLA in a formulation that also included OA, it was largely absent from the ligand shell, which was exclusively passivated by Cs-oleate, a finding corroborated by Manna *et al.* in 2018.[145] Solvent acidity and the degree of TOPO protonation were found to influence both the reactivity of the PbX_2 precursor and the size distri-

Table 2 Summarized ligands binding to LHP materials and devices

Perovskite	Ligands	Structure	Type (L, X, Z)	Classification	Ligands treatment methods	Material PLQY^a/ PLQY^b (%)	EQE^c/EQE^d (%)	Ref.
$CsPbI_3$	Trioctylphosphine (TOP)	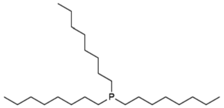	L	Phosphine acid	Post-treatment	66/83	—/—	135
$CsPbBr_3$	Trioctylphosphine oxide (TOPO)	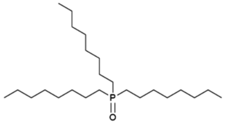	L	Phosphine acid	Used as synthetic ligands	50/>80	—/6.06%	143
$CsPbBr_3$	Octylphosphonic acid (OPA)	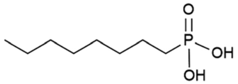	L	Phosphine acid	Used as synthetic ligands	>80/>90	0.86/6.5	149
$CsPbI_3$	Ammonium thiocyanate (NH_4SCN)	$N{\equiv}S^{-}\ NH_4^{+}$	X	Thiocyanate	Used as synthetic ligands	65/89	6.6/10.3	153
$CsPbBr_3$	Sodium thiocyanate (NaSCN)	$N{\equiv}S^{-}\ Na^{+}$	X	Thiocyanate	Post-treatment	92/99	—/—	154
$CsPbBrxCl_{3-x}$	Potassium thiocyanate (KSCN)	$N{\equiv}S^{-}\ K^{+}$	X	Thiocyanate	Post-treatment	34/74.1	0.6/2.04	156
$CsPbBr_3$	Dodecanethiol (DDT)	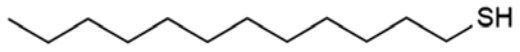	X	Thiocyanate	Post-treatment	54/90–99	—/—	164
$CsPbI_3$	1-Octanethiol (OT)	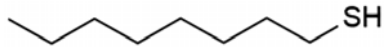	X	Thiols	Post-treatment	76/88	—/—	168
$CsPbI_3$	1-Octadecanethiol (ODT)	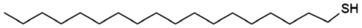	X	Thiols	Post-treatment	52/93	—/—	171
$CsPbBr_3$	Dodecylbenzene sulfonic acid (DBSA)	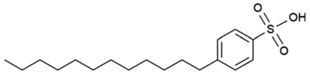	X	Sulfonic acid	Used as synthetic ligands	—/>90	—/—	175
$CsPbI_3$	Sodium dodecyl benzene sulfonate (SDSA)	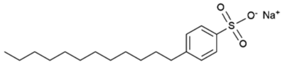	X	Sulfonic acid	Used as synthetic ligands	42.2/90.7	—/—	176
$CsPbBr_xCl_{3-x}$	Tetrabutylammonium *p*-toluenesulfonate (TBSA)	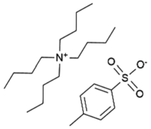	X	Sulfonic acid	Post-treatment	7/29	—/2.6	177
$FAPbBr_3$	2-Naphthalenesulfonic acid (NSA)	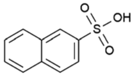	X	Sulfonic acid	Post-treatment	46/93	<15/19.2	178
$CsPbBr_3$	3-(*N*,*N*-Dimethyloctadecylammonio) propanesulfonate (SBE-18)	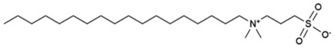	X	Zwitterionic ligands	Used as synthetic ligands	>70/>90	—/2.5	181
$CsPbBr_3$	ZW–PIMA–PEG	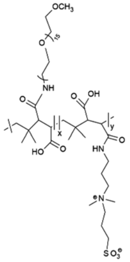	X	Zwitterionic ligands	Post-treatment	55–60/70–80	—/—	185

Table 2 *(Contd.)*

Perovskite	Ligands	Structure	Type (L, X, Z)	Classification	Ligands treatment methods	Material PLQY[a]/PLQY[b] (%)	EQE[c]/EQE[d] (%)	Ref.
$CsPbI_3$	Lecithin	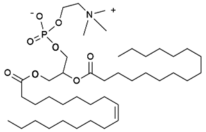	X	Zwitterionic ligands	Used as synthetic ligands	60/100	1.2/7.1	190
$MAPbI_2Br$	Ethylenediaminetetraacetic acid (EDTA)	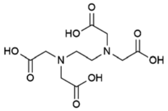	X	Zwitterionic ligands	Post-treatment	>50/>65	4.13/20.28	192
$MAPbBr_3$	L-Cysteine	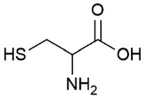	X	Zwitterionic ligands	Used as synthetic ligands	—/53.7	—/—	194
$MAPbBr_3$	Succinic acid	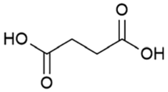	X	Zwitterionic ligands	Used as synthetic ligands	—/34	—/—	195
$CsPbI_3$	2,2′-Iminodibenzoic acid (IDA)	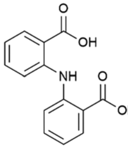	X	Zwitterionic ligands	Post-treatment	80 ± 5/95 ± 2	2.26/5.02	196
$CsPbBr_3$	Oleylammonium iodide (OMA-I)	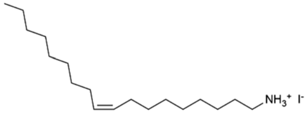	X	Ammonium salts	Post-treatment	38/80	0.17/21.3	197
$CsPbBr_3$	Aniline hydroiodide (An-HI)	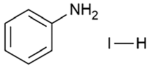	X	Ammonium salts	Post-treatment	38/69	0.17/14.1	197
$CsPbBr_3$	Di-dodecyl dimethyl ammonium bromide (DDAB)	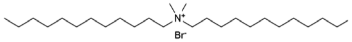	X	Ammonium salts	Post-treatment	49/71	0.1/3.0	198
$CsPbI_{3x}Br_x$	Potassium oleate (K-OA)	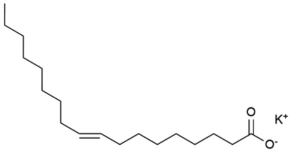	Z	Alkali metal salts	Used as synthetic ligands	85/93	1.89/3.55	110
$CsPbI_3$	Potassium iodide (KI)	$K^+ I^-$	Z	Alkali metal salts	Post-treatment	75/96	16/23	200

[a] PLQY of the material before binding the new ligand. [b] PLQY of the material after binding the new ligand. [c] EQE of the device before binding the new ligand. [d] EQE of the device after binding the new ligand.

bution of the NCs, as shown in Fig. 9e. In addition to TOPO, ligands featuring P═O groups, such as triphenylphosphine oxide (TPPO)[146,147] and tris(4-fluorophenyl)phosphine oxide (TFPPO),[148] have also been used to effectively passivate reduced-dimensional perovskites.

Alkylphosphonic acids, known for their dual chelating sites, offer robust affinities to NC surfaces and are frequently utilized as alternatives to OA and OLA.[149] For instance, octylphosphonic acid (OPA) promotes the dissolution of precursors without requiring amines, due to its acid-dissociation properties. Moreover, OPA's dual chelation sites formed close associations with Pb^{2+}, accelerating both nucleation and growth processes.[150] This leads to the formation of highly stable NCs that are resistant to antisolvents, as illustrated in Fig. 9f. These characteristics have contributed to advancements in device fabrication. Compared with OA/OLA, OPA has shorter carbon chains (8C), which facilitates the removal of detrimental organic ligand residues from OPA–$CsPbBr_3$, yielding highly planar films and devices with an EQE of 6.5%. Additionally, bis(2,2,4-trimethylpentyl)phosphinic acid (TMPPA) serves as an excellent alternative to OA in synthesizing $CsPbI_3$, producing high-quality NCs that resist transitioning to the δ-$CsPbI_3$ phase.[151]

X-type ligands

Thiocyanate. Thiocyanates, considered pseudohalides, offer superior stability over halides and present a promising alternative for perovskite anions, thereby opening new avenues for the tailored design of optoelectronic properties in hybrid inorganic/organic perovskite materials.[152] In contrast to the spherical geometry of X^-, the SCN^- feature a rod-shaped structure, allowing the lone pairs of electrons from both S and N atoms to engage in robust chemical interactions with NC surfaces.[153] Previous research has noted the similarities in ionic radii and electronegativity between SCN^- (217 pm) and I^- (220 pm).[152] Hence, it has been shown that the introduction of ammonium thiocyanate (NH_4SCN) in the synthesis of $CsPbI_3$ NCs can improve crystal quality without lattice incorporation, while reducing surface defects and grain boundaries.[154] Specifically, the dangling Pb^{2+} bonds interact with SCN^- to form Pb–S bonds, thus decreasing surface defects and the CBM of $CsPbI_3$. This results in an improved electron injection efficiency and an increase in the EQE from 6.6% to 10.3%.

In earlier studies, the role of SCN^- was shown to be significant in Br-based NCs. Alivisatos *et al.* reported that post-synthetic treatment of $CsPbBr_3$ NCs with either NH_4SCN or NaSCN powders effectively renovated the lead-rich surface, mitigating shallow electron traps without altering the shape or crystalline structure of the NCs.[155] FTIR analyses pointed that Na^+ or NH_4^+ ions engaged with oleate species, while SCN^- ions interacted specifically with Pb^{2+}. Although SCN^- occupied only 10–15% of the surface sites, it ensured a monoexponential decay profile (Fig. 10a), nearly unity PLQY, and improved the

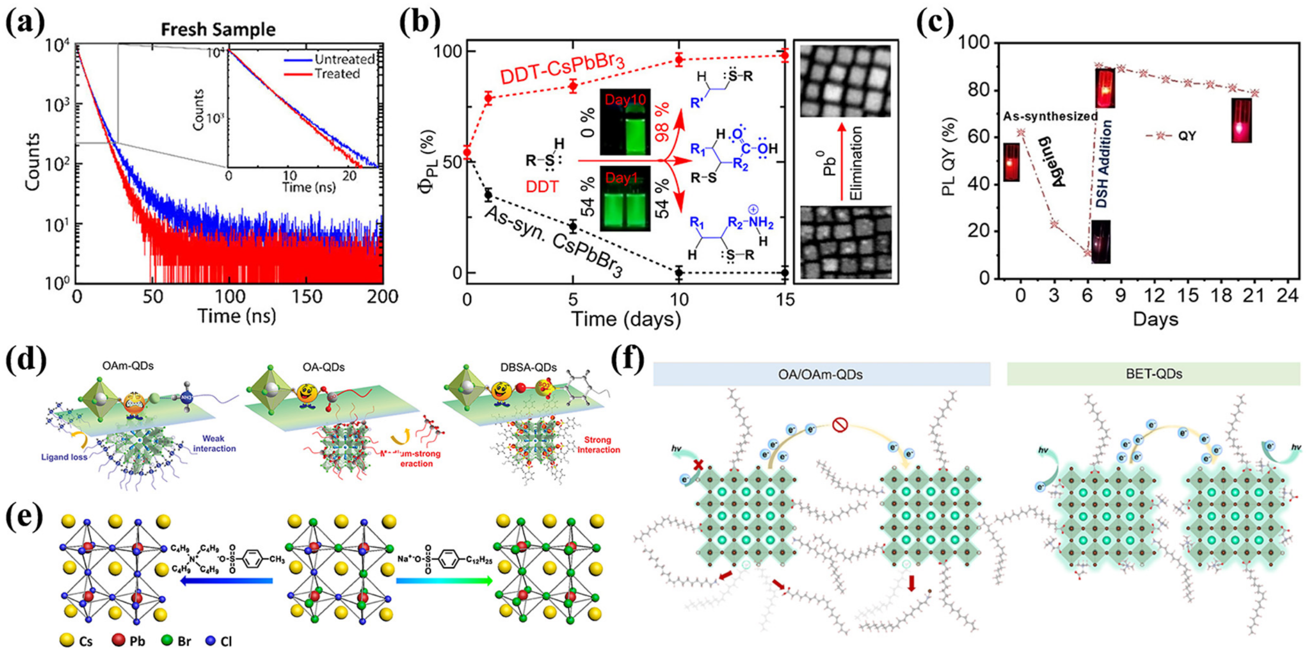

Fig. 10 (a) Time-resolved photoluminescence at room temperature for fresh $CsPbBr_3$ before and after ammonium thiocyanate treatment. Inset figures highlight the differences in the untreated and treated samples at early decay times. Reproduced with permission from ref. 155. Copyright 2017 American Chemical Society. (b) Curves of Φ_{PL} and photographs of sample under UV light (insight) over time for as-synthesized and DDT-treated $CsPbBr_3$ NCs. Reproduced with permission from ref. 165. Copyright 2019 American Chemical Society. (c) Photoluminescence quantum yield (PLQY) of as-synthesized, aged (6 days), and DSH-treated $CsPbI_3$ NCs instantly after treatment (DSH_Instant) and after 1 day (DSH_1Day). Reproduced with permission from ref. 168. Copyright 2023 Wiley-VCH. (d) Binding motif on $CsPbBr_3$ NC surface and interaction strength of OLA, OA, and DBSA ligands. Reproduced with permission from ref. 176. Copyright 2019 Wiley-VCH. (e) Schematic illustration of the halogen exchange process triggered by TBAS and SDSA. Reproduced with permission from ref. 178. Copyright 2020 American Chemical Society. (f) Schematical diagram of the effect of the betaine-capped NCs. Reproduced with permission from ref. 185. Copyright 2023 Elsevier Ltd.

colloidal stability of $CsPbBr_3$ NCs. Similarly, Tian *et al.* combined NaSCN with DDAB to modulate bromine vacancy density, thereby passivating surface defects and enhancing the stability of NCs.[156] The integration of this surface treatment into a solution-processed LED structure led to a significant enhance the maximum luminance from 550 to 1200 cd m^{-2} and a reduction in the turn-on voltage.

In addition to Na^+ and NH_4^+ ions, the cations of thiocyanates, KSCN[157] and $Pb(SCN)_2$,[152,158] are widely used in LEDs. K^+ seized X^- and worked with SCN^- to impede the halide migration through coordinated bonding with detrimental uncoordinated halide sites and vacancies, obtaining high EQE (2.04%) and stability of blue PeLED (~470 nm) without halogen separation.[157] $Pb(SCN)_2$, usually employed as the lead source, can partially or completely substitute PbX_2 without introducing impurities. Due to the ambidentate linear structure of SCN^-, these ligands function as spacers between distinct NCs, hindering aggregation and improving colloidal stability.[158] Notably, the chemical bond strengths of Pb–S or Pb–N surpass that of Pb–Br, enabling SCN^- ions to distort the crystal structure and up-shift the CB position.[152] Additionally, the organic pseudohalide *n*-dodecylammonium thiocyanate (DAT) has been deployed as a ligand in mixed halide (Br/Cl) perovskites as well.[159] The SCN^- ions sourced from DAT effectively filled Cl vacancies and removed electron traps within the bandgap. This optimization led to the production of high-efficiency blue PeLEDs with an emission wavelength of approximately 470 nm and EQE of 6.3%.

The incorporation of SCN^- ions can modulate both the optical properties and carrier dynamics related to the radiative recombination processes in perovskite materials. For instance, NaSCN has been shown to completely suppress the formation of charged excitons that are detrimental to PLQY.[160,161] Moreover, SCN^- ions have been found to hide the flickering phenomenon[162] and are widely utilized in solar cell applications.[163]

Thiols

As X-type ligands, alkanethiols of different chain lengths can form Pb–S bonds, significantly decreasing surface energy and maintaining the stability of perovskite materials.[164] Dodecanethiol (DDT), with its 12C chain, acts as a suitable ligand for post-treatment in the $CsPbX_3$ system, often in conjunction with OA/OLA.[165–168] DDT undergoes a thiol–ene reaction with OA, OLA, and octadecene (ODE) to become a thioether, as shown in Fig. 10b. These thiol and/or thioether ligands exhibit strong binding affinity to uncoordinated Pb^{2+} ions, inhibiting Pb^0 formation and achieving near-unity PLQY.[165] However, Jeon *et al.* found that DDT treatment, while increasing PLQY, also reduced the material's lifetime due to the production of nonradiative V_{Br} recombination fractions.[166] Additionally, DDT plays a dual function in rejuvenating the degraded α-$CsPbI_3$ NCs, as shown in Fig. 10c. Notably, α-$CsPbI_3$ NCs are susceptible to environmental degradation and often transform into a non-luminous δ-phase through the "α–γ–δ" pathway. DDT serves two objectives when added to the "sicked" $CsPbI_3$ NCs: (i) it binds with Pb^{2+} and I^- ions to passivate existing "healthy" NCs and (ii) it utilizes its etching capabilities to promote the α-$CsPbI_3$ phase by selectively removing the heavily aged Cs_4PbI_6 components.[168] Consequently, significant improvements in both the PL and environmental stability were observed. Moreover, DDT in synergy with AlX_3 can catalyze the morphological transition from nanocubes to nanoplates.[167]

The 1-octanethiol (OT), characterized by its relatively short aliphatic alkyl chains, facilitates robust surface adsorption due to minimal steric hindrance.[169] Through comparing the different lengths of the aliphatic alkyl chains, the thiol functional groups in OT anchored to Pb^{2+}, hindering the structural transformation and improving the photostability. Deng *et al.* reported enhanced stability through a multi-step ligand exchange process involving OT, which yielded a stable passivation molecular layer that withstood ethanol washing.[164] Moreover, the *in situ* incorporation of OT as capping ligands during synthesis markedly improved the tolerance of high-temperature and high-humidity conditions.[170] It has been found that 1,3-propanedithiol (PDT) and OLA together trigger irreversible transformation of $CsPbBr_3$ to Cs_4PbBr_6. PDT serves as a capping ligand to regulate the size uniformity and chemical stability of Cs_4PbBr_6 NCs.[171] In addition, materials containing –SH groups, such as 1-octadecanethiol,[172] butanethiol,[173] green fluorescence BODIPY molecule,[174] and porphyrin-thiol,[175] have been extensively studied for similar applications.

Sulfonic acid or sulfonates

Recently, ligands featuring sulfonate groups which are known for their strong acidity and electron-withdrawing capabilities, have garnered considerable attention. The sulfonate head of dodecylbenzene sulfonic acid (DBSA) interacts tightly with exposed lead ions, ameliorating electronic structural defects and repairing Br^- vacancies. In Fig. 10d, the anchoring effect of sulfonate groups on the surface of $CsPbBr_3$ NCs effectively minimizes exciton trapping and confers enhanced stability against degradation throughout purification, storage, and irradiation processes.[176] Sodium dodecyl benzene sulfonate (SDSA)[177] exhibits a notable affinity for $CsPbI_3$ NCs due to $-SO^{3-}$ in the ligand strongly binding with uncoordinated Pb^{2+} and filling the V_I. The inclusion of SDSA sustained a PL intensity of 83% after 60 days of environmental exposure. Furthermore, SDSA and tetrabutylammonium *p*-toluenesulfonate (TBSA) collectively facilitate halogen exchange between Cl^- and Br^- ions, enabling spectral tuning without requiring additional halogen compounds, as depicted in Fig. 10e.[178] In comparison with dodecylbenzenesulfonic acid (DSA) and sodium *p*-toluenesulfonate (SSA), evidence suggests that both cationic and anionic components in TBSA and SDSA are essential for determining the direction and extent of the halogen exchange. The use of $-SO^{3-}$ for surface passivation increases the PLQY from 7% to 81%, with blue PeLEDs owning a promising EQE of 2.6%. The introduction of short-chain aromatic backbones like 2-naphthalenesulfonic acid (NSA) during the purification process not only substitutes for OA but also forms strong interactions with the NC surface through the sulfo group coordinate with Pb.[179] The interaction between the NSA and $FAPbBr_3$ NCs effectively doubled the PLQY from 46% to 93%, enhancing the surface performance. NSA–$FAPbBr_3$ PeLEDs owned a three order of magnitude increase in current density and achieved a high brightness of 67 115 cd cm^{-2} with an exceptional EQE of 19.2%, which hindered efficiency roll-off. Moreover, molecules containing sulfonic acid groups have also showed potential as photosensitizers[180] and as ligands for modulating nanoparticle size.[181]

Zwitterionic ligands

Recently, zwitterionic ligands have emerged as a novel class of capping ligands for PNCs, offering the advantage of simultaneous surface passivation by positively and negatively charged groups. The main difference between zwitterionic ligands and traditional ligands is including:[182] (i) there is no potential for either mutual or external neutralization of cationic and anionic moieties *via* Brønsted acid–base equilibria; (ii) the surface of NCs is stabilized by a strong bidentate effect, establishing chemical equilibrium. As a result, improvements in the optical properties, colloidal stability, and charge transfer of PNCs have been observed. Specifically, the long-chain sulfobetaine zwitterionic molecule, such as 3-(*N*,*N*-dimethyloctadecylammonio)propanesulfonate (SBE-18) has been effectively introduced as a substitute for OA and OLA in $CsPbBr_3$ colloidal systems, exhibiting enhanced durability even after four wash cycles due to its chelating ability.[182] Despite its long alkyl chain, SBE-18 did not significantly impede charge transport, resulting in PeLEDs with an EQE of 2.5%. In contrast to the protonation and deprotonation processes observed in OA and OLA, SBE-18 uniquely anchor to the surface *via* amino and sulfonate groups, enabling simultaneous binding to both anions and cations.[183] Experiments revealed that zwitterionic ligands-treated NCs surfaces often reduce the size uniformity of the as-synthesized colloid. However, the $CsPbBr_3$ NCs coated with SEB-18 demonstrated homogeneity and yielded controllable average sizes, ranging from 3.5 to 16 nm.[184] During solvent evaporation, SBE-18-treated NCs exhibited a propensity for long-range ordered superlattice formation. Similar effect in betaine-capped NCs contributed to high EQE values of 10.8% and enhanced durability, as shown in Fig. 10f.[185]

Zwitterionic polymers with enhanced solubility have garnered research interest. Traditional zwitterionic ligands often have limited solubility in nonpolar organic solvents because of their intrinsic dipole properties. By leveraging poly(isobutylene-*alt*-maleic anhydride) (PIMA) as the foundational structure and incorporating poly(ethylene glycol) (PEG) as solubilizing blocks, Mattoussi and colleagues synthesized polyzwitterionic polymers, denoted as ZW–PIMA–PEG, through nucleophilic addition reactions.[186] These polymers feature both amine and sulfobetaine functional groups. The sulfobetaine groups in ZW–PIMA–PEG coordinated with Pb^{2+} ions, while the steric hindrance introduced by the short PEG segments enabled efficient surface passivation by facilitating close bonding to the surface. Utilizing this ligand enhanced the colloidal stability of the NCs, allowing their solubility in a broad range of polar solvents over extended durations (1.5 years) while concurrently preserving their photophysical attributes. Similar improvements in surface passivation and stability have been observed with poly(carboxybetaine acrylamide) (PCA)[187] and poly(BMA-*co*-2-(methacryloyloxy)ethyl-sulfobetaine) (PBMA-SB).[188] The strategic selection of functional groups allows for the design of photocrosslinkable zwitterionic ligands, thereby enabling the fabrication of directly patternable PNCs.[189]

The predominant functional groups in the amphoteric ligands include sulfobetaine, choline phosphate, and amino acids. Soy lecithin, a naturally abundant phospholipid, acts as an efficacious zwitterionic capping ligand that anchors robustly to its surface. The ligand density and spatial arrangement of lecithin chains contribute significantly to both solution phase formation and structural integrity across a wide concentration range, extending to as low as a few ng mL^{-1}.[190] Similarly, lecithin addition to $CsPbI_3$ NCs enabled phase stability in ambient air for six months.[191] PeLEDs fabricated with lecithin-capped NCs showed an EL peak at 634 nm, satisfying Rec. 2020 red standards, with the L_{max} of 1391 cd m^{-2} and the operational T_{50} of 33 min. This high performance is primarily attributed to the interaction with lecithin to alleviate lattice strain and demonstrate a heightened affinity for the $CsPbI_3$ surface.

In the synthesis of $CsPbBr_3$ NCs, Grisorio and co-authors incorporated an auxiliary bromine source, 8-bromooctanoic acid (BOA).[192] This compound ionizes to release Br^- ions, while the residual moiety undergoes an SN_2 reaction with OLA to form a zwitterionic ligand. This features both dialkylammonium and carboxyl groups, exhibiting a zwitterionic nature. The NCs capped with this zwitterionic ligand shown reduced solubility in nonpolar solutions, allowed purification using hexene, and maintained stability for three months in dichloromethane (CH_2Cl_2). Upon UV irradiation, the $CsPbBr_3$ NCs underwent halide exchange with CH_2Cl_2 as Cl^- sources, leading to a spectral blue shift.

Multidentate ligands

In contrast to other ligands, multidentate ligands offer multiple coordinating groups on the NC surface, yielding more stable and enduring bonds with NCs. The distinction between zwitterionic ligands and multidentate ligands lies in the fact that zwitterionic ligands carry both positive and negative charged components, whereas multidentate ligands establish multiple coordination sites with the metal *via* several functional groups. For instance, in Fig. 11a, the combined treatment of $MAPbI_2Br$ NCs with ethylenediaminetetraacetic acid (EDTA) and reduced L-glutathione (GSH) effectively bound surface Pb^{2+} ions, mitigated surface defects, and suppressed halide migration.[193] This led to a high-efficiency red LEDs with a peak emission at 620 nm and an EQE of 20.3%. DFT calculations confirmed that EDTA and GSH maximized the formation energy of iodide Frenkel defects at 0.18 eV, lowering the likelihood. The experimental results indicated that EDTA played a key role in enhancing the device efficiency, while GSH exhibited a stronger surface attachment compared to EDTA, thereby proving more stability. The concurrent presence of

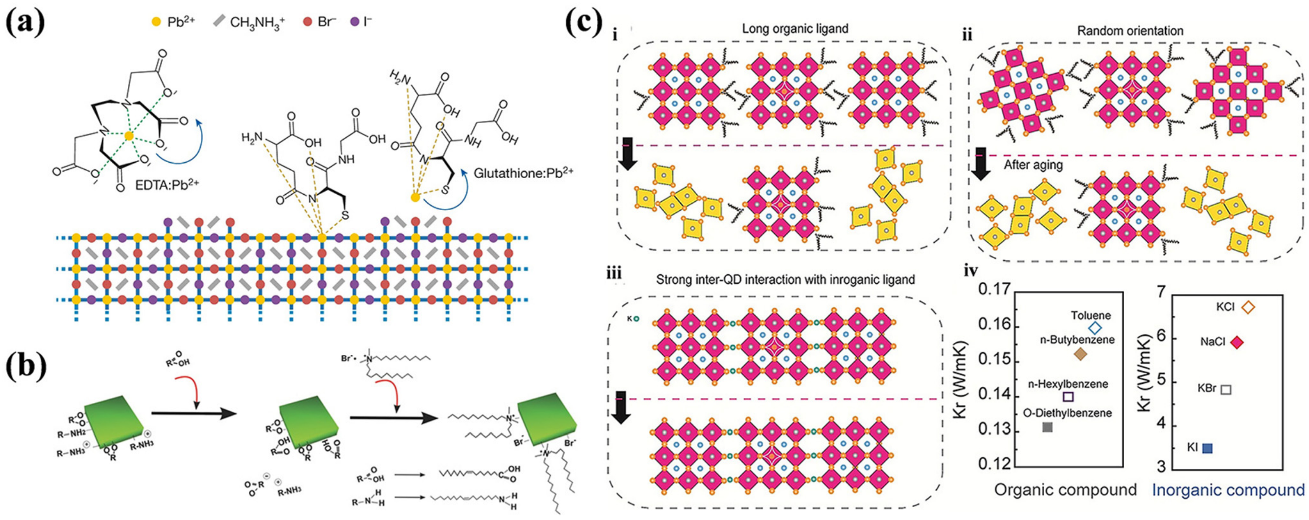

Fig. 11 (a) Schematical diagram of the interactions of GSH and EDTA with Pb^{2+} atoms on the NCs surface. Reproduced with permission from ref. 193. Copyright 2021 Springer Nature. (b) The ligand-exchange mechanism on $CsPbBr_3$ NC surfaces treated sequentially by OA and DDAB. Reproduced with permission from ref. 199. Copyright 2016 Wiley-VCH. (c) Formation of strained films with increased thermal transport. Reproduced with permission from ref. 201. Copyright 2021 Wiley-VCH.

amino and carboxyl functional groups is indispensable in the synthesis of NCs. Unlike individual ligands, such as OA or OLA, which contain either amino or carboxyl groups, peptides offer both functionalities within a single molecular structure.[194] This dual functionality effectively passivates Br^- vacancies and Pb^{2+} sites on the NC surface. Peptides, when varied in chain length and concentration, can regulate the optical properties and dimensions of $MAPbBr_3$ NCs. Specifically, L-cysteine serves as a representative trifunctional amino acid ligand, featuring three functional groups: $-NH_2$, $-COOH$, and $-SH$.[195] This multifunctionality results in a 6.9-fold enhancement in PLQY and yields a PL lifetime of 642 ns. In the synthesis of NCs, replacing OA with succinic acid and combining OLA as a synergistic ligand led to enhanced aqueous stability.[196] This is attributed to the dual carboxylic acid groups in succinic acid, which chelate two exposed Pb sites on the NC surface, thereby significantly improving the stability against the aqueous environment. Post-treatment passivation using 2,2′-iminodibenzoic acid (IDA) stabilized the α-phase in $CsPbI_3$ NC-based red LEDs, achieving a PLQY exceeding 95%.[197] IDA showed superior surface attachment compared to OA, owing to its dual carboxylic groups that securely coordinate with Pb sites. Utilizing IDA-NCs resulted in PeLEDs with a notable EQE of 5.02% and L_{max} of 748 cd m^{-2}. This enhanced performance is attributed to the effective electronic coupling between the LUMO of IDA and the conduction band edge of $CsPbI_3$ NCs, rather than the conductivity of IDA.

Ammonium salts

Ammonium salts are instrumental in optimizing the properties and applications of NCs through various means including surface modification, stability enhancement, optical property modulation, and biocompatibility. Ammonium compounds such as alkyl ammonium salts typically exhibit hydrophobic characteristics. They form adsorptive layers on NC surfaces, thereby enhancing both dispersibility and NC stability, and preventing aggregation and precipitation. Through the strategic selection of specific ammonium salts and modification of substituents, the surface properties of the NCs can be precisely tailored. This fine-tuning occurs because the positively charged moieties in the ammonium salts interact with the negatively charged regions on the NC surface, leading to effective defect passivation. For instance, Kido *et al.* conducted a comparative study on the anion-exchange effects of alkyl ammonium (oleylammonium iodide, OMA-I), and aryl ammonium salts (aniline hydroiodide, An-HI) as I^- sources to deep-redshift emission.[198] The addition of ammonium salts influenced not only the desorption of OA from the original NC surface, but also the surface ligand density. $CsPbI_3$ PeLEDs treated with long alkyl-based OMA-I demonstrated a high EQE of 21.3% and superior color purity compared to aryl-based An-HI-capped NCs. However, devices with aryl-based An-HI-capped NCs demonstrated significantly higher operational stability, lasting 36 times longer. Additionally, the PLQYs of the colloidal solutions were 80% for OAM-I NCs and 69% for An-HI NCs, which was attributed to the effective suppression of anion defects. Bakr *et al.* utilized a halide ion pair-based capping agent DDAB to synthesize highly stable $CsPbX_3$ NC films.[199] This relatively compact ligand structure enhanced carrier mobility within the NC films and facilitated efficient PeLEDs fabrication. Effective DDAB passivation was achieved by incorporating OA into the synthetic solution. The acidic protons facilitated the protonation-mediated removal of the OLA ligands, resulting in the formation of acid–base complexes with deprotonated OA groups, as shown in Fig. 11b. These complexes promoted Br^- coordination with Cs^+ or Pb^{2+} ions and influenced adsorption onto the NC surface because of the steric hindrance of DDA^+ while also maintaining the solubility of the NCs in toluene.

Z-type ligands

Alkali metal salts. Z-type ligands are typically Lewis acids characterized by unoccupied orbitals that are capable of accepting electrons from surface atoms. In the octahedral $[PbX_6]^{4-}$ structure, uncoordinated Pb^{2+} ions typically serve as Lewis acids, whereas the X^- ions, acting as Lewis bases, commonly coordinate with them. At the present time, alkali metal salts provide empty orbitals to accept halogen atoms from the surface. The appeal of K^+ ions stem from their small atomic radius and strong affinity for surface X^- ions, generating significant interest in their interactions. Through the incorporation of potassium oleate (K-OA) during the synthesis of $CsPbI_{3-x}Br_x$ NCs, we have highly achieved color-stable pure red PeLEDs and PL stable NCs for weeks, effectively mitigating halide migration phenomena.[109] Synchrotron radiation photoemission spectroscopy (SRPES) characterization confirmed that the majority of K^+ ions predominantly reside on the surface, facilitating robust interactions with Br^- ions, weakening the bond between Pb^{2+} and Br^-. A smaller fraction of K^+ ions were situated within the interstitial spaces of the NCs. This dual effect of KBr termination efficiently passivates the surface defects, resulting in NCs with a remarkable PLQY exceeding 90%. Subsequent device fabrication demonstrated a significantly elevated EQE of 3.55% and luminance of 2671 cd m^{-2} compared to the control devices. Similar enhancement effects were also observed in blue $CsPb(Br/Cl)_3$ NCs and devices, leading to the production of a spectrally stable and highly efficient blue PeLED, achieving a maximum EQE of 1.96% at the emission peak of 477 nm.[200] Inorganic ligands maximize thermal conductivity compared to traditional organic ligands. Therefore, the incorporation of highly thermally conductive KI into the $CsPbI_3$ system not only improved heat dissipation of the film but also promoted stronger interactions between dots, leading to stress relaxation and effective passivation of surface halide defects.[201] The films of $CsPbI_3$ NCs treated with KI exchange exhibited a close-packed and oriented arrangement, as depicted in Fig. 11c. Moreover, K^+ ions were not doped into the lattice, facilitated mechanical coupling and exchanged surface OA and OLA desorption. The presence of K^+ ions and all-inorganic ligands proved advantageous for enhancing device performance. The red LEDs demonstrated an impressive maximum EQE of 23% and an operating half-lifetime of 10 h, showing a notable 6% improvement compared to the control devices.

4.2 Passivation strategies for LHP films

The fabrication of polycrystalline perovskite thin films, whether *via* one- or two-step spin-coating methods, exhibits subtle distinctions compared to NCs. Notably, the latter approach yielded a higher grain boundary density. These grain boundaries contribute to elevated surface defect concentrations, subsequently influencing charge carrier transport and photoluminescence efficiency. Improvements in the performance of polycrystalline film devices can be achieved through various pre-processing techniques, including optimization of precursor solution concentration and ratio, solvent engineering, incorporation of additives, and the implementation of diverse post-processing strategies. Various post-processing strategies, such as annealing treatment and interface passivation, have been developed to passivate film defects. Pre-processing methods principally focus on controlling the nucleation rate and crystallization kinetics of perovskite films to attain well-defined crystal structures, thereby mitigating defect formation. In contrast, post-processing procedures are directed at reducing defects on the surface of perovskite thin films, thus enhancing their transport properties and ultimately leading to the realization of high-efficiency PeLEDs.

4.2.1 Component regulation. One of the advantages of perovskite materials is their ability to modulate optoelectronic characteristics through material composition manipulation. As outlined in Section 2.1, the synthesis of LHP films involves the combination of AX and PbX_2 to create an $APbX_3$ structure, where the parameters τ and μ are determined for structural stability. Consequently, the adjustment of cation and anion compositions to engineer perovskite structures holds significant theoretical promise for reducing the defect states within perovskite thin films. The lattice structure and dimensions are predominantly influenced by the A-site cations, which are intricately linked to the optical performance and stability of the devices.[134] In the perovskite phase, there is a progressive increase in octahedral tilting among the cations FA^+, MA^+, and Cs^+, indicating that variations in cation size contribute to shaping structural distortions, as illustrated in Fig. 12a.[202] Therefore, cation mixing exerts a substantial influence, not only in improving perovskite morphology to mitigate high leakage current but also in reducing nonradiative recombination at grain boundaries.

Substituting the smaller MA^+ cation with the larger FA^+ cation led to a tolerance factor nearing 1, which expanded the octahedral structure slightly, resulting in enhanced luminance and repeatability in $FAPbBr_3$ PeLEDs.[203] Additionally, the incorporation of MA^+ cations with high dipole facilitated the stabilization of the α-phase of $FAPbI_3$ without necessitating high annealing temperatures.[204] It is widely recognized that all-inorganic LHPs generally exhibit greater structural stability compared to hybrid organic–inorganic LHPs, primarily due to the chemical instability of MA^+ or FA^+ and asymmetry and instability of the coordination environment within the lattice structure.[205] Inorganic cations like Cs^+, which are more size-compatible with halides, can facilitate a more symmetric and stable coordination environment, thereby enhancing the overall stability of the perovskites. For instance, $CsPbX_3$ perovskites demonstrate significantly elevated thermal decomposition temperatures (approximately 580 °C for $CsPbBr_3$) compared to $MAPbBr_3$ (approximately 220 °C).[206] However, due to the relatively weak interaction between FA^+ cations and halides, the introduction of Cs^+ cations can effectively enhance crystallinity and improve optical/thermal stability.[207] Similarly, when Cs^+ is incorporated into MA-based perovskite crystals, thin films exhibit nearly complete surface coverage and display

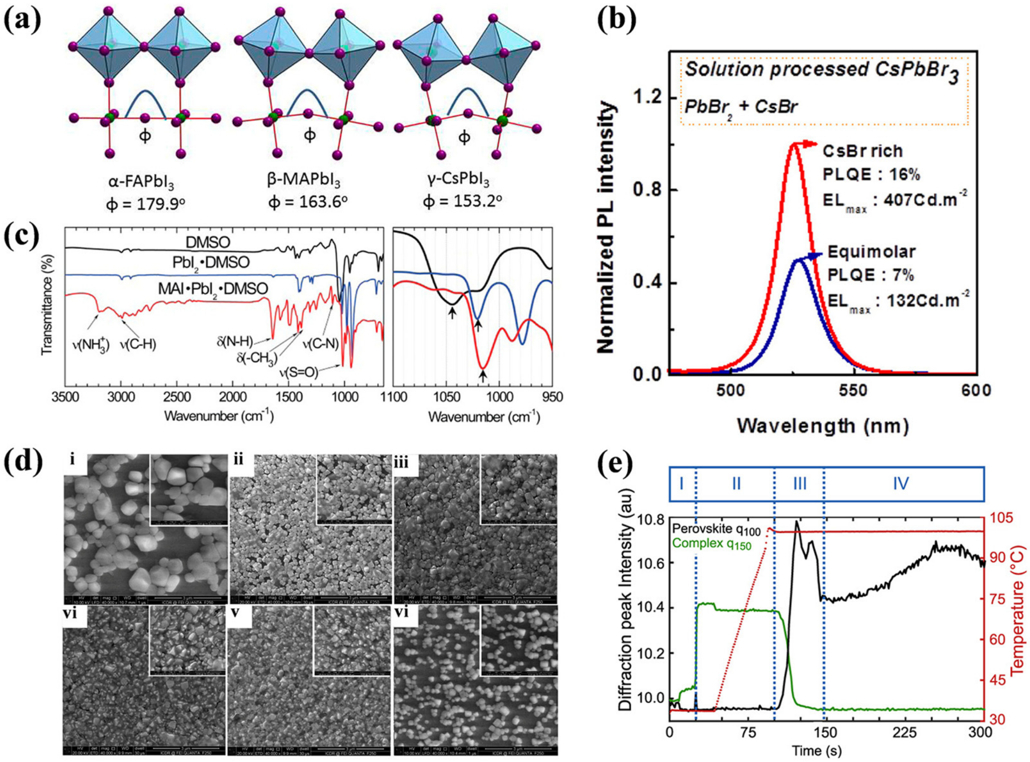

Fig. 12 (a) Structural deformations of the ideal 180° B–X–B bond angle induced by the A-site cation size. Reproduced with permission from ref. 202. Copyright 2015 American Chemical Society. (b) Performance of PeLEDs based on $CsPbBr_3$ films with and without excess CsBr. Reproduced with permission from ref. 205. Copyright 2015 American Chemical Society. (c) FTIR spectra of DMSO (solution), PbI_2·DMSO (powder), MAI·PbI_2·DMSO (powder), and expanded the fingerprint region for the S=O vibrations. Reproduced with permission from ref. 216. Copyright 2015 American Chemical Society. (d) Top-view SEM images of $MAPbBr_3$ films deposited on PEDOT:PSS/ITO substrates. The $MAPbBr_3$ films were fabricated using solutions with different CB/DMF ratios of 0/1 (i), 1/10 (ii), 2/10 (iii), 3/10 (iv), 4/10 (v), and 4/10 (vi), respectively. Reproduced with permission from ref. 219. Copyright 2009 Royal Society of Chemistry. (e) Temporal evolution of radially integrated GIWAXS data of MAPI (black) and MAPI·DMSO solvent-complex (green) as well as temperature (red) during the crystallization process of perovskite solvent complex at 100 °C. Reproduced with permission from ref. 227. Copyright 2021, Springer Nature.

favorable emission characteristics.[208] Conversely, the addition of MA^+ molecules to all-inorganic $CsPbBr_3$ films facilitate in reducing pinholes by controlling crystallization kinetics. This synergistic approach, combined with interface engineering, has yielded high-performance mixed-cation $Cs_{0.87}MA_{0.13}PbBr_3$ PeLEDs with a peak brightness of 91 000 cd m^{-2} and a peak EQE of 10.43%.[209] In cases where an oversized A-site cation is used, it can lead to the segmentation of the 3D perovskite structure into multilayered quasi-2D perovskites with low defect generation, such as $PEA_2(CsPbBr_3)_2PbBr_4$.[210] For example, through DFT calculations, the intercalation of aliphatic or aromatic alkylammonium cations between perovskite layers resulted in significant van der Waals interactions, as observed quantitatively. This increase in formation energy contributed to enhanced stability.[211]

In addition to A-site cation adjustments, the precise control of reactant stoichiometry plays a pivotal role in defect passivation. Reaction stoichiometry governs the exact correlation between substances involved in chemical reactions.[56] In the context of perovskite precursor solvents, the standard chemical stoichiometric ratio of raw materials is 1 : 1, inevitably leading to the formation of defects, such as metallic lead atoms. Therefore, increasing the nonstoichiometric ratio of the raw materials has proven to be an effective strategy for reducing defect formation. Varying the concentrations of CsBr and $PbBr_2$ in DMSO was found to decrease the defect density, resulting in enhanced performance of PeLEDs.[205] This enhancement is evident in the prolonged PL lifetime and higher PLQY, as depicted in Fig. 12b. Employing a CsBr-rich solution led to an exceptionally narrow FWHM, increased luminescence, along with a decreased V_{on} in PeLEDs. The incomplete reaction between MABr and $PbBr_2$ at a 1 : 1 stoichiometry can lead to the formation of metallic Pb atoms.[212] To avoid the generation of metallic lead atoms, incremental increases in the molar ratio of MABr by 2 to 7% in the $MAPbBr_3$ solution were successfully accomplished.[213]

In contrast to the demands of PSC applications, the control of A-site cations and nonstoichiometric ratios in perovskite materials involves not only the modulation of film morphology, but also the imperative reduction of grain size. This reduction is essential for facilitating efficient electron and hole confinement, enabling effective radiative recombination in

LED devices. However, small grain sizes often lead to an increased prevalence of grain boundaries and defects. Therefore, the effective passivation of defects is a critical factor in upgrading LED performance. Achieving an optimal balance between promoting grain growth and effectively passivating defects is instrumental in fine-tuning the mixture of A-site cations and stoichiometric ratios.

4.2.2 **Solvent engineering.** A significant advantage of perovskite materials is their suitability for solution processing. However, this advantage can introduce challenges, including the formation of pinholes and defects during solution processing, which can subsequently lead to leakage currents and performance degradation in the devices. As previously discussed, perovskite thin films are synthesized through a straightforward method involving the spin-coating of perovskite precursor solutions. These solutions were prepared by dissolving the AX and PbX_2 salts in a polar protic solvent, followed by centrifugation and solvent evaporation. The spin-coating process is intricately linked to the viscosity, saturation vapor pressure, and boiling point, which collectively govern the perovskite crystallization and film morphology. Consequently, the choice of solvent plays a pivotal role in the crystallization of perovskite films.

Within the precursor solution system, Pb^{2+} acts as a Lewis acid, adeptly accepting electron pairs from X^- ions or solvents such as *N*,*N*-dimethylformamide (DMF), dimethyl sulfoxide (DMSO), *N*-methyl-2-pyrrolidone (NMP), and thiourea, all of which serve as Lewis bases.[56] This dynamic interplay establishes a nuanced acid–base equilibrium, fostering intricate interactions among these components to form an intermediate phase.[7] This intermediate entity is crucial for affecting both the nucleation and growth processes of perovskites, subsequently exerting a specific impact on film morphology and defect density. As an illustrative example, we consider the formation of $MAPbI_3$ perovskite films to elucidate the role of the solution in constructing the intermediate phase. Initially, PbI_2 dissolved in a solvent exhibited a layered structure held together by van der Waals interactions. Upon the addition of MAI, competition arose between the solvent and the I^- ions to coordinate with PbI_2. On the one hand, a relatively low activation energy facilitated intercalation reactions between the layered PbI_2 and I^-. This process involves the dissociation and reformation of chemical bonds between Pb and I in PbI_2, resulting in a series of iodoplumbate coordination complexes, including PbI_3^- and PbI_4^{2-}. Notably, a discernible relationship emerged between the concentration of PbI_4^{2-} and the density of charge recombination centers in the generated perovskite thin films.[214] On the other hand, a highly coordinating solvent could displace I^- ions from their coordination sites with Pb^{2+} ions by solvent molecules. Consequently, the presence of this intermediate phase within the precursor solution effectively hinders perovskite crystallization. However, it is essential to note that the current understanding of the formation of intermediate phases during perovskite crystallization is characterized by the absence of reliable experimental methods to directly confirm their presence.[215] This challenge is primarily due to the rapid nature of the crystallization process and the inherent instability of these intermediate phases. Additionally, contentious debate remains regarding whether these intermediate phases manifest as distinct crystal lattice structures or amorphous phases. Summarily, dissolving PbI_2 in DMF along with equimolar amounts of DMSO and MAI yielded intermediate phases of $PbI_2\cdot DMSO$ and $MAI\cdot PbI_2\cdot DMSO$, as corroborated by shifts in the stretching vibration of S=O at 1020 cm^{-1} and 1015 cm^{-1}, respectively, upon reaction with PbI_2 and PbI_2 + MAI, as depicted in Fig. 12c.[216]

From the preceding discourse, the influence of various solvents on the crystallization process and, consequently, the film morphology is a key consideration. These commonly used solvents, which subtly differ in polarity, solubility, and binding capabilities, produce diverse complexes during the precursor stage. Gutmann's donor number (DN) was employed to quantify solvent solubility of solutions in perovskite precursors, especially for cations and Lewis acids.[217] Solvents with high-DN values tend to bind Pb^{2+} centers, suppressing the formation of iodoplumbate complexes and retarding perovskite crystallization. In contrast, solvents with low-DN values have weak Pb^{2+} affinity, enabling the formation of iodoplumbate complexes and supporting the growth of perovskite single crystals.[218] By blending solvents with varying DN capabilities, it becomes possible to manipulate the shape of intermediate complexation species, adjust coordination interactions within the solution, and effectively control the crystallization process of perovskites.[7] Wu and coworkers demonstrated a straightforward one-step solution-based approach for enhancing perovskite film morphology by utilizing a diverse range of DN values in a nonsolvent/solvent mixture. As depicted in Fig. 12d, the impact of different CB/DMF ratios on $MAPbBr_3$ film morphology was evident, with an increase in the proportion of CB leading to enhanced coverage and decreased grain size.[219] The improved film morphology was attributed to the influence of the combined solvent on the nucleation process during film formation, leading to an increased nucleation rate due to the low solubility of CB in the crystallization process. This led to a smaller grain size in the $MAPbBr_3$ film. The achievement of high-coverage and small-sized films effectively reduced the device leakage current, resulting in a device with an L_{max} of 3846 cd m^{-2}.

Crystallization occurs upon reaching a state of supersaturation in the solvent, and the anti-solvent expedites this process by accelerating the nucleation rate of the perovskite film. This is achieved by adding the anti-solvent dropwise during the spin-coating process, which flushes away the solvent within the precursor, inducing supersaturation and rapid precipitation of the precursor solution.[220] Increasing experimental evidence underscores the imperative role of incorporating anti-solvents as a specific method for producing uniformly dense films, while concurrently addressing inherent defects. The anti-solvent not only modulates the nucleation rate during spin-coating but also exerts a profound influence on crystal growth and film morphology. Commonly used anti-solvents in PeLEDs include CB, chloroform, ethyl acetate (EA), and mixed anti-solvent solutions. Comprehensive anti-solvent comparisons have revealed that CB, when employed as the anti-solvent, efficiently removes solvents from the precursor solution and leverages the inherent chloride ions within CB to adeptly passivate surface bromine vacancies in $MAPbBr_3$, as substantiated by XPS analysis.[221] Nonetheless, the high boiling point of CB at 132 °C presents a predicament as a substantial residue of CB often remains within the films, potentially posing toxic or hazardous environmental issues.[222] In contrast, the eco-friendly green solvent EA, known for its low boiling point and easy removal after thermal treatment, offers a favorable option for generating denser and more uniform thin films.[223] It is important to note that iodine-based films treated with EA tend to increase grain size, while bromine-based films exhibit only marginal increases while concurrently diminishing grain boundaries, effectively passivating defects at the grain boundaries.[224] Therefore, $MAPbBr_3$ films treated with EA exhibit an improved crystalline structure, refined morphology, and diminished defect density, thereby in turn enhancing the operational efficiency of the associated PeLEDs. Additionally, the timing of anti-solvent dropping during the film formation process also impacts surface morphology.[225,226]

Precise control of solvent engineering is of paramount importance because of its direct influence on surface morphology and defect states, thereby providing a means to regulate nucleation and crystal growth processes. Furthermore, there is a pressing need to expand the repertoire of solvent systems to accommodate diverse needs, particularly those related to eco-friendly solvents.

4.2.3 **Annealing treatment.** Annealing, a pivotal post-processing technique, has been strategically employed to control the nucleation, crystallization rate, grain size, thin films characteristics, and defect density in perovskite thin films. This approach aims to elevate the light emission efficiency, current efficiency, and overall robustness. The quality of the post-annealed films is intricately linked to solvent engineering, with both factors playing a crucial role in defect density control. However, understanding how annealing treatment affects film crystallization and defect modulation is a complex and challenging endeavor. Müller-Buschbaum *et al.* utilized grazing-incidence wide-angle X-ray scattering (GIWAXS) and PL spectroscopy for *in situ* monitoring, providing detailed insights into the intricate changes occurring in $MAPbI_3$ films during the annealing process using a one-step antisolvent-assisted crystallization method.[227] Prior to annealing, the addition of an anti-solvent induced a nucleation process, leading to a first-order phase transition. During this phase transition, metastable nuclei are connected through nanostructures, ultimately forming solvent complexes. Upon annealing, a secondary phase transition is initiated, driving the transformation of these solvent complexes entirely into $MAPbI_3$. During annealing, solvent evaporation was most rapid at the film–air interface, followed by the removal of the solvent from deeper interfaces through the already crystallized portion. This triggered a dissolution and recrystallization process, ultimately converting the clusters into $MAPbI_3$. This transformation is evidenced by the oscillatory changes in the Bragg peak observed in region III of Fig. 12e. These findings validate the understanding of structural variations in thin films, where crystallization occurs at varying rates across different film thicknesses due to processes such as solvent evaporation, interdiffusion, and colloidal assembly.[228,229] These processes lead to the emergence of physicochemical reaction gradients resulting from distinct rates of removal of tightly coordinated solvent molecules, facilitated by the advection of evaporating solvent molecules from different film thicknesses.[227]

Annealing exerts similar effects in both the one- and two-step methods. In the two-step method, an annealing treatment was employed to facilitate diffusion between the two layers of thin films, such as diffusion from the PbI_2/DMF solution to the MAI/IPA solution. Mativenga *et al.* varied the resting time between these steps to enable solvent-controlled growth of $MAPbI_3$ thin films, yielding films with fewer residues, pinholes, and defects.[230] During the intermediate resting period, gradual solvent evaporation mitigated the rapid evaporation of solvents in the second step, effectively decelerating the entire crystallization process and resulting in devices with reduced defects and enhanced performance. Furthermore, the residual stress in the lattice exhibited a linear dependence on the annealing temperature, with higher temperatures resulting in increased stress levels in the film.[231] Typically, films prepared using the two-step method exhibit greater residual stress than those prepared using the one-step method.

Annealing treatments have garnered attention for their capacity to rectify undesirable structural[232] and are acknowledged for inducing beneficial morphological transformations.[233] In a vacuum-deposition process, Luo *et al.* successfully engineered low-dimensional perovskite thin films of $PEA_2(Cs_{n-1}Pb_nBr_{3n+1})$ and subsequently improved the device performance with an impressive EQE of 6.5% through post-annealing treatment. Comprehensive analyses, including PL, space-charge-limited current (SCLC), and PLQY, coupled with kinetic assessments, indicate the effectiveness of the post-annealing approach. This led to a notable reduction in defect density, enhanced film morphology, a five-fold decrease in nonradiative recombination, mitigated the unfavorable contribution of the small *n*-phase to luminescence, and heightened the potential for radiative recombination.

The annealing parameters, including the number of annealing steps, duration, and temperature, exert a substantial influence on both the formation of defect states within the film and the optical performance of the devices. Furthermore, the annealing process also impacts the construction of the intermediate phase between solvents and precursors, with both annealing time and temperature playing pivotal roles in this regard.[234] On occasion, annealing can facilitate the transition between distinct perovskite phases; for instance, at 583 K, it induces the transformation from $CsPb_2Br_5$ to $CsPbBr_3$.[235] While solvent-vapor annealing is a well-established method, it finds greater application in PSCs[236] and is less commonly employed in LEDs. This discrepancy primarily arises from the propensity for a liquid or quasi-liquid phase to form on the film's surface under vapor conditions, resulting in the recrystallization of atoms in regions where grains are less compact or not in contact, ultimately leading to the formation of larger grains.[237] It is important to note that larger grains are generally unsuitable for light emission purposes.

Annealing, achieved through precise temperature control, is a valuable tool for optimizing microstructures within the crystal lattice and material interfaces. This enhances the intrinsic crystal quality and promotes the lattice homogeneity. Nevertheless, the selection of annealing conditions and their influence on the performance warrants further investigation. Careful consideration remains essential for determining the applicability of the annealing parameters in different application scenarios.

4.2.4 Additive engineering. As discussed in Section 4.1.2, NCs are susceptible to surface defects during purification. To mitigate this issue and obtain stable and efficient NCs, ligand-control methods have been employed to reduce defects. Similarly, in solution-processed polycrystalline films, uncontrollable nucleation and growth processes result in the inevitable generation of numerous defects. These defect sites have a propensity to adsorb water and oxygen, functioning as trapping sites for excitons upon adsorption, thereby affecting device performance.[238] To address these challenges, additive engineering is a widely adopted approach. Additives can be simply classified into two primary categories: organic and inorganic, and we discuss each category separately.

Organic additives. Certain organic molecules exhibit Lewis base characteristics, possessing available lone electron pairs that can interact with Pb^{2+}, reduce halide vacancies, enhance optical properties, and improve the efficiency and stability of PeLEDs. One approach involves the use of nonionic dielectric Lewis base polyethylene glycol (PEG) in $CsPbBr_3$ precursors, which physically fills grain boundaries and interacts with the perovskite crystal to passivate defect states.[239] The interaction binding between Pb^{2+} and PEG effectively reduced nonradiative recombination, resulting in a one-order-of-magnitude decrease in the decay rate and a significant reduction in grain size. Furthermore, stoichiometric ratio adjustments through coordinated chemistry yielded luminance levels of 36 600 cd m^{-2} and an EQE of 5.34%. Other organic polymer additives with similar effects include poly(ethylene oxide),[240] poly(2-ethyl-2-oxazoline),[241] and polyhedral oligomeric silsesquioxane.[242] Halide amines in ammonium salts can also passivate halide anions of the PbX_6^{4-} octahedra through hydrogen bonding between the amino groups and three halogen anions, effectively reducing defects.[56] For instance, multilayered quasi-2D perovskite films have been created by incorporating long-chain ammonium halides such as phenylethylammonium halides (PEAX),[206] *n*-butylammonium halides (BAX),[243] and ethylammonium halides (EAX),[210] transforming the dimension from 3D to 2D and facilitating bonding between the organic large cations and halides through hydrogen bonding. This approach is practical for producing pinhole-free films with low defect density. To prevent excessive crystal growth and alleviate surface defects, a substantial amount of bulky ammonium halide was introduced into quasi-2D perovskite films. However, akin to ligands in colloidal NCs, the excessive presence of ammonium halides can establish an insulating capping layer, hindering efficient carrier transport across nanometer-sized grains within the perovskite structure. Therefore, the inclusion of formamidine acetate (FAOAc) as an additive in $CsPbBr_{3-x}Cl_x$ perovskite films led to the fabrication of highly efficient blue PeLEDs (~477 nm).[244] Acetate ions in FAOAc facilitated the removal of excess ammonium ions, while FA^+ contributed to elevating the formation energy of the low-dimensional ($n = 2$) phase in Fig. 13a. This leads to the suppression of nonradiative recombination in the perovskite films, converting the $n = 2$ phase into a 3D phase. Consequently, efficient blue PeLEDs with a maximum EQE of 8.8% were achieved.

Another approach is the introduction of additives into the anti-solvent and deposit them in a post-deposition treatment process, which reduces and mitigates nonradiative recombination defects in polycrystalline perovskite films. The organic small molecule ethoxylated trimethylolpropane triacrylate (ETPTA) functions as a functional additive that is incorporated into the anti-solvent.[245] ETPTA effectively passivated and suppressed defects by interacting with undercoordinated Pb^{2+} ions through its C=O group. This process relies on the ability of ETPTA in anti-solvent to cover the surface of the thin film and permeate the grain boundaries. The ETPTA passivation treatment resulted in a high EQE of 22.49% and a threefold increase in operational stability. Similarly, the addition of 9,9-spirobifluoren-2-yl-diphenylphosphine oxide (SPPO1), which contains phosphine oxide functionality, to the anti-solvent also facilitated the passivation of defects at grain boundaries, thereby enhancing device performance.[246]

Multifunctional molecules have proven effective not only in enhancing the performance of NCs but also in thin films. For instance, Xiao *et al.* synthesized a dual passivation additive, 4-fluorophenylmethylammoniumtrifluoroacetate (FPMATFA), which achieved dual passivation of both Pb^{2+} and X^- in high-performance $FA_{0.33}Cs_{0.67}Pb(I_{0.7}Br_{0.3})_3$ red PeLEDs.[247] $FPMA^+$, with its strong NH_3^+ functional group at its end and electron-withdrawing F atom, enabled close binding with X^- ions through hydrogen bonds. TFA^- contributed lone electron pairs for interaction with uncoordinated Pb^{2+}, as supported by XPS and DFT analyses. This intricate passivation strategy with FPMATFA led to a remarkable increase in EQE, reaching an impressive value of 20.9% in mixed-halide PeLEDs. Additionally, the harmful impacts stem from hysteresis and phase segregation, attributed to defects and ion migration, were significantly alleviated. Similarly, the bifunctional amino acid-derived additive 5-aminovaleric acid (Ava) also exhibited similar passivation effects.[248,249]

Inorganic additives. Currently, inorganic metal salts are the predominant choice for inorganic passivation, offering effective mitigation of X-site vacancy defects and grain boundaries in perovskite materials. For example, the systematic application of passivating potassium halide on both the surface and grain boundary regions has been demonstrated to

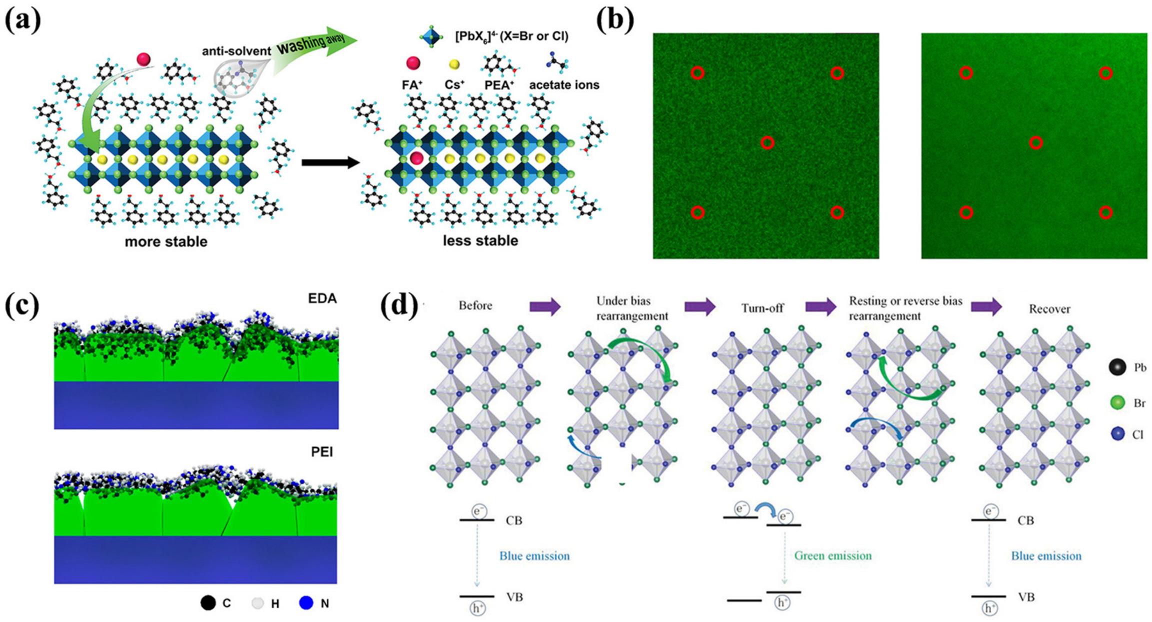

Fig. 13 (a) Schematic diagram of quasi-2D perovskite with FAOAc addition. Reproduced with permission from ref. 244. Copyright 2021 Wiley-VCH. (b) Confocal microscopy images of perovskite film on NiO_x (left) and NiO_x/PVK (right) substrates. Reproduced with permission from ref. 257. Copyright 2019 AIP Publishing. (c) Schematic illustration of the depthwise penetration of PEI/EDA into $MAPbBr_3$. Reproduced with permission from ref. 77. Copyright 2017 American Chemical Society. (d) Schematic diagram of halide ion migration under forward and reverse bias. Reproduced with permission from ref. 273. Copyright 2019 Wiley-VCH.

reduce nonradiative losses and photoinduced ion migration within perovskite films and interfaces.[250] Similarly, the use of lithium halides can yield analogous passivation effects, leading to devices with high EQE of up to 16.2%.[251] Strategically dispersing metal ions within grain boundary crevices effectively passivates defects and raises the defect formation energy, thereby reducing defect occurrence.[238] In addition to metal halide salts, certain inorganic salts containing thiolate ions can also serve as effective passivation agents for thin film defects. This is primarily because O atoms with unpaired electrons on the SO_3^- head group can form Lewis adducts, effectively coordinating with the Pb-exposed surface. Yang *et al.* effectively utilized methanesulfonate (MeS) in their study, and through rigorous analysis involving DFT calculations and NMR measurements, they demonstrated that MeS engaged in robust triple hydrogen bonding interactions with spacer BA cations.[252] This interaction played a pivotal role in modulating the crystallization kinetics of the quasi-2D perovskite structure. The incorporation of MeS resulted in a weakened adsorbate blocking effect of BA, promoted the formation of Lewis adducts, and contributed to a reduction in uncoordinated Pb ions, ultimately alleviating defect formation within the perovskite films. These effects facilitate the transition from small-*n* to large-*n* phases, thereby enhancing radiative recombination in the higher *n*-phase. Consequently, the green LEDs employing these quasi-2D RP perovskite films achieved remarkable performance metrics, including a high CE of 63 cd A^{-1} and an exceptional EQE of 20.5%.

4.2.5 Interface passivation.

Ionic defects significantly reduce the activation energy for ion migration, leading to device degradation under continuous bias conditions. In the context of PeLEDs, optimizing the radiative recombination efficiency is more than simply enhancing the quality of the perovskite film. It also necessitates the precise alignment of energy level structures and impeccable interface interactions. As encapsulated by Nobel laureate Herbert Kroemer's assertion that "interfaces are the devices", the pivotal role of interfaces in defect management has become apparent. Interface passivation has emerged as a potent strategy for defect mitigation, accomplished through the interaction between the passivation layer and dangling bonds on the perovskite surface, effectively neutralizing their detrimental effects. Interface passivation can be categorized into two types based on the introduction site of a passivation agent: upper and lower interface passivation.

Lower interface passivation. The anode buffer layer, poly(3,4-ethylenedioxythiophene):poly(styrenesulfonate) (PEDOT:PSS), employed in PeLEDs, processes hygroscopic and acidic properties that can lead to detrimental etching of indium tin oxide (ITO) anodes.[253] This etching effect results in exciton quenching and poses a substantial threat to the long-term stability of the devices. However, the relatively high injection barrier at the interface with perovskite hinders carrier injection. Indeed, commonly employed materials such as poly(9-vinylcarbazole) (PVK), poly(9,9-dioctylfluorene-*co*-*N*-(4-butylphenyl)diphenylamine) (TFB), and poly(*N*,*N*′-bis-4-butylphenyl-*N*,*N*′-bisphenyl)benzidine (poly-TPD) can function as interfaces between PEDOT:PSS and perovskite, effectively alleviating exciton quenching resulting from direct contact. These materials establish stepped energy level barriers, thus facilitating hole injection.[254] Moreover, when an ultrathin LiF interlayer was applied to coat PEDOT:PSS, the wettability of the mixed DMF/DMSO solvent was enhanced. This enhancement is evident from the reduced contact angles observed on the coated surface compared to pristine PEDOT:PSS.[255]

Inorganic nickel oxide (NiO_x) is a promising candidate for use as HTL in PeLEDs, owing to its highly favorable characteristics, including exceptional stability, high hole mobility, and effective electron-blocking ability.[256–258] Nonetheless, the issue of nonradiative recombination leading to substantial PL quenching, primarily attributed to charge transfer events induced by defects occurring at the surface of the NiO_x layer, has been a challenge. To avoid these quenching effects, an intermediate layer was strategically introduced between the NiO_x and perovskite film. Sun *et al.* selected PVK as an intermediate layer, which significantly elevated the PLQY from 23% to 54%, resulting in an impressive EQE of 11.2% for a green PeLED.[257] This notable enhancement is attributed to improved hole injection facilitated by the ladder energy band alignment of the NiO_x/PVK layer and the suppression of nonradiative recombination processes, as depicted in Fig. 13b. The incorporation of this intermediate layer not only eliminates PL quenching but also enhances the crystallinity and overall stability of PeLEDs. Additionally, a synergistic approach involving the use of sodium dodecyl sulfate (SDS)-coated NiO_x in combination with short oxygen plasma treatment has been successful in improving the crystallinity of the perovskite layer and facilitating hole injection efficiency.[258] This strategy effectively suppressed quenching by leveraging the interaction between the C═O group in SDS-OP and uncoordinated Pb^{2+}, leading to efficient passivation of interfacial defects. The interfacial properties of SDS-OP contribute to the formation of a substantial surface dipole, a consequence of the combined effects of SDS layer dipoles and the increased concentration of Ni^{3+} species, ultimately resulting in an enhanced hole injection efficiency. Furthermore, a novel NiO_x/LiF (1 nm)/perovskite interface has demonstrated superior wettability toward hydrophilic perovskite precursors and has successfully mitigated the effects of defect trap states on the NiO_x surface.[256]

To enhance the perovskite film morphology and device stability, it is common practice to introduce ultrathin hydrophilic layers on poorly wetted bottom surfaces. You *et al.* employed this approach by depositing a hydrophilic insulating polyvinyl pyrrolidone (PVP) polymer interface layer on the ZnO ETL, leading to a vast reduction in perovskite film pinhole density.[209] The improved wetting of the perovskite precursor solution on the PVP-modified substrate resulted in the uniform growth of perovskite films, thereby minimizing nonradiative recombination at the grain boundaries. Additionally, PVP passivated the surface defects in ZnO, reduced the electron-injection barrier, which, together with its insulating properties, ultimately improved the carrier balance. Similarly, inserting PMMA between the ZnO and $MAPbBr_3$ interface effectively mitigated leakage current and minimized nonradiative recombination pathways.[259] The ZnO substrate catalyzed an *in situ* amidation reaction with the dicarboxylic acids in the precursor, leading to the removal of organic components from the perovskite layer.[260] These newly formed amides acted as interface barriers, preventing undesirable reactions between the perovskite layer and the underlying interface, ensuring stable contact at interface, and contributing to the overall stability of the devices (T_{50} = 682 h at 20 mA cm^{-2}).

In PeLED devices, the extended diffusion length of LHP can lead to an imbalanced charge carrier transport, resulting in charge accumulation near the EML layer. In addition, the interface between the HTL and EML layers plays a crucial role in perovskite crystallization,[261] emphasizing its significance. Various techniques similar to those employed for interface passivation are available to address the issues of the formation of defects. For instance, these techniques include introducing betaine as a passivating agent between the HTL and EML layers[262] or using $MAPbCl_3$ as an HTL layer to passivate defects at the interface.[263] When designing the HTL/EML interface, considerations extend beyond defect reduction. Inserting nanostructures[264] or Al_2O_3 [265] can also be considered to adjust the refractive index mismatch between the EML layer and substrate. This adjustment minimizes the photon losses in the waveguide and substrate modes, thereby maximizing the light outcoupling efficiency.

Upper interface passivation. Owing to the inherent structural softness of the perovskite lattice, the interactions between Pb^{2+} and X-site ions can be relatively weak, rendering the perovskite vulnerable to the formation of ionic surface defects during LHP deposition. Consequently, establishing an upper surface interface layer is an essential prerequisite for defect mitigation. This strategic insertion effectively neutralizes uncoordinated Pb atoms that contribute to nonradiative recombination centers while also reducing the presence of dangling bonds on the surface. Various amine-based passivating interlayers, including branched polyethylenimine (PEI) and EDA with different molecular sizes, were introduced to passivate defect sites in $MAPbBr_3$ thin films, fabricating a highly efficient PeLEDs with excellent stability.[77] This treatment addresses the defect sites by forming coordinated bonds between the nitrogen atoms from the amine-based molecules and the undercoordinated lead ions, leading to charge neutralization and a consequent decrease in the number of defect sites. Compared with PEI, a smaller EDA exhibited superior passivation effects on the top of film surface and penetrated deeper (Fig. 13c). Therefore, Song *et al.* gained outstanding PL intensity, no PL blinking, and enhanced device performance. A thin passivation layer of the organic small molecule TOPO was applied to coat the surface of quasi-two-dimensional perovskite thin films.[266] PeLEDs utilizing $PEA_2(FAPbBr_3)_{n-1}PbBr_4$ (n = 3) exhibited green emission and achieved a remarkable CE of 62.4 cd A^{-1} and an EQE of 14.36%. This achievement primarily relies on the combination of TOPO and $PbBr_2$ to passivate defects, effectively reducing nonradiative recombination at both the surface and grain boundaries. Similarly, the incorporation of a LiF interlayer on the EML/ETL surface served a dual purpose: it eradicated defects at perovskite grain boundaries and the surface by strengthening chemical bonds with uncoordinated Pb^{2+} ions, while also preventing perovskite emission quenching caused by the electron transport layer.[267] Moreover, it reduces excessive electron injection, effectively maintaining carrier balance within the device.

4.3 Adjustment of drive modes

PeLEDs are typically driven by direct current (DC), which is a straightforward driving mode to realize effective luminescence. Nevertheless, DC driving comes into being continuous unidirectional current injection, resulting in unfavorable charge accumulation at the luminescent layers, especially at high current densities.[268] This can compromise the device stability and induce adverse defect behaviors such as ion migration under EFs. In addition, DC driving requires power converters and rectifiers when connected to household alternating current (AC) power lines (110/220 V and 50/60 Hz), making inevitable power losses.[269] Recently, there has been a growing interest in AC-driven EL devices, as they present a potential alternative mode to replace DC driving. AC driving involves the frequent reversal of the applied EF, effectively preventing charge accumulation and thermal degradation of devices, alleviating adverse defect behaviors and improving operational stability.[270–272] The passivation methods discussed earlier, which address defects in NCs and thin films, are not only effective in reducing the defect impact under EF conditions, but also serve as universal defect passivation strategies applicable to devices in various scenarios. AC-driven devices leverage EFs to manage the defect behavior within perovskite materials. When subjected to an AC EF, defects at interfaces or within the EML become activated as charges.[268] These charges, acting as hot electrons, tunnel into the EML to impact and excite emitting centers for light generation or form excitons with counter charges, ultimately in turn leading to light emission through recombination.[268]

Under a DC bias, one detrimental defect behavior is ion migration, which can lead to spectral instability. However, AC driving mode effectively alleviated this issue. Tang *et al.* employed square-wave alternating voltage to drive devices and obtain stable ultra-pure $CsPbBr_xCl_{3-x}$ blue PeLEDs (~466 nm).[273] Under DC operational bias, the mixed-halide perovskite film exhibited Cl-rich and Br-rich regions, resulting in spectral instability due to halide ion migration. This phenomenon was fully reversible upon resetting or applying a reverse bias (Fig. 13d). Utilizing reverse bias facilitates the rearrangement of halogen ions in mixed-halide devices. A square-wave alternating voltage was employed for 12 h to stabilize the EL spectra during the operation. Mobile ions accumulate at the surface of the perovskite emission layer induced by EF, which causes bond bending. This effect reduces the injection barriers for electrons and holes at forward and reverse voltages, enabling bidirectional AC EL. Hu *et al.* realized bidirectional AC EL using red quasi-2D $PEA_2MA_{n-1}Pb_nI_{3n+1}$ films with different *n*-phase uniform distributions and symmetric device structures (ITO/PEDOT:PSS/PEI/$PEA_2MA_{n-1}Pb_nI_{3n+1}$/P3HT/PEI/Ag).[274] The distinct *n*-phase quasi-2D films provided varying optical bandgaps and energy levels of the conduction and valence bands to accept and transport injected carriers. Additionally, the accumulation of mobile ions at the film interface further reduces the energy barriers for carrier injection under AC voltage, enabling bidirectional electron–hole injection. This approach achieved a final EQE of 12.5% and EL irradiance of 24 W sr^{-1} m^{-2} at forward voltage and 3.7% and 18.3 W sr^{-1} m^{-2} at reverse voltage.

Under the influence of EF, both mobile defects and charge carriers exhibit response times to EF, which becomes more pronounced under AC EFs, especially with varying frequencies. In the context of the AC quasi-2D devices mentioned previously, the EL displayed a gradual response when subjected to a square-wave voltage, instantly disappearing when the voltage was removed (Fig. 14a). Moreover, at different frequencies (1/20/50/100 Hz), the response time lengthened with increasing frequency, indicating increased accumulation of mobile ions at the interfaces.[274] Material properties also play a role in the response times. Fig. 14b illustrates that the EL response curves of $MAPbBr_3$ and $MAPbI_3$ under low-frequency and high-frequency AC sinusoidal voltage differ.[275] Under low-frequency conditions, both the $MAPbBr_3$ and $MAPbI_3$ EL responses synchronize with the applied voltage crests. However, at high frequencies, a certain delay is observed because the transit time of the charge carriers exceeds the duration of a forward-bias half-cycle, requiring more time for recombination. The delay effect is more pronounced in $MAPbBr_3$ because the recombination region is closer to the ETL under positive EFs, necessitating a longer receding time under reverse bias to retract the recombination region. Moreover, the ambipolar nature of the materials affects the reverse-bias EL intensity. For ambipolar materials such as $MAPbI_3$, the reverse bias EL intensity is higher because the emission during the negative half-cycle primarily originates from residual charge carriers from the positive half-cycle.

Several efforts have been made to operate PeLEDs using AC voltage, with a focus on reducing the migration of ionic vacancies to enhance operational stability and increase EL intensity. Li and colleagues conducted a comparative study on $CsPbI_3$ NCs under both DC and AC driving modes, observing alleviated efficiency roll-off and improved operational stability under AC mode (Fig. 14c).[271] This effect primarily stemmed from the shorter operation time of AC driving compared with DC driving at an equivalent voltage, mitigating heat generation at high current densities. The frequent EF reversal also contributed to reducing charge accumulation in the defect states. Furthermore, they conducted a comparative analysis between sine and square pulsed bias to assess their effects on enhancing the device stability (Fig. 14d). It was observed that square pulsed bias yielded better EL intensity and operational stability due to the higher voltage magnitude of the square pulsed bias under the same peak-to-peak voltage (V_{PP}).[276] The EL intensity, whether driven by a sine or square pulsed bias, decreases with increasing frequency. This phenomenon can be attributed to the fact that the reverse voltage pumps out a larger number of

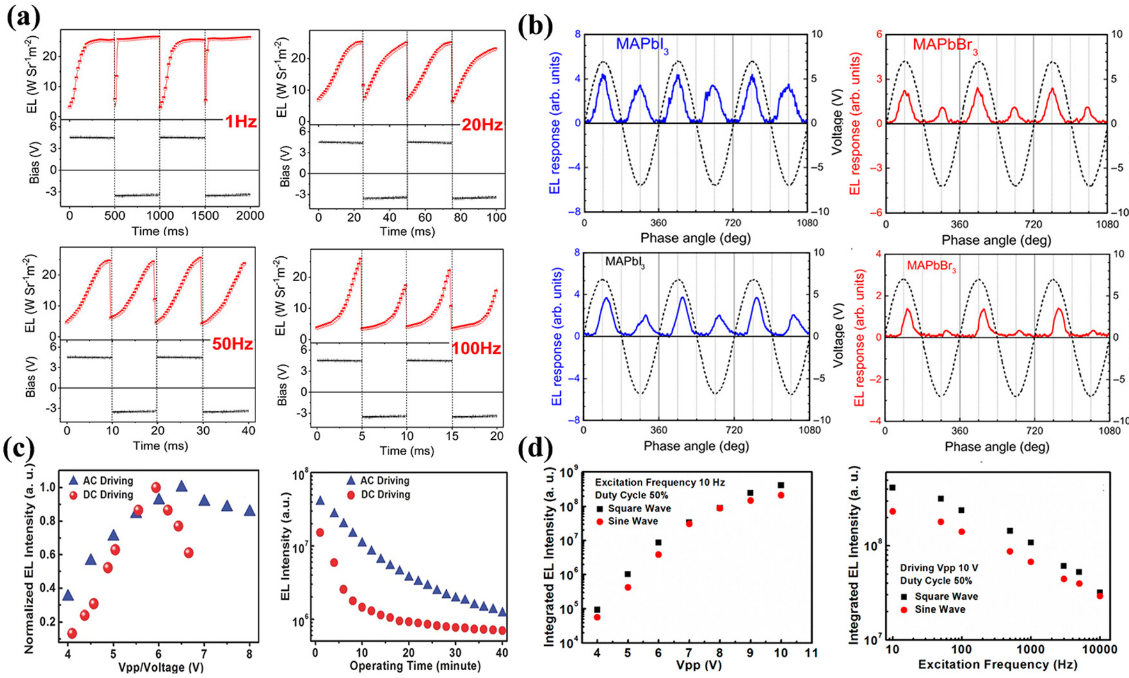

Fig. 14 (a) EL profile of quasi-2D perovskite LEDs under forward (4.5 V) and reverse (−3.5 V) square-wave biases at different frequencies. Reproduced with permission from ref. 274. Copyright 2021 Elsevier Ltd. (b) EL and applied sinusoidal ac voltage as a function of phase angle for the LEDs based on $MAPbI_3$ and $MAPbBr_3$ at 75 Hz (top) or 5.6 kHz (bottom). Reproduced with permission from ref. 275. Copyright 2020 American Physical Society. (c) Normalized EL intensity of $CsPbBr_3$ NCs LED as a function of voltage (left) and running time (right) under DC and AC driving conditions. Reproduced with permission from ref. 271. Copyright 2017 Wiley-VCH. (d) Integrated EL intensity *versus* V_{pp} (left) and excitation frequency (right) under different driving voltage modes (square wave and sine wave). Reproduced with permission from ref. 276. Copyright 2018 MDPI.

injected carriers before they can recombine at higher frequencies. By employing a dual strategy of AC driving and ChCl interface passivation, it is possible to effectively passivate interface defects, suppress device heating, and reduce charge accumulation. As a result, stability is improved by a factor of four compared to DC driving.[277]

We recognize the inherent advantages of perovskite materials, including their high carrier mobility (ranging from 0.1 to 10 cm^2 V^{-1} s^{-1}) and long diffusion lengths (exceeding 500 nm). These properties enable low-frequency emissions when subjected to an AC EF and potential integration with household circuits. Moreover, in AC-OLEDs, the serial connection of multiple units capitalizes on the alternating nature of the AC voltage, facilitating the alternating emission of different colors during the positive and negative cycles. Implementing this approach in PeLEDs broadens the scope of the potential applications of these devices. When operated under a DC bias, thermal effects and the accumulation of defects at interfaces can result in device and material degradation. However, AC driving offers a solution to mitigate these issues, allowing for controlled management of defect behaviors.

5. Conclusion and future perspectives

In recent years, LHP materials have achieved remarkable advancements, which are emerging as promising candidates for next-generation display technologies. LHP materials exhibit notable advantages such as high EQE, cost-effective fabrication, exceptional color purity, and an extensive color gamut. Although research into the physics of LHP-based devices is currently experiencing rapid growth, there remains a substantial gap that must be bridged before commercial applications can be fully realized. LHPs are well known for their high tolerance to defects; however, recent investigations have indicated that defects play a pivotal role in constraining the attainment of high-performance PeLEDs. Therefore, our focus was on elucidating the behavior of defects and providing a comprehensive review of defect passivation methods.

The formation of defects in PNCs and bulk films is influenced by a variety of internal and external factors. Among these factors, the study of defect behavior under EF is particularly pivotal, as an EF serves as an indispensable external operating condition for driving these devices. The behavior of defects in the presence of EF remains intricate and elusive. Under EF, defects undergo transformation into charged defects, leading to the movement of quasi-free charge carriers and ensuing ion migration. Ion migration, as a consequence of defect behavior, is particularly concerning for researchers due to its potential to cause device degradation and introduce color impurities. However, these adverse effects can be effectively mitigated through the application of targeted defect passivation techniques. A more profound understanding of the EF-induced defect dynamics behavior is still relatively limited.

When devices inject or generate charge carriers or photocarriers under the influence of EF or illumination, the interaction between defects and carriers becomes notably intricate. Currently, PL variation serves as the primary tool for investigating the behavior of charge carriers and defects in the presence of lateral EF. Additionally, the movement of defects under an electric field can generate new, potentially harmful deep-level defects.

The challenge in achieving theoretical unity in understanding defect behaviors is partly due to the absence of direct visual characterization methods for defects. Although commonly used methods, such as microscopy, spectroscopy, and electrical measurements, have been reported in the literature, these methods primarily provide indirect responses to defect behaviors, which is not conducive to simple analysis. TOF-SIMS, a technique enabling the relative visualization of ion migration phenomena within devices, and a number of developed *in situ* characterization techniques provide valuable insights into how defect behaviors contribute to poor device performance.

Nowadays, extensive research is directed toward defect passivation with the aim of mitigating the adverse effects of defect behaviors and enhancing the performance of PeLEDs. In this review, we summarized the recent advancements in defect passivation within LHPs and examined them from three perspectives: NCs, bulk films, and driving methods. Defect passivation for NCs predominantly revolves around ligand control, which we have delineated with a focus on functional groups for optimizing both NC materials and devices. However, the choice of ligands for NCs creates problems of possible toxicity and stability, restricting their development. The commonly used encapsulation method increases the particle size, which is unfavorable for practical applications. Natural materials such as lecithin as a ligand are a potential material to expand the application of NCs in the biological field. Regarding the defect passivation methods for bulk films, we explored compositional adjustments, solvent engineering, annealing processes, additive engineering, and interface passivation. Current research has shown that using inorganic additives in bulk materials is cost-effective, suitable for mass production, and commercially viable. Furthermore, employing AC-EF that can be directly integrated with home circuits to drive PeLEDs presents a feasible approach and constitutes an important research target for future commercial applications.

Looking ahead, EF-induced LHP-based devices are ripe with opportunities and challenges. Research on EF-induced defect behavior primarily centers on the lateral EF, with limited exploration of vertical electric fields. In-depth research into the impact of vertical EFs on defect behavior is crucial, a topic that currently lacks consensus within the academic community. This highlights a significant research gap that demands to be addressed urgently and requires a concerted effort by researchers in their future work. This is not just vital for understanding the physics of the PeLEDs but also pivotal in eliminating the effects of ion migration, an essential step towards the early realization of commercial use.

Moreover, due to the toxicity concerns associated with lead in LHPs, there has been a growing focus on developing lead-free perovskites. Lead is highly water soluble and readily cycles through the food chain into the human body. Therefore, to safeguard public health, it is imperative for us to pursue the development of Pb-free PeLEDs vigorously, but the performance of current Pb-free devices still significantly lags far behind that of Pb-based perovskite because of self-trapped exciton emission and indirect bandgap. With vigorous development, non-toxic or low-toxicity Sn- or Ge-based PeLEDs are expected to improve performance gradually.

AC is emerging as a promising solution for mitigating the charge accumulation at interfaces induced by EFs. PeLEDs driven by AC can be directly connected to standard household circuits (110/220 V and 50/60 Hz) without additional power converters and rectifiers, reducing power loss. AC driving mode has the potential to achieve color-tunable emission, akin to OLEDs, under varying EF directions, fulfilling the desire for adjustable color displays. Therefore, AC driving is poised to become a significant research focus in the field of PeLEDs.

Author contributions

S. Z. and Z. X. conceived and designed the project. N. J. carried out research on the literature and drafted an initial version of the review. G. M. supported literature collection. All authors discussed the results and assisted during manuscript preparation.

Conflicts of interest

The authors declare no conflict of interest.

Acknowledgements

The authors express their thanks to the National Key Research and Development Program of China under grant no. 2021YFB3600403 and the National Natural Science Foundation of China under grant no. 62075006.

References

1 J. Wang, S. Wang, Y. Zhou, Y. Lou and Z. Wang, *Sci. China Mater.*, 2022, **66**, 1–21.
2 Z. Ren, K. Wang, X. W. Sun and W. C. H. Choy, *Adv. Funct. Mater.*, 2021, **31**, 2100516.
3 Y. Gao, X. Li, W. Liu, X. Xing, H. Long, K. Wang, B. Wang and P. Lu, *Nano Lett.*, 2021, **21**, 10230–10237.
4 J. Lu, C. Yan, W. Feng, X. Guan, K. Lin and Z. Wei, *EcoMat*, 2021, **3**, e12082.
5 X. K. Liu, W. Xu, S. Bai, Y. Jin, J. Wang, R. H. Friend and F. Gao, *Nat. Mater.*, 2021, **20**, 10–21.

6 H. He, S. Mei, Z. Wen, D. Yang, B. Yang, W. Zhang, F. Xie, G. Xing and R. Guo, *Small*, 2022, **18**, e2103527.

7 Y. Xia, Y. Lou, Y. Zhou, K. Wang, J. Chen, Z. Wang and L. Liao, *J. Mater. Chem. C*, 2022, **10**, 3276–3286.

8 L. Xu, S. Yuan, H. Zeng and J. Song, *Mater. Today Nano*, 2019, **6**, 100036.

9 Z. Tan, R. S. Moghaddam, M. L. Lai, P. Docampo, R. Higler, F. Deschler, M. Price, A. Sadhanala, L. M. Pazos, D. Credgington, F. Hanusch, T. Bein, H. J. Snaith and R. H. Friend, *Nat. Nanotechnol.*, 2014, **9**, 687–692.

10 K. Wang, Z. Y. Lin, Z. Zhang, L. Jin, K. Ma, A. H. Coffey, H. R. Atapattu, Y. Gao, J. Y. Park, Z. Wei, B. P. Finkenauer, C. Zhu, X. Meng, S. N. Chowdhury, Z. Chen, T. Terlier, T. H. Do, Y. Yao, K. R. Graham, A. Boltasseva, T. F. Guo, L. Huang, H. Gao, B. M. Savoie and L. Dou, *Nat. Commun.*, 2023, **14**, 397.

11 W. Bai, T. Xuan, H. Zhao, H. Dong, X. Cheng, L. Wang and R. J. Xie, *Adv. Mater.*, 2023, **35**, e2302283.

12 W. Zhou, Y. Shen, L. X. Cao, Y. Lu, Y. Y. Tang, K. Zhang, H. Ren, F. M. Xie, Y. Q. Li and J. X. Tang, *Adv. Funct. Mater.*, 2023, **33**, 2301425.

13 J. Ye, M. M. Byranvand, C. O. Martinez, R. L. Z. Hoye, M. Saliba and L. Polavarapu, *Angew. Chem., Int. Ed.*, 2021, **60**, 21636–21660.

14 W. Tress, *Adv. Energy Mater.*, 2017, **7**, 1602358.

15 M. Azam, K. Liu, Y. Sun, Z. Wang, G. Liang, S. Qu, P. Fan and Z. Wang, *J. Phys. D: Appl. Phys.*, 2020, **53**, 183002.

16 W. Li, M. U. Rothmann, Y. Zhu, W. Chen, C. Yang, Y. Yuan, Y. Y. Choo, X. Wen, Y. Cheng, U. Bach and J. Etheridge, *Nat. Energy*, 2021, **6**, 624–632.

17 H. Kim, J. S. Kim, J. M. Heo, M. Pei, I. H. Park, Z. Liu, H. J. Yun, M. H. Park, S. H. Jeong, Y. H. Kim, J. W. Park, E. Oveisi, S. Nagane, A. Sadhanala, L. Zhang, J. J. Kweon, S. K. Lee, H. Yang, H. M. Jang, R. H. Friend, K. P. Loh, M. K. Nazeeruddin, N. G. Park and T. W. Lee, *Nat. Commun.*, 2020, **11**, 3378.

18 S. Wieghold, E. M. Cope, G. Moller, N. Shirato, B. Guzelturk, V. Rose and L. Nienhaus, *ACS Energy Lett.*, 2022, **7**, 2211–2218.

19 D. Ji, M. Na, S. Wang, H. Zhang, K. Zhu, C. Zhang and X. Li, *Sci. Rep.*, 2018, **8**, 12492.

20 T. Leijtens, A. R. S. Kandada, G. E. Eperon, G. Grancini, V. D'Innocenzo, J. M. Ball, S. D. Stranks, H. J. Snaith and A. Petrozza, *J. Am. Chem. Soc.*, 2015, **137**, 15451–15459.

21 S. T. Birkhold, J. T. Precht, H. Liu, R. Giridharagopal, G. E. Eperon, L. Schmidt-Mende, X. Li and D. S. Ginger, *ACS Energy Lett.*, 2018, **3**, 1279–1286.

22 Y. Zhong, K. Liao, W. Du, J. Zhu, Q. Shang, F. Zhou, X. Wu, X. Sui, J. Shi, S. Yue, Q. Wang, Y. Zhang, Q. Zhang, X. Hu and X. Liu, *ACS Nano*, 2020, **14**, 15605–15615.

23 M. A. Green, A. Ho-Baillie and H. J. Snaith, *Nat. Photonics*, 2014, **8**, 506–514.

24 M. Ju, J. Dai, L. Ma and X. Zeng, *J. Am. Chem. Soc.*, 2017, **139**, 8038–8043.

25 C. Li, X. Lu, W. Ding, L. Feng, Y. Gao and Z. Guo, *Acta Crystallogr., Sect. B: Struct. Sci.*, 2008, **64**, 702–707.

26 C. J. Bartel, C. Sutton, B. R. Goldsmith, R. Ouyang, C. B. Musgrave, L. M. Ghiringhelli and M. Scheffler, *Sci. Adv.*, 2019, **5**, eaav0693.

27 J. Kang, J. Li and S. Wei, *Appl. Phys. Rev.*, 2021, **8**, 031302.

28 X. Zhang, J. X. Shen, M. E. Turiansky and C. G. Van de Walle, *Nat. Mater.*, 2021, **20**, 971–976.

29 S. N. Habisreutinger, T. Leijtens, G. E. Eperon, S. D. Stranks, R. J. Nicholas and H. J. Snaith, *Nano Lett.*, 2014, **14**, 5561–5568.

30 X. Ma and Z. Li, *Appl. Surf. Sci.*, 2018, **428**, 140–147.

31 J. You, Y. Yang, Z. Hong, T. B. Song, L. Meng, Y. Liu, C. Jiang, H. Zhou, W. H. Chang, G. Li and Y. Yang, *Appl. Phys. Lett.*, 2014, **105**, 183902.

32 S. Chen, X. Wen, S. Huang, F. Huang, Y. Cheng, M. Green and A. Ho-Baillie, *Sol. RRL*, 2017, **1**, 1600001.

33 K. Suchan, J. Just, P. Beblo, C. Rehermann, A. Merdasa, R. Mainz, I. G. Scheblykin and E. Unger, *Adv. Funct. Mater.*, 2022, **33**, 2206047.

34 S. J. Yoon, M. Kuno and P. V. Kamat, *ACS Energy Lett.*, 2017, **2**, 1507–1514.

35 X. Bu, R. J. E. Westbrook, L. Lanzetta, D. Ding, T. Chotchuangchutchaval, N. Aristidou and S. A. Haque, *Sol. RRL*, 2019, **3**, 1800282.

36 K. S. Cho, E. K. Lee, W. J. Joo, E. Jang, T. H. Kim, S. J. Lee, S. J. Kwon, J. Y. Han, B. K. Kim, B. L. Choi and J. M. Kim, *Nat. Photonics*, 2009, **3**, 341–345.

37 Y. Zou, T. Wu, F. Fu, S. Bai, L. Cai, Z. Yuan, Y. Li, R. Li, W. Xu, T. Song, Y. Yang, X. Gao, F. Gao and B. Sun, *J. Mater. Chem. C*, 2020, **8**, 15079–15085.

38 M. I. Cohen, K. F. Young, T. T. Chang and W. S. Brower, *J. Appl. Phys.*, 1971, **42**, 5267–5272.

39 D. Zhang, S. W. Eaton, Y. Yu, L. Dou and P. Yang, *J. Am. Chem. Soc.*, 2015, **137**, 9230–9233.

40 K. Gesi and K. Ozawa, *J. Phys. Soc. Jpn.*, 1975, **39**, 1026–1031.

41 T. Hu, D. Li, Q. Shan, Y. Dong, H. Xiang, W. C. H. Choy and H. Zeng, *ACS Mater. Lett.*, 2021, **3**, 1702–1728.

42 F. Brivio, J. M. Frost, J. M. Skelton, A. J. Jackson, O. J. Weber, M. T. Weller, A. R. Goni, M. A. Leguy, P. R. F. Barnes and A. Walsh, *Phys. Rev. B: Condens. Matter Mater. Phys.*, 2015, **92**, 144308.

43 J. Wu, Y. Li, S. Tan, B. Yu, H. Li, Y. Li, J. Shi, H. Wu, Y. Luo, D. Li and Q. Meng, *ACS Appl. Mater. Interfaces*, 2020, **12**, 27258–27267.

44 N. Li, Y. Jia, Y. Guo and N. Zhao, *Adv. Mater.*, 2022, **34**, e2108102.

45 Y. Yuan and J. Huang, *Acc. Chem. Res.*, 2016, **49**, 286–293.

46 Q. A. Akkerman, G. Raino, M. V. Kovalenko and L. Manna, *Nat. Mater.*, 2018, **17**, 394–405.

47 X. Liu, Z. Yu, T. Wang, K. L. Chiu, F. Lin, H. Gong, L. Ding and Y. Cheng, *Adv. Energy Mater.*, 2020, **10**, 2001958.

48 H. Cheng, Y. Feng, Y. Fu, Y. Zheng, Y. Shao and Y. Bai, *J. Mater. Chem. C*, 2022, **10**, 13590–13610.

49 C. G. Bischak, E. M. Sanehira, J. T. Precht, J. M. Luther and N. S. Ginsberg, *Nano Lett.*, 2015, **15**, 4799–4807.

50 D. W. D. Quilettes, S. M. Vorpahl, S. D. Stranks, H. Nagaoka, G. E. Eperon, M. E. Ziffer, H. J. Snaith and D. S. Ginger, *Science*, 2015, **348**, 683–686.

51 J. S. Yun, A. Ho-Baillie, S. Huang, S. H. Woo, Y. Heo, J. Seidel, F. Huang, Y. Cheng and M. A. Green, *J. Phys. Chem. Lett.*, 2015, **6**, 875–880.

52 N. Faraji, C. Qin, T. Matsushima, C. Adachi and J. Seidel, *J. Phys. Chem. C*, 2018, **122**, 4817–4821.

53 Z. Kang, H. Si, M. Shi, C. Xu, W. Fan, S. Ma, A. Kausar, Q. Liao, Z. Zhang and Y. Zhang, *Sci. China Mater.*, 2019, **62**, 776–789.

54 J. S. Yun, J. Seidel, J. Kim, A. M. Soufiani, S. Huang, J. Lau, N. J. Jeon, S. I. Seok, M. A. Green and A. Ho-Baillie, *Adv. Energy Mater.*, 2016, **6**, 1600330.

55 L. K. Ono and Y. Qi, *J. Phys. Chem. Lett.*, 2016, **7**, 4764–4794.

56 S. Lee, D. B. Kim, J. C. Yu, C. H. Jang, J. H. Park, B. R. Lee and M. H. Song, *Adv. Mater.*, 2019, **31**, e1805244.

57 C. Stecker, K. Liu, J. Hieulle, R. Ohmann, Z. Liu, L. K. Ono, G. Wang and Y. Qi, *ACS Nano*, 2019, **13**, 12127–12136.

58 X. Ren, X. Zhang, H. Xie, J. Cai, C. Wang, E. Chen, S. Xu, Y. Ye, J. Sun, Q. Yan and T. Guo, *Nanomaterials*, 2022, **12**, 2243.

59 J. Song, J. Li, L. Xu, J. Li, F. Zhang, B. Han, Q. Shan and H. Zeng, *Adv. Mater.*, 2018, **30**, e1800764.

60 F. Qin, M. Lu, P. Lu, S. Sun, X. Bai and Y. Zhang, *Small Methods*, 2023, **7**, e2300434.

61 Y. Jiang, M. Cui, S. Li, C. Sun, Y. Huang, J. Wei, L. Zhang, M. Lv, C. Qin, Y. Liu and M. Yuan, *Nat. Commun.*, 2021, **12**, 336.

62 Z. L. Tseng, L. C. Chen, L. W. Chao, M. J. Tsai, D. Luo, N. R. A. Amin, S. W. Liu and K. T. Wong, *Adv. Mater.*, 2022, **34**, e2109785.

63 D. Cao, W. Li, X. Zhang, L. Wan, Z. Guo, X. Wang, D. Eder and S. Wang, *J. Mater. Chem. A*, 2022, **10**, 19278–19303.

64 J. Hidalgo, A. F. Castro-Méndez and J. P. Correa-Baena, *Adv. Energy Mater.*, 2019, **9**, 1900444.

65 Q. Huang, Y. Zou, S. A. Bourelle, T. Zhai, T. Wu, Y. Tan, Y. Li, J. Li, S. Duhm, T. Song, L. Wang, F. Deschler and B. Sun, *Nanoscale Horiz.*, 2019, **4**, 924–932.

66 H. S. Duan, H. Zhou, Q. Chen, P. Sun, S. Luo, T. B. Song, B. Bob and Y. Yang, *Phys. Chem. Chem. Phys.*, 2015, **17**, 112–116.

67 T. Walter, R. Herberholz, C. Müller and H. W. Schock, *J. Appl. Phys.*, 1996, **80**, 4411–4420.

68 X. Zheng, B. Chen, J. Dai, Y. Fang, Y. Bai, Y. Lin, H. Wei, X. Zeng and J. Huang, *Nat. Energy*, 2017, **2**, 17102.

69 S. Heo, G. Seo, Y. Lee, D. Lee, M. Seol, J. Lee, J. B. Park, K. Kim, D. J. Yun, Y. S. Kim, J. K. Shin, T. K. Ahn and M. K. Nazeeruddin, *Energy Environ. Sci.*, 2017, **10**, 1128–1133.

70 L. Xu, G. Liu, H. Xiang, R. Wang, Q. Shan, S. Yuan, B. Cai, Z. Li, W. Li, S. Zhang and H. Zeng, *Appl. Phys. Rev.*, 2022, **9**, 021308.

71 I. Zarazua, J. Bisquert and G. Garcia-Belmonte, *J. Phys. Chem. Lett.*, 2016, **7**, 525–528.

72 M. Xu, Q. Peng, W. Zou, L. Gu, L. Xu, L. Cheng, Y. He, M. Yang, N. Wang, W. Huang and J. Wang, *Appl. Phys. Lett.*, 2019, **115**, 041102.

73 G. G. Malliaras, J. R. Salem, P. J. Brock and J. C. Scott, *Phys. Rev. B: Condens. Matter Mater. Phys.*, 1999, **59**, 10371.

74 D. Shi, V. Adinolfi, R. Comin, M. Yuan, E. Alarousu, A. Buin, Y. Chen, S. Hoogland, A. Rothenberger, K. Katsiv, Y. Losovyj, X. Zhang, P. A. Dowben, O. F. Mohammed, E. H. Sargent and O. M. Bakr, *Science*, 2015, **347**, 519–522.

75 Y. Yang, X. Peng, C. Qin, Y. Lian, J. Gao and X. Yang, *ACS Photonics*, 2022, **9**, 163–172.

76 S. P. Harvey, J. Messinger, K. Zhu, J. M. Luther and J. J. Berry, *Adv. Energy Mater.*, 2020, **10**, 1903674.

77 S. Lee, J. H. Park, B. R. Lee, E. D. Jung, J. C. Yu, D. Di Nuzzo, R. H. Friend and M. H. Song, *J. Phys. Chem. Lett.*, 2017, **8**, 1784–1792.

78 Q. Jeangros, M. Duchamp, J. Werner, M. Kruth, R. E. Dunin-Borkowski, B. Niesen, C. Ballif and A. Hessler-Wyser, *Nano Lett.*, 2016, **16**, 7013–7018.

79 H. Hu, Z. Ren, P. W. K. Fong, M. Qin, D. Liu, D. Lei, X. Lu and G. Li, *Adv. Funct. Mater.*, 2019, **29**, 1900092.

80 J. Varignon, N. C. Bristowe and P. Ghosez, *Phys. Rev. Lett.*, 2016, **116**, 057602.

81 X. Deng, X. Wen, C. F. J. Lau, T. Young, J. Yun, M. A. Green, S. Huang and A. W. Y. Ho-Baillie, *J. Mater. Chem. C*, 2016, **4**, 9060–9068.

82 L. Kong, X. Zhang, C. Zhang, L. Wang, S. Wang, F. Cao, D. Zhao, A. L. Rogach and X. Yang, *Adv. Mater.*, 2022, **34**, e2205217.

83 T. Y. Yang, G. Gregori, N. Pellet, M. Gratzel and J. Maier, *Angew. Chem.*, 2015, **127**, 8016–8021.

84 Z. Xiao, Y. Yuan, Y. Shao, Q. Wang, Q. Dong, C. Bi, P. Sharma, A. Gruverman and J. Huang, *Nat. Mater.*, 2015, **14**, 193–198.

85 Y. Lin, B. Chen, Y. Fang, J. Zhao, C. Bao, Z. Yu, Y. Deng, P. N. Rudd, Y. Yan, Y. Yuan and J. Huang, *Nat. Commun.*, 2018, **9**, 4981.

86 S. Reichert, J. Flemming, Q. An, Y. Vaynzof, J. F. Pietschmann and C. Deibel, *Phys. Rev. Appl.*, 2020, **13**, 034018.

87 M. H. Futscher, J. M. Lee, L. McGovern, L. A. Muscarella, T. Wang, M. I. Haider, A. Fakharuddin, L. Schmidt-Mende and B. Ehrler, *Mater. Horiz.*, 2019, **6**, 1497–1503.

88 Y. Chen, N. Li, L. Wang, L. Li, Z. Xu, H. Jiao, P. Liu, C. Zhu, H. Zai, M. Sun, W. Zou, S. Zhang, G. Xing, X. Liu, J. Wang, D. Li, B. Huang, Q. Chen and H. Zhou, *Nat. Commun.*, 2019, **10**, 1112.

89 E. Mosconi, D. Meggiolaro, H. J. Snaith, S. D. Stranks and F. De Angelis, *Energy Environ. Sci.*, 2016, **9**, 3180–3187.

90 L. Yao, X. Lou, N. Sui, W. Zhang, H. Xiao, X. Chi, H. Zhang, L. Yuan, J. Zhang and Y. Wang, *J. Lumin.*, 2023, **253**, 119444.

91 M. Bag, L. A. Renna, R. Y. Adhikari, S. Karak, F. Liu, P. M. Lahti, T. P. Russell, M. T. Tuominen and

D. Venkataraman, *J. Am. Chem. Soc.*, 2015, **137**, 13130–13137.

92 J. M. Azpiroz, E. Mosconi, J. Bisquert and F. De Angelis, *Energy Environ. Sci.*, 2015, **8**, 2118–2127.

93 C. Eames, J. M. Frost, P. R. F. Barnes, B. C. O'Regan, A. Walsh and M. S. Islam, *Nat. Commun.*, 2015, **6**, 7497.

94 J. Haruyama, K. Sodeyama, L. Han and Y. Tateyama, *J. Am. Chem. Soc.*, 2015, **137**, 10048–10051.

95 P. Delugas, C. Caddeo, A. Filippetti and A. Mattoni, *J. Phys. Chem. Lett.*, 2016, **7**, 2356–2361.

96 S. Meloni, T. Moehl, W. Tress, M. Franckevicius, M. Saliba, Y. H. Lee, P. Gao, M. K. Nazeeruddin, S. M. Zakeeruddin, U. Rothlisberger and M. Graetzel, *Nat. Commun.*, 2016, **7**, 10334.

97 L. Zhao, Y. W. Yeh, N. L. Tran, F. Wu, Z. Xiao, R. A. Kerner, Y. L. Lin, G. D. Scholes, N. Yao and B. P. Rand, *ACS Nano*, 2017, **11**, 3957–3964.

98 Y. Jia, H. Yu, Y. Zhou, N. Li, Y. Guo, F. Xie, Z. Qin, X. Lu and N. Zhao, *ACS Appl. Mater. Interfaces*, 2021, **13**, 28546–28554.

99 B. Yang, C. C. Brown, J. Huang, L. Collins, X. Sang, R. R. Unocic, S. Jesse, S. V. Kalinin, A. Belianinov, J. Jakowski, D. B. Geohegan, B. G. Sumpter, K. Xiao and O. S. Ovchinnikova, *Adv. Funct. Mater.*, 2017, **27**, 1700749.

100 X. Zhu, J. Lee and W. D. Lu, *Adv. Mater.*, 2017, **29**, 1700527.

101 L. Zhao, R. A. Kerner, Z. Xiao, Y. L. Lin, K. M. Lee, J. Schwartz and B. P. Rand, *ACS Energy Lett.*, 2016, **1**, 595–602.

102 X. Wang, Y. Li, Y. Xu, Y. Pan, Y. Wu, G. Li, Q. Huang, Q. Zhang, Q. Li, X. Zhang, J. Chen and W. Lei, *Phys. Status Solidi B*, 2020, **257**, 1900784.

103 R. I. Biega and L. Leppert, *J. Phys.: Energy*, 2021, **3**, 034017.

104 A. Oranskaia, J. Yin, O. M. Bakr, J. L. Bredas and O. F. Mohammed, *J. Phys. Chem. Lett.*, 2018, **9**, 5474–5480.

105 D. Meggiolaro, E. Mosconi and F. De Angelis, *ACS Energy Lett.*, 2019, **4**, 779–785.

106 L. Zhao, J. Gao, Y. L. Lin, Y. W. Yeh, K. M. Lee, N. Yao, Y. L. Loo and B. P. Rand, *Adv. Mater.*, 2017, **29**, 1605317.

107 N. K. Kumawat, W. Tress and F. Gao, *Nat. Commun.*, 2021, **12**, 4899.

108 C. Bi, Z. Yao, X. Sun, X. Wei, J. Wang and J. Tian, *Adv. Mater.*, 2021, **33**, e2006722.

109 J. Yang, Y. Song, J. Yao, K. Wang, J. Wang, B. Zhu, M. Yao, S. U. Rahman, Y. Lan, F. Fan and H. Yao, *J. Am. Chem. Soc.*, 2020, **142**, 2956–2967.

110 P. Vashishtha and J. E. Halpert, *Chem. Mater.*, 2017, **29**, 5965–5973.

111 G. Li, F. W. Rivarola, N. J. L. K. Davis, S. Bai, T. C. Jellicoe, F. de la Pena, S. Hou, C. Ducati, F. Gao, R. H. Friend, N. C. Greenham and Z. Tan, *Adv. Mater.*, 2016, **28**, 3528–3534.

112 T. G. Liashenko, A. P. Pushkarev, A. Naujokaitis, V. Pakstas, M. Franckevicius, A. A. Zakhidov and S. V. Makarov, *Nanomaterials*, 2020, **10**, 1937.

113 Y. Miao, Y. Ke, N. Wang, W. Zou, M. Xu, Y. Cao, Y. Sun, R. Yang, Y. Wang, Y. Tong, W. Xu, L. Zhang, R. Li, J. Li, H. He, Y. Jin, F. Gao, W. Huang and J. Wang, *Nat. Commun.*, 2019, **10**, 3624.

114 H. Wang, F. U. Kosasih, H. Yu, G. Zheng, J. Zhang, G. Pozina, Y. Liu, C. Bao, Z. Hu, X. Liu, L. Kobera, S. Abbrent, J. Brus, Y. Jin, M. Fahlman, R. H. Friend, C. Ducati, X. Liu and F. Gao, *Nat. Commun.*, 2020, **11**, 891.

115 W. Ming, D. Yang, T. Li, L. Zhang and M. H. Du, *Adv. Sci.*, 2018, **5**, 1700662.

116 N. N. Shlenskaya, N. A. Belich, M. Grätzel, E. A. Goodilin and A. B. Tarasov, *J. Mater. Chem. A*, 2018, **6**, 1780–1786.

117 K. Awasthi, C. Wang, A. Fathi, S. Narra, E. W. G. Diau and N. Ohta, *J. Phys. Chem. C*, 2017, **121**, 22700–22706.

118 C. Li, A. Guerrero, S. Huettner and J. Bisquert, *Nat. Commun.*, 2018, **9**, 5113.

119 S. Chen, X. Wen, R. Sheng, S. Huang, X. Deng, M. A. Green and A. Ho-Baillie, *ACS Appl. Mater. Interfaces*, 2016, **8**, 5351–5357.

120 D. L. Jacobs, M. A. Scarpulla, C. Wang, B. R. Bunes and L. Zang, *J. Phys. Chem. C*, 2016, **120**, 7893–7902.

121 Z. Xu, T. De Rosia and K. Weeks, *J. Phys. Chem. C*, 2017, **121**, 24389–24396.

122 J. Xing, C. Zhao, Y. Zou, W. Kong, Z. Yu, Y. Shan, Q. Dong, D. Zhou, W. Yu and C. Guo, *Light: Sci. Appl.*, 2020, **9**, 111.

123 H. T. Yi, S. Rangan, B. Tang, C. D. Frisbie, R. A. Bartynski, Y. N. Gartstein and V. Podzorov, *Mater. Today*, 2019, **28**, 31–39.

124 X. Hu, X. Wang, P. Fan, Y. Li, X. Zhang, Q. Liu, W. Zheng, G. Xu, X. Wang, X. Zhu and A. Pan, *Nano Lett.*, 2018, **18**, 3024–3031.

125 S. Yuan, X. Zheng, W. Shen, J. Liu, L. Cui, C. Zhang, Q. Tian, J. Wu, Y. Zhou, X. Wang, Z. Wang, P. Han, J. M. Luther, O. M. Bakr and L. Liao, *ACS Energy Lett.*, 2022, **7**, 1348–1354.

126 W. Sun, R. Yun, Y. Liu, X. Zhang, M. Yuan, L. Zhang and X. Li, *Small*, 2023, **19**, e2205950.

127 S. ten Brinck and I. Infante, *ACS Energy Lett.*, 2016, **1**, 1266–1272.

128 V. K. Ravi, P. K. Santra, N. Joshi, J. Chugh, S. K. Singh, H. Rensmo, P. Ghosh and A. Nag, *J. Phys. Chem. Lett.*, 2017, **8**, 4988–4994.

129 J. De Roo, M. Ibanez, P. Geiregat, G. Nedelcu, W. Walravens, J. Maes, J. C. Martins, I. Van Driessche, M. V. Kovalenko and Z. Hens, *ACS Nano*, 2016, **10**, 2071–2081.

130 S. R. Smock, T. J. Williams and R. L. Brutchey, *Angew. Chem., Int. Ed.*, 2018, **57**, 11711–11715.

131 G. Almeida, I. Infante and L. Manna, *Science*, 2019, **364**, 833–834.

132 M. I. Bodnarchuk, S. C. Boehme, S. Ten Brinck, C. Bernasconi, Y. Shynkarenko, F. Krieg, R. Widmer, B. Aeschlimann, D. Gunther, M. V. Kovalenko and I. Infante, *ACS Energy Lett.*, 2019, **4**, 63–74.

133 Z. Shen, S. Zhao, D. Song, Z. Xu, B. Qiao, P. Song, Q. Bai, J. Cao, G. Zhang and W. Swelm, *Small*, 2020, **16**, e1907089.

134 Q. Shan, J. Song, Y. Zou, J. Li, L. Xu, J. Xue, Y. Dong, B. Han, J. Chen and H. Zeng, *Small*, 2017, **13**, 1701770.

135 H. Wang, N. Sui, X. Bai, Y. Zhang, Q. Rice, F. J. Seo, Q. Zhang, V. L. Colvin and W. W. Yu, *J. Phys. Chem. Lett.*, 2018, **9**, 4166–4173.

136 H. Wang, X. Zhang, N. Sui, Y. Hu, V. L. Colvin, W. W. Yu and Y. Zhang, *ACS Appl. Mater. Interfaces*, 2020, **12**, 11769–11777.

137 C. Lu, H. Li, K. Kolodziejski, C. Dun, W. Huang, D. Carroll and S. M. Geyer, *Nano Res.*, 2017, **11**, 762–768.

138 F. Liu, Y. Zhang, C. Ding, S. Kobayashi, T. Izuishi, N. Nakazawa, T. Toyoda, T. Ohta, S. Hayase, T. Minemoto, K. Yoshino, S. Dai and Q. Shen, *ACS Nano*, 2017, **11**, 10373–10383.

139 Y. Liu, D. Li, L. Zhang, Y. Chen, C. Geng, S. Shi, Z. Zhang, W. Bi and S. Xu, *Chem. Mater.*, 2020, **32**, 1904–1913.

140 J. Wu, J. Tong, Y. Gao, A. Wang, T. Zhang, H. Tan, S. Nie and Z. Deng, *Angew. Chem., Int. Ed.*, 2020, **59**, 7738–7742.

141 K. H. Peng, S. H. Yang, Z. Y. Wu and H. C. Hsu, *ACS Omega*, 2021, **6**, 10437–10446.

142 E. A. C. Ruiz, D. F. G. Gutierrez and D. I. G. Gutierrez, *Nanotechnology*, 2022, **33**, 155604.

143 L. Wu, Q. Zhong, D. Yang, M. Chen, H. Hu, Q. Pan, H. Liu, M. Cao, Y. Xu, B. Sun and Q. Zhang, *Langmuir*, 2017, **33**, 12689–12696.

144 S. Baek, S. Kang, C. Son, S. J. Shin, J. H. Kim, J. Park and S. W. Kim, *Adv. Opt. Mater.*, 2020, **8**, 1901897.

145 G. Almeida, O. J. Ashton, L. Goldoni, D. Maggioni, U. Petralanda, N. Mishra, Q. A. Akkerman, I. Infante, H. J. Snaith and L. Manna, *J. Am. Chem. Soc.*, 2018, **140**, 14878–14886.

146 N. F. Jamaludin, N. Yantara, B. Febriansyah, Y. B. Tay, B. T. Muhammad, S. Laxmi, S. S. Lim, T. C. Sum, S. Mhaisalkar and N. Mathews, *ACS Energy Lett.*, 2021, **6**, 4265–4272.

147 Y. Zhang, Z. Zhang, W. Yu, Y. He, Z. Chen, L. Xiao, J. Shi, X. Guo, S. Wang and B. Qu, *Adv. Sci.*, 2022, **9**, e2102895.

148 D. Ma, K. Lin, Y. Dong, H. Choubisa, A. H. Proppe, D. Wu, Y. Wang, B. Chen, P. Li, J. Z. Fan, F. Yuan, A. Johnston, Y. Liu, Y. Kang, Z. Lu, Z. Wei and E. H. Sargent, *Nature*, 2021, **599**, 594–598.

149 K. Hills-Kimball, H. Yang, T. Cai, J. Wang and O. Chen, *Adv. Sci.*, 2021, **8**, 2100214.

150 Y. Tan, Y. Zou, L. Wu, Q. Huang, D. Yang, M. Chen, M. Ban, C. Wu, T. Wu, S. Bai, T. Song, Q. Zhang and B. Sun, *ACS Appl. Mater. Interfaces*, 2018, **10**, 3784–3792.

151 C. Wang, A. S. R. Chesman and J. J. Jasieniak, *Chem. Commun.*, 2016, **53**, 232–235.

152 Y. Lou, Y. Niu, D. Yang, Q. Xu, Y. Hu, Y. Shen, J. Ming, J. Chen, L. Zhang and Y. Zhao, *Nano Res.*, 2018, **11**, 2715–2723.

153 B. Sun, O. Voznyy, H. Tan, P. Stadler, M. Liu, G. Walters, A. H. Proppe, M. Liu, J. Fan, T. Zhuang, J. Li, M. Wei, J. Xu, Y. Kim, S. Hoogland and E. H. Sargent, *Adv. Mater.*, 2017, **29**, 1700749.

154 M. Lu, J. Guo, P. Lu, L. Zhang, Y. Zhang, Q. Dai, Y. Hu, V. L. Colvin and W. W. Yu, *J. Phys. Chem. C*, 2019, **123**, 22787–22792.

155 B. A. Koscher, J. K. Swabeck, N. D. Bronstein and A. P. Alivisatos, *J. Am. Chem. Soc.*, 2017, **139**, 6566–6569.

156 C. Zheng, C. Bi, F. Huang, D. Binks and J. Tian, *ACS Appl. Mater. Interfaces*, 2019, **11**, 25410–25416.

157 C. B. Park, Y. S. Shin, Y. J. Yoon, H. Jang, J. G. Son, S. Kim, N. G. An, J. W. Kim, Y. C. Jun, G. H. Kim and J. Y. Kim, *J. Mater. Chem. C*, 2022, **10**, 2060–2066.

158 T. Cai, F. Li, Y. Jiang, X. Liu, X. Xia, X. Wang, J. Peng, L. Wang and W. A. Daoud, *Nanoscale*, 2019, **11**, 1319–1325.

159 X. Zheng, S. Yuan, J. Liu, J. Yin, F. Yuan, W. Shen, K. Yao, M. Wei, C. Zhou, K. Song, B. Zhang, Y. Lin, M. N. Hedhili, N. Wehbe, Y. Han, H. Sun, Z. Lu, T. D. Anthopoulos, O. F. Mohammed, E. H. Sargent, L. Liao and O. M. Bakr, *ACS Energy Lett.*, 2020, **5**, 793–798.

160 N. Yarita, T. Aharen, H. Tahara, M. Saruyama, T. Kawawaki, R. Sato, T. Teranishi and Y. Kanemitsu, *Phys. Rev. Mater.*, 2018, **2**, 116003.

161 S. Nakahara, H. Tahara, G. Yumoto, T. Kawawaki, M. Saruyama, R. Sato, T. Teranishi and Y. Kanemitsu, *J. Phys. Chem. C*, 2018, **122**, 22188–22193.

162 N. Yarita, H. Tahara, M. Saruyama, T. Kawawaki, R. Sato, T. Teranishi and Y. Kanemitsu, *J. Phys. Chem. Lett.*, 2017, **8**, 6041–6047.

163 X. Zhang, Z. Jin, J. Zhang, D. Bai, H. Bian, K. Wang, J. Sun, Q. Wang and S. F. Liu, *ACS Appl. Mater. Interfaces*, 2018, **10**, 7145–7154.

164 L. Ruan, W. Shen, A. Wang, Q. Zhou, H. Zhang and Z. Deng, *Nanoscale*, 2017, **9**, 7252–7259.

165 M. A. Uddin, J. K. Mobley, A. A. Masud, T. Liu, R. L. Calabro, D. Y. Kim, C. I. Richards and K. R. Graham, *J. Phys. Chem. C*, 2019, **123**, 18103–18112.

166 S. Park, H. Cho, W. Choi, H. Zou and D. Y. Jeon, *Nanoscale Adv.*, 2019, **1**, 2828–2834.

167 M. A. Uddin, J. D. Glover, S. M. Park, J. T. Pham and K. R. Graham, *Chem. Mater.*, 2020, **32**, 5217–5225.

168 A. Ghorai, S. Mahato, S. Singh, S. Bose, B. Roy, U. Jeong and S. K. Ray, *Angew. Chem.*, 2023, **135**, e202302852.

169 S. Baek, Y. Kim and S. W. Kim, *J. Ind. Eng. Chem.*, 2020, **83**, 279–284.

170 L. Ruan, W. Shen, A. Wang, A. Xiang and Z. Deng, *J. Phys. Chem. Lett.*, 2017, **8**, 3853–3860.

171 Z. Liu, Y. Bekenstein, X. Ye, S. C. Nguyen, J. Swabeck, D. Zhang, S. T. Lee, P. Yang, W. Ma and A. P. Alivisatos, *J. Am. Chem. Soc.*, 2017, **139**, 5309–5312.

172 X. Min, Q. Xie, Z. Wang, X. Wang and M. Chen, *Mater. Chem. Phys.*, 2022, **276**, 125404.

173 A. Wang, F. Muhammad, Y. Liu and Z. Deng, *Chem. Commun.*, 2021, **57**, 2677–2680.

174 X. Feng, J. Liu, X. Zhao, P. Xu and J. Liu, *J. Colloid Interface Sci.*, 2023, **629**, 63–72.

175 X. Feng, X. Zhao, J. Liu, P. Xu and J. Liu, *Adv. Mater. Interfaces*, 2022, **10**, 2201886.

176 D. Yang, X. Li, W. Zhou, S. Zhang, C. Meng, Y. Wu, Y. Wang and H. Zeng, *Adv. Mater.*, 2019, **31**, e1900767.

177 Y. Liu, Y. Zhu, J. Wang and P. Yang, *J. Phys. Chem. C*, 2023, **127**, 3123–3130.

178 F. Ye, H. Zhang, P. Wang, J. Cai, L. Wang, D. Liu and T. Wang, *Chem. Mater.*, 2020, **32**, 3211–3218.

179 H. Zhao, H. Chen, S. Bai, C. Kuang, X. Luo, P. Teng, C. Yin, P. Zeng, L. Hou, Y. Yang, L. Duan, F. Gao and M. Liu, *ACS Energy Lett.*, 2021, **6**, 2395–2403.

180 J. A. Pan, J. C. Ondry and D. V. Talapin, *Nano Lett.*, 2021, **21**, 7609–7616.

181 X. Kong, F. Xu, W. Wang, F. Juan, Y. Wu, X. Li, J. Li, X. Chen and B. Cao, *Appl. Phys. Lett.*, 2019, **115**, 153104.

182 F. Krieg, S. T. Ochsenbein, S. Yakunin, S. T. Brinck, P. Aellen, A. Suess, B. Clerc, D. Guggisberg, O. Nazarenko, Y. Shynkarenko, S. Kumar, C. J. Shih, I. Infante and M. V. Kovalenko, *ACS Energy Lett.*, 2018, **3**, 641–646.

183 Y. Zu, J. Xi, L. Li, J. Dai, S. Wang, F. Yun, B. Jiao, H. Dong, X. Hou and Z. Wu, *ACS Appl. Mater. Interfaces*, 2020, **12**, 2835–2841.

184 F. Krieg, P. C. Sercel, M. Burian, H. Andrusiv, M. I. Bodnarchuk, T. Stoferle, R. F. Mahrt, D. Naumenko, H. Amenitsch, G. Raino and M. V. Kovalenko, *ACS Cent. Sci.*, 2021, **7**, 135–144.

185 X. Mei, K. He, R. Zhuang, M. Yu, Y. Hua and X. Zhang, *Chem. Eng. J.*, 2023, **453**, 139909.

186 S. Wang, L. Du, Z. Jin, Y. Xin and H. Mattoussi, *J. Am. Chem. Soc.*, 2020, **142**, 12669–12680.

187 H. Jin, G. Y. Park, M. K. Kim, J. Cha, D. S. Ham and M. Kim, *Chem. Eng. J.*, 2023, **459**, 141531.

188 H. Kim, N. Hight-Huf, J. H. Kang, P. Bisnoff, S. Sundararajan, T. Thompson, M. Barnes, R. C. Hayward and T. Emrick, *Angew. Chem.*, 2020, **132**, 10894–10898.

189 S. H. Noh, W. Jeong, K. H. Lee, H. S. Yang, E. H. Suh, J. Jung, S. C. Park, D. Lee, I. H. Jung, Y. J. Jeong and J. Jang, *Adv. Funct. Mater.*, 2023, **33**, 2304004.

190 F. Krieg, Q. K. Ong, M. Burian, G. Raino, D. Naumenko, H. Amenitsch, A. Suess, M. J. Grotevent, F. Krumeich, M. I. Bodnarchuk, I. Shorubalko, F. Stellacci and M. V. Kovalenko, *J. Am. Chem. Soc.*, 2019, **141**, 19839–19849.

191 W. J. Mir, A. Alamoudi, J. Yin, K. E. Yorov, P. Maity, R. Naphade, B. Shao, J. Wang, M. N. Lintangpradipto, S. Nematulloev, A. H. Emwas, A. Genovese, O. F. Mohammed and O. M. Bakr, *J. Am. Chem. Soc.*, 2022, **144**, 13302–13310.

192 R. Grisorio, F. Fasulo, A. B. Munoz-Garcia, M. Pavone, D. Conelli, E. Fanizza, M. Striccoli, I. Allegretta, R. Terzano, N. Margiotta, P. Vivo and G. P. Suranna, *Nano Lett.*, 2022, **22**, 4437–4444.

193 Y. Hassan, J. H. Park, M. L. Crawford, A. Sadhanala, J. Lee, J. C. Sadighian, E. Mosconi, R. Shivanna, E. Radicchi, M. Jeong, C. Yang, H. Choi, S. H. Park, M. H. Song, F. De Angelis, C. Y. Wong, R. H. Friend, B. R. Lee and H. J. Snaith, *Nature*, 2021, **591**, 72–77.

194 B. Luo, S. B. Naghadeh, A. L. Allen, X. Li and J. Z. Zhang, *Adv. Funct. Mater.*, 2017, **27**, 1604018.

195 S. Wang, L. Zhou, F. Huang, Y. Xin, P. Jin, Q. Ma, Q. Pang, Y. Chen and J. Zhang, *J. Mater. Chem. C*, 2018, **6**, 10994–11001.

196 P. Bansal and P. Kar, *New J. Chem.*, 2019, **43**, 4599–4604.

197 J. Pan, Y. Shang, J. Yin, M. De Bastiani, W. Peng, I. Dursun, L. Sinatra, A. M. El-Zohry, M. N. Hedhili, A. H. Emwas, O. F. Mohammed, Z. Ning and O. M. Bakr, *J. Am. Chem. Soc.*, 2018, **140**, 562–565.

198 T. Chiba, Y. Hayashi, H. Ebe, K. Hoshi, J. Sato, S. Sato, Y. Pu, S. Ohisa and J. Kido, *Nat. Photonics*, 2018, **12**, 681–687.

199 J. Pan, L. Quan, Y. Zhao, W. Peng, B. Murali, S. P. Sarmah, M. Yuan, L. Sinatra, N. M. Alyami, J. Liu, E. Yassitepe, Z. Yang, O. Voznyy, R. Comin, M. N. Hedhili, O. F. Mohammed, Z. Lu, D. H. Kim, E. H. Sargent and O. M. Bakr, *Adv. Mater.*, 2016, **28**, 8718–8725.

200 F. Yang, H. Chen, R. Zhang, X. Liu, W. Zhang, J. Zhang, F. Gao and L. Wang, *Adv. Funct. Mater.*, 2020, **30**, 1908760.

201 Y. Wang, F. Yuan, Y. Dong, J. Li, A. Johnston, B. Chen, M. I. Saidaminov, C. Zhou, X. Zheng, Y. Hou, K. Bertens, H. Ebe, D. Ma, Z. Deng, S. Yuan, R. Chen, L. K. Sagar, J. Liu, J. Fan, P. Li, X. Li, Y. Gao, M. K. Fung, Z. Lu, O. M. Bakr, L. Liao and E. H. Sargent, *Angew. Chem., Int. Ed.*, 2021, **60**, 16164–16170.

202 C. C. Stoumpos and M. G. Kanatzidis, *Acc. Chem. Res.*, 2015, **48**, 2791–2802.

203 L. Meng, E. Yao, Z. Hong, H. Chen, P. Sun, Z. Yang, G. Li and Y. Yang, *Adv. Mater.*, 2017, **29**, 1603826.

204 A. Binek, F. C. Hanusch, P. Docampo and T. Bein, *J. Phys. Chem. Lett.*, 2015, **6**, 1249–1253.

205 N. Yantara, S. Bhaumik, F. Yan, D. Sabba, H. A. Dewi, N. Mathews, P. P. Boix, H. V. Demir and S. Mhaisalkar, *J. Phys. Chem. Lett.*, 2015, **6**, 4360–4364.

206 M. Yuan, L. Quan, R. Comin, G. Walters, R. Sabatini, O. Voznyy, S. Hoogland, Y. Zhao, E. M. Beauregard, P. Kanjanaboos, Z. Lu, D. H. Kim and E. H. Sargent, *Nat. Nanotechnol.*, 2016, **11**, 872–877.

207 S. Zhang, C. Yi, N. Wang, Y. Sun, W. Zou, Y. Wei, Y. Cao, Y. Miao, R. Li, Y. Yin, N. Zhao, J. Wang and W. Huang, *Adv. Mater.*, 2017, **29**, 1606600.

208 J. Si, Y. Liu, N. Wang, M. Xu, J. Li, H. He, J. Wang and Y. Jin, *Nano Res.*, 2017, **10**, 1329–1335.

209 L. Zhang, X. Yang, Q. Jiang, P. Wang, Z. Yin, X. Zhang, H. Tan, Y. Yang, M. Wei, B. R. Sutherland, E. H. Sargent and J. You, *Nat. Commun.*, 2017, **8**, 15640.

210 Z. Chu, Y. Zhao, F. Ma, C. Zhang, H. Deng, F. Gao, Q. Ye, J. Meng, Z. Yin, X. Zhang and J. You, *Nat. Commun.*, 2020, **11**, 4165.

211 L. Quan, M. Yuan, R. Comin, O. Voznyy, E. M. Beauregard, S. Hoogland, A. Buin, A. R. Kirmani, K. Zhao, A. Amassian, D. H. Kim and E. H. Sargent, *J. Am. Chem. Soc.*, 2016, **138**, 2649–2655.

212 R. Lindblad, N. K. Jena, B. Philippe, J. Oscarsson, D. Bi, A. Lindblad, S. Mandal, B. Pal, D. D. Sarma, O. Karis,

H. Siegbahn, E. M. J. Johansson, M. Odelius and H. Rensmo, *J. Phys. Chem. C*, 2015, **119**, 1818–1825.

213 H. Cho, S. H. Jeong, M. H. Park, Y. H. Kim, C. Wolf, C. L. Lee, J. H. Heo, A. Sadhanala, N. Myoung, S. Yoo, S. H. Im, R. H. Friend and T. W. Lee, *Science*, 2015, **350**, 1222–1225.

214 R. J. Stewart, C. Grieco, A. V. Larsen, G. S. Doucette and J. B. Asbury, *J. Phys. Chem. C*, 2016, **120**, 12392–12402.

215 D. T. Moore, H. Sai, K. W. Tan, D. M. Smilgies, W. Zhang, H. J. Snaith, U. Wiesner and L. A. Estroff, *J. Am. Chem. Soc.*, 2015, **137**, 2350–2358.

216 N. Ahn, D. Y. Son, I. H. Jang, S. M. Kang, M. Choi and N. G. Park, *J. Am. Chem. Soc.*, 2015, **137**, 8696–8699.

217 J. C. Hamill Jr., J. Schwartz and Y. L. Loo, *ACS Energy Lett.*, 2017, **3**, 92–97.

218 B. Li, D. Binks, G. Cao and J. Tian, *Small*, 2019, **15**, e1903613.

219 B. Jiao, X. Zhu, W. Wu, H. Dong, B. Xia, J. Xi, T. Lei, X. Hou and Z. Wu, *Nanoscale*, 2016, **8**, 11084–11090.

220 M. Xiao, F. Huang, W. Huang, Y. Dkhissi, Y. Zhu, J. Etheridge, A. Gray-Weale, U. Bach, Y. Cheng and L. Spiccia, *Angew. Chem., Int. Ed.*, 2014, **53**, 9898–9903.

221 J. C. Yu, D. W. Kim, D. B. Kim, E. D. Jung, K. S. Lee, S. Lee, D. D. Nuzzo, J. S. Kim and M. H. Song, *Nanoscale*, 2017, **9**, 2088–2094.

222 T. Bu, L. Wu, X. Liu, X. Yang, P. Zhou, X. Yu, T. Qin, J. Shi, S. Wang, S. Li, Z. Ku, Y. Peng, F. Huang, Q. Meng, Y. Cheng and J. Zhong, *Adv. Energy Mater.*, 2017, **7**, 1700576.

223 M. Yin, F. Xie, H. Chen, X. Yang, F. Ye, E. Bi, Y. Wu, M. Cai and L. Han, *J. Mater. Chem. A*, 2016, **4**, 8548–8553.

224 L. Xu, S. Che, J. Huang, D. Xie, Y. Yao, P. Wang, P. Lin, H. Piao, H. Hu, C. Cui, F. Wu, D. Yang and X. Yu, *Appl. Phys. Lett.*, 2019, **115**, 033101.

225 K. Bruening and C. J. Tassone, *J. Mater. Chem. A*, 2018, **6**, 18865–18870.

226 T. B. Song, Z. Yuan, F. Babbe, D. P. Nenon, E. Aydin, S. De Wolf and C. M. Sutter-Fella, *ACS Appl. Energy Mater.*, 2020, **3**, 2386–2393.

227 S. Pratap, F. Babbe, N. S. Barchi, Z. Yuan, T. Luong, Z. Haber, T. B. Song, J. L. Slack, C. V. Stan, N. Tamura, C. M. Sutter-Fella and P. Müller-Buschbaum, *Nat. Commun.*, 2021, **12**, 5624.

228 M. Tsige and G. S. Grest, *J. Phys.: Condens. Matter*, 2005, **17**, S4119–S4132.

229 M. P. Howard, W. F. Reinhart, T. Sanyal, M. S. Shell, A. Nikoubashman and A. Z. Panagiotopoulos, *J. Chem. Phys.*, 2018, **149**, 094901.

230 F. Haque, R. N. Bukke and M. Mativenga, *Materials*, 2021, **14**, 2573.

231 N. Rolston, K. A. Bush, A. D. Printz, A. Gold-Parker, Y. Ding, M. F. Toney, M. D. McGehee and R. H. Dauskardt, *Adv. Energy Mater.*, 2018, **8**, 1802139.

232 T. W. Jones, A. Osherov, M. Alsari, M. Sponseller, B. C. Duck, Y. K. Jung, C. Settens, F. Niroui, R. Brenes, C. V. Stan, Y. Li, M. Abdi-Jalebi, N. Tamura, J. E. Macdonald, M. Burghammer, R. H. Friend, V. Bulović, A. Walsh, G. J. Wilson, S. Lilliu and S. D. Stranks, *Energy Environ. Sci.*, 2019, **12**, 596–606.

233 S. Pratap, J. Schlipf, L. Bießmann and P. Müller-Buschbaum, *ACS Appl. Nano Mater.*, 2020, **3**, 11701–11708.

234 A. W. P. Sanches, M. A. T. da Silva, N. J. A. Cordeiro, A. Urbano and S. A. Lourenco, *Phys. Chem. Chem. Phys.*, 2019, **21**, 5253–5261.

235 S. Caicedo-Dávila, R. Gunder, J. A. Márquez, S. Levcenko, K. Schwarzburg, T. Unold and D. Abou-Ras, *J. Phys. Chem. C*, 2020, **124**, 19514–19521.

236 Y. Shao, Y. Yuan and J. Huang, *Nat. Energy*, 2016, **1**, 15001.

237 J. Liu, C. Gao, X. He, Q. Ye, L. Ouyang, D. Zhuang, C. Liao, J. Mei and W. Lau, *ACS Appl. Mater. Interfaces*, 2015, **7**, 24008–24015.

238 Y. Yu, Y. Tang, B. Wang, K. Zhang, J. Tang and Y. Li, *Laser Photonics Rev.*, 2022, **17**, 2200608.

239 L. Song, X. Guo, Y. Hu, Y. Lv, J. Lin, Z. Liu, Y. Fan and X. Liu, *J. Phys. Chem. Lett.*, 2017, **8**, 4148–4154.

240 J. Li, S. G. R. Bade, X. Shan and Z. Yu, *Adv. Mater.*, 2015, **27**, 5196–5202.

241 H. Lin, L. Zhu, H. Huang, C. J. Reckmeier, C. Liang, A. L. Rogach and W. C. H. Choy, *Nanoscale*, 2016, **8**, 19846–19852.

242 H. Huang, H. Lin, S. V. Kershaw, A. S. Susha, W. C. H. Choy and A. L. Rogach, *J. Phys. Chem. Lett.*, 2016, **7**, 4398–4404.

243 Z. Xiao, R. A. Kerner, L. Zhao, N. L. Tran, K. M. Lee, T. W. Koh, G. D. Scholes and B. P. Rand, *Nat. Photonics*, 2017, **11**, 108–115.

244 W. Ding, H. Liu, S. Zhang, D. Qiu, X. Li and S. Wang, *Adv. Funct. Mater.*, 2021, **32**, 2105164.

245 Z. Chu, Q. Ye, Y. Zhao, F. Ma, Z. Yin, X. Zhang and J. You, *Adv. Mater.*, 2021, **33**, e2007169.

246 M. G. La-Placa, G. Longo, A. Babaei, L. Martinez-Sarti, M. Sessolo and H. J. Bolink, *Chem. Commun.*, 2017, **53**, 8707–8710.

247 Z. Fang, W. Chen, Y. Shi, J. Zhao, S. Chu, J. Zhang and Z. Xiao, *Adv. Funct. Mater.*, 2020, **30**, 1909754.

248 T. Zhang, L. Xie, L. Chen, N. Guo, G. Li, Z. Tian, B. Mao and Y. Zhao, *Adv. Funct. Mater.*, 2017, **27**, 1603568.

249 Y. Ke, N. Wang, D. Kong, Y. Cao, Y. He, L. Zhu, Y. Wang, C. Xue, Q. Peng, F. Gao, W. Huang and J. Wang, *J. Phys. Chem. Lett.*, 2019, **10**, 380–385.

250 M. Abdi-Jalebi, Z. Andaji-Garmaroudi, S. Cacovich, C. Stavrakas, B. Philippe, J. M. Richter, M. Alsari, E. P. Booker, E. M. Hutter, A. J. Pearson, S. Lilliu, T. J. Savenije, H. Rensmo, G. Divitini, C. Ducati, R. H. Friend and S. D. Stranks, *Nature*, 2018, **555**, 497–501.

251 T. Wu, J. Li, Y. Zou, H. Xu, K. Wen, S. Wan, S. Bai, T. Song, J. A. McLeod, S. Duhm, F. Gao and B. Sun, *Angew. Chem., Int. Ed.*, 2020, **59**, 4099–4105.

252 L. Kong, X. Zhang, Y. Li, H. Wang, Y. Jiang, S. Wang, M. You, C. Zhang, T. Zhang, S. V. Kershaw, W. Zheng, Y. Yang, Q. Lin, M. Yuan, A. L. Rogach and X. Yang, *Nat. Commun.*, 2021, **12**, 1246.

253 Z. Wang, Z. Luo, C. Zhao, Q. Guo, Y. Wang, F. Wang, X. Bian, A. Alsaedi, T. Hayat and Z. Tan, *J. Phys. Chem. C*, 2017, **121**, 28132–28138.

254 E. Yoon, K. Y. Jang, J. Park and T. W. Lee, *Adv. Mater. Interfaces*, 2021, **8**, 2001712.

255 Z. Li, K. Cao, J. Li, X. Du, Y. Tang and B. Yu, *Org. Electron.*, 2020, **81**, 105675.

256 K. Wang, Y. Peng, J. Ge, S. Jiang, B. Zhu, J. Yao, Y. Yin, J. Yang, Q. Zhang and H. Yao, *ACS Photonics*, 2018, **6**, 667–676.

257 Y. Liu, T. Wu, Y. Liu, T. Song and B. Sun, *APL Mater.*, 2019, **7**, 021102.

258 H. Wang, H. Yuan, J. Yu, C. Zhang, K. Li, M. You, W. Li, J. Shao, J. Wei, X. Zhang, R. Chen, X. Yang and W. Zhao, *ACS Appl. Mater. Interfaces*, 2020, **12**, 53528–53536.

259 G. S. Kumar, B. Pradhan, T. Kamilya and S. Acharya, *Bull. Chem. Soc. Jpn.*, 2018, **91**, 1241–1248.

260 C. Kuang, Z. Hu, Z. Yuan, K. Wen, J. Qing, L. Kobera, S. Abbrent, J. Brus, C. Yin, H. Wang, W. Xu, J. Wang, S. Bai and F. Gao, *Joule*, 2021, **5**, 618–630.

261 S. Ahn, M. H. Park, S. H. Jeong, Y. H. Kim, J. Park, S. Kim, H. Kim, H. Cho, C. Wolf, M. Pei, H. Yang and T. W. Lee, *Adv. Funct. Mater.*, 2019, **29**, 1807535.

262 Q. Liu, S. Yuan, S. Sun, W. Luo, Y. Zhang, L. Liao and M. K. Fung, *J. Mater. Chem. C*, 2019, **7**, 4344–4349.

263 D. H. Kang, S. G. Kim, Y. C. Kim, I. T. Han, H. J. Jang, J. Y. Lee and N. G. Park, *ACS Energy Lett.*, 2020, **5**, 2191–2199.

264 Y. Shen, L. Cheng, Y. Li, W. Li, J. Chen, S. T. Lee and J. Tang, *Adv. Mater.*, 2019, **31**, e1901517.

265 R. Li, L. Cai, Y. Zou, H. Xu, Y. Tan, Y. Wang, J. Li, X. Wang, Y. Li, Y. Qin, D. Liang, T. Song and B. Sun, *ACS Appl. Mater. Interfaces*, 2020, **12**, 36681–36687.

266 X. Yang, X. Zhang, J. Deng, Z. Chu, Q. Jiang, J. Meng, P. Wang, L. Zhang, Z. Yin and J. You, *Nat. Commun.*, 2018, **9**, 570.

267 M. You, H. Wang, F. Cao, C. Zhang, T. Zhang, L. Kong, L. Wang, D. Zhao, J. Zhang and X. Yang, *ACS Appl. Mater. Interfaces*, 2020, **12**, 43018–43023.

268 L. Wang, L. Xiao, H. Gu and H. Sun, *Adv. Opt. Mater.*, 2019, **7**, 1801154.

269 S. Yu, J. Hu, H. Zhang, G. Zhao, B. Li, Y. Xia and Y. Chen, *ACS Photonics*, 2022, **9**, 1852–1874.

270 C. Zhang, B. Qiao, S. Zhao, Z. Xu, P. Wang, Y. Chen, F. Yin, G. Teyssedre, C. Laurent and X. Xu, *Org. Electron.*, 2016, **39**, 348–353.

271 J. Liu, X. Sheng, Y. Wu, D. Li, J. Bao, Y. Ji, Z. Lin, X. Xu, L. Yu, J. Xu and K. Chen, *Adv. Opt. Mater.*, 2018, **6**, 1700897.

272 X. Liu, D. Yu, C. Huo, X. Song, Y. Gao, S. Zhang and H. Zeng, *Adv. Opt. Mater.*, 2018, **6**, 1800206.

273 Z. Tan, J. Luo, L. Yang, X. Li, Z. Deng, L. Gao, H. Chen, J. Li, P. Du, G. Niu and J. Tang, *Adv. Opt. Mater.*, 2020, **8**, 1901094.

274 J. Zhang, H. Tsai, W. Nie and B. Hu, *Nano Energy*, 2021, **79**, 105413.

275 R. Chakraborty, G. Paul and A. J. Pal, *Phys. Rev. Appl.*, 2020, **14**, 024006.

276 J. Liu, Z. Lu, X. Zhang, Y. Zhang, H. Ma, Y. Ji, X. Xu, L. Yu, J. Xu and K. Chen, *Nanomaterials*, 2018, **8**, 974.

277 X. Xu, K. Xiao, G. Hou, Y. Zhang, T. Zhu, L. Xu, J. Xu and K. Chen, *Adv. Opt. Mater.*, 2021, **9**, 2100636.